

Nonlinear and Chaotic Front Dynamics in Semiconductor Superlattices

vorgelegt von
Diplom-Physiker
Andreas Amann
aus Rastatt

von der Fakultät II – Mathematik und Naturwissenschaften
der Technischen Universität Berlin
zur Erlangung des akademischen Grades

Doktor der Naturwissenschaften
– Dr. rer. nat. –

genehmigte Dissertation

Promotionsausschuss:

Vorsitzender: Prof. Dr. Erwin Sedlmayr
Berichter: Prof. Dr. Eckehard Schöll, PhD
Berichter: Prof. Dr. Harald Engel

Tag der wissenschaftlichen Aussprache: 11. Dezember 2003

Berlin 2004
D 83

Zusammenfassung

Die Ladungsträgerdynamik in Halbleiterübergittern wird theoretisch auf der Grundlage eines semiklassischen sequentiellen Tunnelmodells untersucht. Abhängig von den Modellparametern ergeben sich dabei laufende oder stationäre Anreicherungs- und Verarmungsfronten der Elektronen.

Besonders interessante Szenarien entstehen dadurch, dass verschiedenartige Fronten miteinander in Wechselwirkung treten und sich gegenseitig annihilieren können. Durch diesen Mechanismus wird es möglich, ein chaotisches raum-zeitliches Verhalten bei konstanter äußerer Spannung herbeizuführen. Das dabei auftretende Bifurkationsverhalten wird analysiert. Es stellt sich heraus, dass ein äquivalentes Szenario auch in einem System aus Tankbehältern auftritt, welche nach bestimmten Regeln befüllt und entleert werden. Solche hybriden Tanksysteme werden üblicherweise bei der Beschreibung von Lagerhaltungsproblemen in Fabriken eingesetzt. Ein Hauptschwerpunkt dieser Arbeit ist es, diese überraschende Verbindung zweier vollständig unterschiedlicher dynamischer Systeme zu begründen. Dazu wird zunächst das Verhalten einzelner Fronten studiert, insbesondere deren Erzeugung am Emitterkontakt, sowie die Frontgeschwindigkeiten in Abhängigkeit des durch das Bauteil fließenden Stromes. Anschließend wird das Zusammenspiel der Fronterzeugungs- und Vernichtungsprozesse anhand einfacher Regeln erklärt, welche durch weitere Spezialisierung auf das erwähnte Tankmodell führen. Im einfachsten Fall lässt sich das Tankmodell mittels einer eindimensionalen iterierten Abbildung analysieren, und es werden die sich daraus ergebenden analytischen Ergebnisse mit den Resultaten aus der numerischen Behandlung der vollen mikroskopischen Modellgleichungen verglichen.

Weiterhin wird das dynamische Verhalten des Übergitters bei nichtkonstanter äußerer Spannung, wie zum Beispiel während Schaltvorgängen, betrachtet. Hierbei ergibt sich, dass das Schaltverhalten in nichttriviale Weise von der Größe der Schaltspannung abhängt. In diesem Zusammenhang wird auch das Verhalten unter einer kombinierten Gleich- und Wechselspannung untersucht.

Durch eine Erweiterung der ursprünglichen Modellgleichungen um eine zusätzliche Dimension senkrecht zur Haupttransportrichtung des Stroms wird es ferner möglich, die Wechselwirkung lateraler und vertikaler Strukturen näher zu beleuchten.

Abstract

The charge dynamics in semiconductor superlattices is studied theoretically on the basis of a semiclassical sequential tunneling model. Depending on the model parameters, moving or stationary electron accumulation and depletion fronts are obtained.

Particularly interesting scenarios arise from the interaction between the fronts and from the possibility of mutual front annihilation. With this mechanism it is possible to induce chaotic spatio-temporal behavior at a fixed external voltage. By analyzing the relevant bifurcations it turns out that an equivalent scenario also occurs in a system of water tanks, which are filled and emptied following a given set of rules. This type of hybrid tank system is known to be useful for the description of stock-keeping problems in production systems. One main focus of this work is to substantiate this surprising connection between two completely different dynamical systems. For this purpose, we first study the dynamical behavior of single fronts, in particular their generation at the emitter contact, as well as the front velocities as a function of the overall current through the device. We then explain the interplay of front generation and annihilation processes on the basis of simple rules, which eventually lead to the tank model with further specialization. In the most simple case, the tank model may be analyzed by means of a one-dimensional iterated map, and we compare the analytical results with the numerical results from the full microscopic model equations.

Also the dynamical behavior of the superlattice under nonstationary external voltage conditions, such as during switching processes, is considered. It turns out that the switching scenarios depend in a nontrivial way on the switching voltage. In this context we also investigate the behavior at a combined ac and dc voltage.

By extending the original model equations with an additional dimension perpendicular to the main current, we explore the interaction between lateral and vertical structures.

Contents

1	Introduction	1
2	The Microscopic Model	5
2.1	Vertical Transport	5
2.1.1	Quantum Transport	5
2.1.2	Decoherence Theory	7
2.2	The Sequential Tunneling Model	9
2.2.1	The Well to Well Characteristic	10
2.2.2	Global Coupling	12
2.3	Boundary Currents	13
3	Front Dynamics in One Spatial Dimension	15
3.1	Dynamics of a Single Front	15
3.1.1	The Current Velocity Characteristic	18
3.1.2	Depletion Front with Positive Velocity	22
3.1.3	Stationary Accumulation Front	23
3.1.4	Accumulation Front with Positive Velocity	24
3.1.5	Accumulation Front with Negative Velocity	27
3.2	Multiple Fronts under Fixed External Voltage	28
3.3	Front Generation and Annihilation	30
3.3.1	Front Injection at the Emitter	30
3.3.2	Front Collisions	35
3.3.3	Front Annihilation at the Collector	36
4	Chaotic Front Dynamics	37
4.1	Bifurcation Scenarios of the Microscopic Model	37
4.1.1	The Case $\sigma = 0.5 (\Omega m)^{-1}$	37
4.1.2	Varying σ	41
4.1.3	Lyapunov Exponents	45
4.2	The Front model	47
4.2.1	Elimination of the current density	47
4.2.2	The rules for the front model	49
4.2.3	The case $n = 3$	52
4.2.4	Arbitrary n	55

5	The Tank Model	59
5.1	Deduction from the Front Model	59
5.1.1	The Case $p_l = 0$	59
5.1.2	The Case $p_l > 0$	61
5.2	Connection to Water Tanks	62
5.3	The Poincaré Map	63
5.4	Bifurcation Analysis for $n = 3$	66
5.4.1	Connection with the Flat-Topped map	67
5.4.2	The Tent-Map Case $\lambda = 1$	69
5.4.3	The Case $\lambda < 1$	72
5.4.4	Elementary Intervals	74
5.4.5	Period Doubling Cascade	75
5.4.6	Intermediate Intervals	76
5.4.7	Symbolic Dynamics	76
5.4.8	Chaoticity	77
5.5	Bifurcation Analysis for $n = 4$	78
6	Nonstationary External Voltage	81
6.1	Switching	82
6.1.1	Down Jumps	83
6.1.2	Up Jumps	86
6.2	Ramping	90
6.3	Sweeping	91
6.4	Impedance	92
7	Front Dynamics in Two Spatial Dimensions	97
7.1	Lateral Transport Theory	97
7.1.1	Dynamical Equations	97
7.1.2	The Generalized Einstein Relation	98
7.1.3	Solving Poisson's Equation	98
7.2	Stability of Inhomogeneous Lateral Patterns	100
8	Summary and Outlook	105
	Bibliography	109

List of Important Symbols

Symbol	Description
U_0 / U	external voltage / voltage at superlattice
m_B^* / m_W^*	effective electron mass in barrier / well
E_c^B / E_c^W	Γ point conduction band energy for barrier / well
$\Psi_{m\mathbf{k}}^\nu(z, \mathbf{r})$	Wannier wave function localized at well m with lateral wave vector \mathbf{k} and band index ν
b / w	barrier / well width
d / L	period / total length of superlattice
A	sample cross section
n_m	electron density in well m
N_D	two-dimensional doping density
F_m	electric field between well m and well $m + 1$
$j_{m \rightarrow m+1}$	current density from well m to well $m + 1$
N	number of wells in superlattice
σ	Ohmic boundary conductivity
j	global current density
$F^l(j) / F^h(j)$	low and high field branch of electron density vs. electric field characteristic
F_{\max}^l / F_{\min}^h	largest / smallest field on low / high field branch
j_{\max}^l / j_{\min}^h	largest / smallest current on low / high field branch
j_{\max}^s / j_{\min}^s	largest / smallest current for which stationary fronts occur
Q_a / Q_d	charge of a fully developed accumulation / depletion front
p_a / p_d	position of accumulation / depletion front within superlattice
a_i / d_i	position of the i th accumulation / depletion front
$v_a(j) / v_d(j)$	velocity of accumulation / depletion front
N_a / N_d	number of accumulation / depletion fronts
j_d	current density for which $v_a(j_d) = v_d(j_d)$
$j_{(N_a, N_d)} = j \left(\frac{N_a}{N_d} \right)$	current density for which $N_a v_a(j) = N_d v_d(j)$
(F_c, j_c)	intersection point of homogeneous current density characteristic with emitter current density characteristic
L_h	length of high field region in superlattice
r_c	ratio N_a/N_d for which $j(r_c) = j_c$

Contents

Symbol	Description
p_h / p_l	minimum length of high / low field domain at emitter, before new fronts can be injected
n	maximum number of fronts of one type ($n = \max [N_a^{\max}, N_d^{\max}]$)
x_i	length of the i th high field domain and filling height of tank $\#i$.
μ	draining rate for all tanks
λ	filling rate of tank connected to server
P^n / B^n	Poincaré map / Poincaré section of the n -tank model
M^{III}	matrix for reordering of tank positions after switching
\tilde{N}_d	number of nonempty tanks before the next switching of the server
t_{m+1}^- / t_{m+1}^+	time just before / after next switching
Δx_e	maximum amount of water lost by one tank before switching
z	p_h in units of L_h , ($z = p_h / L_h$)
$\hat{P}_z^n(x)$	P^n rescaled in units of L_h
I_z^P	flat segment of \hat{P}_z^n
$f_\lambda(x)$	flat topped map on unit interval with maximum at $\lambda = 1 - z/2$
f_1	tent map
$f_\lambda^{(k)}$	k th iterate of f_λ
I_λ^f	flat segment of f_λ
Q	string consisting of $k - 1$ letters of 0 or 1
$l = \%_0 Q$	Q is the binary representation of l
\tilde{Q}	bitwise inverse of Q
$p_l^{(k)} = p_Q^k$	fixed points of $f_1^{(k)}$ on branches with positive slope
$n_l^{(k)} = n_Q^k$	fixed points of $f_1^{(k)}$ on branches with negative slope
x_λ^i	trajectory of $x_0 = 1/2$ under f_λ
$k(\lambda)$	the shortest periodic orbits of f_λ has the period $k(\lambda)$
I_Q^k	$I_Q^k = [p_Q^k, n_Q^k]$
U_i / U_f	initial / final voltage
U_{step}	$U_{\text{step}} = U_f - U_i$
U_{crit}	tripole relocation triggered for $U_{\text{step}} > U_{\text{crit}}$
τ_r	ramping time
U_{disc}	discontinuity in current voltage characteristic
τ_d / τ_s	delay time / switching time
τ_{rel}	relocation time $\tau_{\text{rel}} = \tau_d + \tau_s$
$U_{\text{ac}} / U_{\text{dc}}$	ac / dc part of the external voltage
$j_{m \rightarrow m+1}^{\parallel} / \mathbf{j}_m^{\perp}$	transversal / lateral current density
D_0	effective diffusion coefficient

1 Introduction

Moving fronts are the source of complex self-organized patterns in a broad range of nonlinear systems. Starting from classical water waves, fronts appear in many different forms in physics, such as the phase transition fronts in crystal growth [1] or as interstellar conduction fronts [2] in astronomy. Prominent examples for front systems in chemical science are the famous Belousov–Zhabotinskii reaction [3, 4] or combustion waves [5]. Furthermore fronts are often a key element in the self-organization processes in biological systems, for example the excitation wave in cardiac tissue [6] or during morphogenesis [7]. It is therefore an important task of nonlinear science to identify the basic features which are responsible for the similarities and differences observed in a variety of front systems and to provide a unified theory of front dynamics, which may explain the observed patterns irrespective of the particular system at hand.

Since the 1960s many aspects of single isolated fronts have been studied in the physical and mathematical literature. Thus a detailed understanding of the generation, the shape, and the propagation of single fronts in an infinite medium was obtained in the context of simplified mathematical models in one or two dimensions [8, 9]. In particular the importance of the non-equilibrium aspects was realized, and important notions like the distinction between bistable, excitable and oscillatory media were introduced.

In real world systems, however, multiple fronts often coexist, and the interaction between fronts may lead to sophisticated self-organized patterns. To understand the relevant mechanisms, it would be desirable to again obtain a simple mathematical picture, which is capable of identifying the key elements that lead to a particular pattern, but so far no unifying theory exists. Considerable effort in this direction has been made concerning the problem of turbulence in fluid systems, which is often quoted to be the “last great unsolved problem of classical physics” [10]. In spite of major advances, a unified theory for turbulence is still not available and it is also not clear, how the results in this area could be carried over to more general front systems.

Semiconductor devices have a long tradition as practically relevant nonlinear model systems [11, 12, 13, 14, 15, 16, 17, 18]. Fueled by their enormous technological relevance and economic success, semiconductor materials have become one of the best studied objects in solid state physics. The manufacturing technology for building small well defined semiconductor structures of high purity has steadily improved during the last decades, and structures in the sub-micron range are commercially available today.

1 Introduction

In a semiclassical description, the dynamically relevant quantities in semiconductor devices are typically the densities of the free electrons or holes, the electric field or the local temperature. Often the microscopic charge transport equations in such devices are nonlinear [13, 18] and may give rise to a local region of Negative Differential Conductance (NDC) in the local current density vs electric field characteristic. For an S-shaped or Z-shaped local characteristic, the inhomogeneous charge distribution is typically characterized by current filaments. Examples are the *Heterostructure Hot Electron Device* (HHED) [19], thyristors [20] or the *Double Barrier Resonant Tunneling* (DBRT) diode [21]. An N-shaped current density vs electric field characteristic typically gives rise to charge accumulation and depletion fronts forming electric field domains in the direction parallel to the current (*vertical* fronts). Vertically moving charge fronts appear for instance in the Gunn diode [11].

In the following we will specifically consider semiconductor superlattices, which consist of alternating layers of two different semiconductor materials. Using sophisticated growth techniques, such as the metal organic chemical vapor deposition (MOCVD), it is possible to fabricate such alternating layers with a thickness of only a few atomic monolayers at any desired doping density. What makes this type of structure particularly interesting is the fact that they exhibit at the same time, lateral filamentary structures and electron accumulation and depletion fronts in the vertical direction. From the technological aspect, superlattices may serve as a source for Gigahertz oscillations [22, 23, 24]. Recently, the successful operation of a so called “quantum cascade laser” [25, 26], which is a specifically modified superlattice, has sparked further interest in this type of structures.

It is the purpose of the present work to gain a better understanding of interacting fronts, by using the semiconductor superlattice as a particularly simple, but nevertheless technologically relevant model system. It will be shown that in this case, a simple mathematical model can indeed satisfyingly predict the basic bifurcation scenarios. The methods which worked successfully in this case, could well be generalized to suit other systems as well.

This thesis is organized as follows: After this introduction we will explain in Chapter 2 the basic electron transport mechanisms leading to a sequential tunneling model [27] for superlattices, which is used as the basis for the subsequent numerical calculations. In the following Chapter 3 we study the generation and motion of single fronts. It turns out that two complementary types of vertical fronts, namely the electron accumulation front, and the electron depletion front exist. We examine the velocity of single fronts as a function of the applied external current, and study the motion of multiple fronts, which is governed by the global constraint of the externally applied voltage. Particular consideration is given to the influence of the contact boundaries on the generation and annihilation processes of new fronts.

In Chapter 4 we combine these results and derive a simplified front model, which reproduces the numerically observed scenarios leading to chaos under a fixed external voltage. Under the additional assumption that fronts do not traverse the whole sample, we finally obtain in Chapter 5 a tank model, which explains the basic bi-

furcations by a set of filling rules for a system of water tanks. In the most simple nontrivial case this system further reduces to a one dimensional map, which can be analyzed analytically.

In the subsequent Chapter 6 we study the front dynamics under non-stationary external voltage conditions, such as switching, ramping, or combined ac+dc voltage. Further interesting dynamical features occur if an additional lateral degree of freedom for charge transport is taken into account. Such an extension is introduced in Chapter 7, and the basic effects of interacting lateral and vertical fronts is examined. Finally in Chapter 8 we give a brief summary and an outlook for possible directions of future research.

1 Introduction

2 The Microscopic Model

Grown-ups like numbers,
which make it unnecessary to
grasp the essential!

(Le Petite Prince)

In this chapter we will discuss the microscopic theory of the electron transport in semiconductor superlattices. We will concentrate on the topics which are necessary to understand the sequential tunneling model, which is used in the subsequent chapters. For a broader coverage of the microscopic theory the reader is referred to the books by Bastard [28] and Schöll [29] as well as to the recent review articles by Bonilla [30] and Wacker [27].

2.1 Vertical Transport

We consider a semiconductor superlattice, which consists of alternating layers of two types of materials with different band gaps, such as AlAs and GaAs, or $\text{Al}_x\text{Ga}_{1-x}\text{As}$ and GaAs. We will only consider electron transport in n -doped samples. Then the material with the lower conduction band edge will act as a quantum well, while the other material represents a quantum barrier. The band structure for an AlAs/GaAs superlattice is depicted in Fig. 2.1. The external voltage drop U is applied in the z direction, i.e. perpendicularly to the quantum well layers, giving rise to a vertical electron current.

2.1.1 Quantum Transport

Let us first consider a single electron in an infinitely long superlattice without bias. The alternating layers of barrier and well material result in a z -dependence in the potential energy of the electrons given by the conduction band edge $E_c(z)$, and also in the effective isotropic electron mass $m^*(z)$.¹ The numerical values for the

¹For the effective mass in the well material, we use the effective mass at the conduction band edge m_c^W . Since the electron energies we are interested in, can be located in the band gap of the barrier material, it is not appropriate to use the effective mass m_c^B at its conduction band edge. Instead we use an energy dependent effective mass $m^B(E)$ in the barrier material as proposed in [31], which interpolates linearly between zero at the valence band edge, and m_c^B at the conduction band edge.

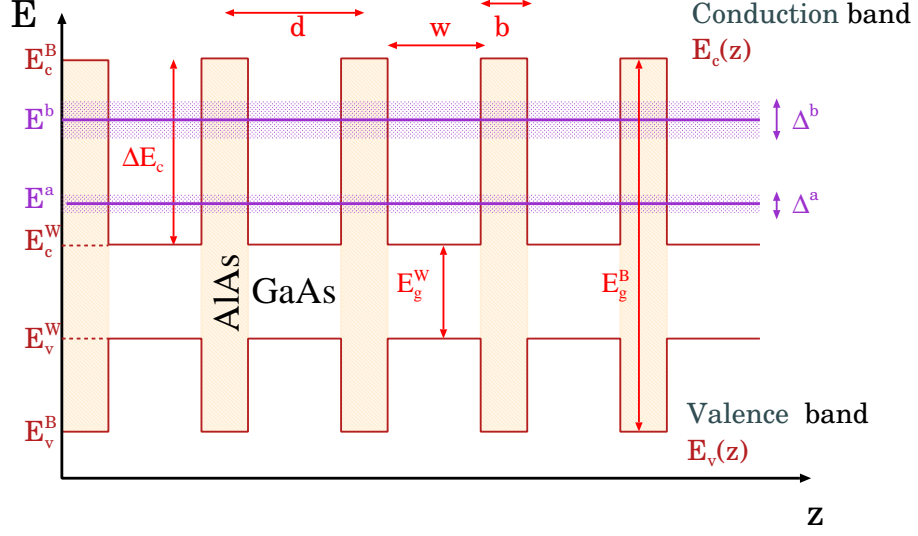


Figure 2.1: Schematic band structure of the conduction band $E_c(z)$ and the valence band $E_v(z)$ in an AlAs/GaAs superlattice with barrier width b , well width w and period $d = w + b$. $E_{c/v}^B$ and $E_{c/v}^W$ are the minimum energies of the conduction band (c) and valence band (v) for the barrier (B) and well (W) material, respectively; E_g^B and E_g^W are the respective energy gaps between valence and conduction band. $\Delta E_c = E_c^B - E_c^W$ is the difference in the conduction band energy of the well and the barrier material. Δ^a and Δ^b denote the widths of the first and the second minibands, which are located at the energies E^a and E^b , respectively.

effective masses and relevant energies in the case of GaAs and AlAs are given in Table 2.1.

Due to the periodicity of the structure, we have $E_c(z+d) = E_c(z)$ and $m^*(z+d) = m^*(z)$, and obtain a Kronig-Penney type Hamiltonian [33],

$$\mathcal{H} = -\nabla \frac{\hbar^2}{2m^*(z)} \nabla + E_c(z), \quad (2.1.1)$$

with eigenfunctions of the form

$$\varphi_{q,\mathbf{k}}^\nu(\mathbf{r}, z) = e^{i\mathbf{k}\cdot\mathbf{r}} \varphi_{q,\mathbf{k}}^\nu(z). \quad (2.1.2)$$

	GaAs	AlAs
m_c	$0.067 m_e$	$0.15 m_e$
E_g	1.52 eV	3.13 eV
E_c	0	1.05 eV

Table 2.1: Material parameters for GaAs and AlAs after [31, 32].

Here \mathbf{r} and \mathbf{k} are vectors in the two-dimensional (x, y) plane, ν is the miniband index and $q \in [-\pi/d, \pi/d]$ is the quasi wave vector in z -direction. The Bloch functions $\varphi_{q,\mathbf{k}}^\nu(z)$ are of the form

$$\varphi_{q,\mathbf{k}}^\nu(z) = e^{iqz} u_{q,\mathbf{k}}^\nu(z), \quad (2.1.3)$$

with real d periodic functions $u_{q,\mathbf{k}}^\nu(z)$, and fulfill the one-dimensional Schrödinger equation

$$\left[-\frac{\partial}{\partial z} \frac{\hbar^2}{2m^*(z)} \frac{\partial}{\partial z} + V_{\mathbf{k}}(z) \right] \varphi_{q,\mathbf{k}}^\nu(z) = E_{q,\mathbf{k}}^\nu \varphi_{q,\mathbf{k}}^\nu(z), \quad (2.1.4)$$

with

$$V_{\mathbf{k}} = E_c(z) + \frac{\hbar^2 \mathbf{k}^2}{2m^*(z)}. \quad (2.1.5)$$

Note that for all relevant energies $m^*(z^{GaAs}) < m^*(z^{AlAs})$. This leads to the somewhat paradoxical situation that for large lateral momentum \mathbf{k} , we obtain $V_{\mathbf{k}}(z^{GaAs}) > V_{\mathbf{k}}(z^{AlAs})$, i.e. GaAs would act as a barrier, and AlAs attains the role of the quantum well. This however is an artifact, which arises from the use of the effective mass approximation at energies, at which it is not supposed to be valid. In the following we will drop the \mathbf{k} dependence of the Bloch functions by setting $\varphi_q^\nu = \varphi_{q\mathbf{k}=0}^\nu$.

A standard textbook solution of the Kronig-Penney model [28] yields the dispersion relation of the form

$$E_{q,\mathbf{k}}^\nu = \frac{\hbar^2 \mathbf{k}^2}{2m^*(z)} + E_q^\nu, \quad (2.1.6)$$

where E_q^ν is given by the implicit equation

$$\cos(qd) = \cos(k_W w) \cosh(\kappa_B b) - \frac{1}{2} \left(\frac{m_B^* k_W}{m_W^* \kappa_B} - \frac{m_W^* \kappa_B}{m_B^* k_W} \right) \sin(k_W w) \sinh(\kappa_B b), \quad (2.1.7)$$

with $k_W = \sqrt{2m_W^* E_q^\nu} / \hbar$ and $\kappa_B = \sqrt{2m_B^* (\Delta E_c - E_q^\nu)} / \hbar$.

2.1.2 Decoherence Theory

The Bloch functions φ_q^ν diagonalize the Hamiltonian \mathcal{H} in (2.1.6) for a single electron exactly, and appear therefore to be the most suitable basis from the quantum mechanical point of view. However one apparent problem with the basis φ_q^ν is that they are completely delocalized. In practice however, the electrons appear to be localized on a length scale of a few nanometers, and are not expected to extend over the whole superlattice, which may be several hundreds of nanometers long. This localization effect is even stronger, when inhomogeneous charge distributions occur. Therefore we may ask, how the transition from the delocalized electron to a localized one can be explained in a quantum mechanically correct way.

This question is related to the more general question, why objects appear to be localized on a macroscopic scale, even if the quantum mechanical eigenstates are

2 The Microscopic Model

delocalized. This is answered conclusively by the so called *decoherence theory* which was introduced by Zeh [34] in an attempt to overcome the measuring problem in quantum mechanics. One of the basic observations in this theory is that due to the continuous quantum mechanical interaction between all macroscopic objects, a single object will not undergo the quantum mechanical transitions that would be possible if the object was isolated [35, 36]. Instead, the objects tends to prefer the basis, in which the interaction with the environment is diagonal. This so called *quantum Zeno effect* has been verified in optical experiments [37]. The preference of the position eigenstates, which results in the desired localization effect, is then simply a consequence of the fact that all interactions are local, i.e. diagonal in position space, but not in momentum space. This is in particular the case for the Coulomb and the gravitational interactions, which are the dominant interactions between macroscopic objects. These interactions therefore tend to produce many particle entangled states $|\Psi\rangle$ which are composed of components with approximate eigenstates of the position operator, i.e.

$$|\Psi\rangle = \sum_i c_i |1_i\rangle |2_i\rangle \cdots |n_i\rangle, \quad (2.1.8)$$

with $\hat{x}^n |n_i\rangle \approx x_i |n_i\rangle$, where $|n_i\rangle$ is a single particle state. If there are many objects present ($n \gg 1$), the phases between the individual components of the entangled state become quickly randomized ($\langle c_i c_j \rangle = 0$), which leads to decoherence, and makes transitions between different components effectively impossible. On a small scale with few particles however, the phases are not randomized, and quantum coherence can be maintained for a long time.

The advantage of this approach is that there is no need for a singular measurement process, which “collapses” the wave functions in the sense of the Copenhagen Interpretation of quantum mechanics. Instead, what is conceived as a measurement, is merely the practical separation of different components of an entangled state, and is completely explained within quantum mechanics. The question, whether an interpretation of quantum mechanics along these lines necessarily leads to a “many-worlds” interpretation [38] is still open to debate [35], and should not concern us here. We conclude however that the decoherence theory can in principle quantitatively predict how the interaction with the environment influences the decoherence length of the electrons. In particular, the intermediate case, where the electrons are neither fully localized, nor fully delocalized could be calculated in a natural way.

The practical method to employ the decoherence theory, is to start with the density matrix of the full state $\rho = |\Psi\rangle\langle\Psi|$ which evolves according to the von Neumann equation with the complete Hamiltonian. We may then concentrate on the evolution of the first particle $|1\rangle$ by tracing out the other particles as environment

$$\rho^1 = \text{tr}_{2,\dots,n}\rho. \quad (2.1.9)$$

The equation of motion for this subsystem can then be reduced to a Lindblad type

equation [39]

$$i\frac{\partial\rho^1}{\partial t} = [\mathcal{H}^1, \rho^1] - i\Lambda [\hat{x}^1, [\hat{x}^1, \rho^1]], \quad (2.1.10)$$

where \mathcal{H}^1 is the reduced Hamiltonian and Λ summarizes the interaction of the environment with the considered subsystem. Note that due to the non-unitary part in (2.1.10), the subsystem can evolve from a pure state to a seemingly mixed state, although the full density matrix ρ remains in a pure state. The net effect of this non-unitary part is that the non diagonal elements in the position basis of ρ are damped exponentially [35], i.e.

$$\rho(x, x', t) = \rho(x, x', 0) \exp(-\Lambda t(x - x')^2), \quad (2.1.11)$$

which leads to a spatial decoherence.

In this work we are dealing with weakly coupled superlattices, where we may assume that the spatial decoherence due to (2.1.11) is strong enough to localize the electrons within one quantum well. It may be worthwhile, however to test the implications of decoherence theory in the more critical case of strongly coupled superlattices, where nontrivial predictions can be expected. It might for instance be possible to strictly derive a continuum model of the type used in [40].

2.2 The Sequential Tunneling Model

For the sequential tunneling model we assume that the neighboring quantum wells in the superlattice are weakly coupled, and therefore the localization effect due to decoherence is large. It is then useful to work in a basis with localized wave functions instead of energy eigenstates. A perfectly localized (delta peak) state would require a superposition of all Bloch states in all minibands and is unphysical. But if we restrict ourselves to superpositions of Bloch states from only one miniband we are led to consider Wannier functions [41], defined by [42]

$$\Psi^\nu(z) = \sqrt{\frac{d}{2\pi}} \int_{-\pi/d}^{\pi/d} dq \varphi_q^\nu(z). \quad (2.2.1)$$

Here the phases of the different φ_q^ν have to be chosen in such a way that the best localization in well number 0 is achieved. A general Wannier function localized at well m and with lateral wave vector \mathbf{k} is then given by

$$\Psi_{m\mathbf{k}}^\nu(z, \mathbf{r}) = \Psi^\nu(z - md) e^{i\mathbf{k}\cdot\mathbf{r}}. \quad (2.2.2)$$

Taking into account an additional electric field F , the Hamiltonian (2.1.1) can be written in this new basis in a matrix of the form [27]

$$\mathcal{H}_{n\mathbf{k};m\mathbf{k}'}^{\nu\mu} = \left\{ E^\nu \delta_{nm} \delta_{\nu\mu} + \sum_{h=1}^{\infty} (T_h^\nu \delta_{\nu\mu} - eFR_h^{\nu\mu}) (\delta_{(n+h)m} + \delta_{(n-h)m}) \right\} \delta_{\mathbf{k}\mathbf{k}'}. \quad (2.2.3)$$

2 The Microscopic Model

Here the energy of the miniband E^ν , and the coupling to the h -nearest neighbor well T_h^ν is obtained from a Fourier expansion of the dispersion relation [42]

$$E_q^\nu = E^\nu + \sum_{h=1}^{\infty} 2T_h^\nu \cos(hdq). \quad (2.2.4)$$

In the following we will only take into account the coupling between neighboring wells ($h = 1$). The electric field F gives rise to an additional potential $V_F(z) = -eFz$ yielding the matrix elements $R_h^{\nu\mu} = \int dz \Psi^\nu(z - hd) \Psi^\mu(z)$.

If the decoherence time τ_ϕ is small compared to the tunneling time, i.e. $\Gamma = \hbar/\tau_\phi \gg T_1^\nu \sqrt{2}$, the phase information is lost between two tunneling events, and the electron tunnels incoherently. Under this condition a sequential tunneling approach is justified [43]. If furthermore the thermodynamical relaxation between the different energy levels of one quantum well is faster than the tunneling rate, we can assume that each well is in a quasi-equilibrium state, characterized by a quasi-electron temperature T . The effects due to electron heating and varying T were studied in [44, 45], here we assume that the electron temperature T coincides with the constant lattice temperature. If we furthermore assume that the lateral sample cross section A is so small that the electron concentration is homogeneous in (x, y) direction, then the electron configuration of the superlattice is completely determined by the electron densities n_m in each quantum well $m = 1 \dots N$, where N is the number of quantum wells. Here n_m is the number of electrons in well m per sample cross section A and is therefore a two-dimensional density. The electron concentration changes according to the continuity equation

$$e\dot{n}_m = j_{m-1 \rightarrow m} - j_{m \rightarrow m+1}, \quad (2.2.5)$$

where $e < 0$ is the charge of the electron and $j_{m \rightarrow m+1}$ is the current density from well m to well $m + 1$.

2.2.1 The Well to Well Characteristic

Physically, the current density $j_{m \rightarrow m+1}$ should not only depend on the electron densities n_m and n_{m+1} , but also on the electric field F_m between the two wells. The electric field causes a relative shift of the miniband levels by $E_m^\nu + eF_m d = E_{m+1}^\nu$. If the miniband levels in two neighboring wells are aligned, i.e. $E_m^\nu \approx E_{m+1}^\mu$, *resonant* tunneling without photon or phonon emission is possible. Since the scattering Γ^ν causes an energy broadening of the miniband states, a resonant current occurs even if the level alignment is not perfect, but in general the current will decrease rapidly with increasing level mismatch. We model this behavior by assuming that the current density between the levels ν and μ is proportional to a Lorentzian of width $(\Gamma^\nu + \Gamma^\mu)/2$. For $k_B T \ll E^b - E^a$ we may furthermore assume that the tunneling current is dominated by electrons originating from one of the lowest energy levels E_m^a or E_{m+1}^a , since at quasi-equilibrium this is the only significantly populated

energy level. For the usual case $F < 0$ (electrons moving from left to right), we have $E_m^\nu > E_{m+1}^\nu$, and the tunneling current from E_{m+1}^a to E_m^ν with $\nu > 1$ can be neglected. $j_{m \rightarrow m+1}$ is then calculated by a Fermi's Golden Rule like expression [42],

$$j_{m \rightarrow m+1} = \sum_{1\nu} \frac{e}{\hbar} |\mathcal{H}_{m,m+1}^{a,\nu}|^2 \int_{E^a}^{\infty} dE \rho_0 [n_F(E - E_m^F) - n_F(E - E_{m+1}^F + eFd)] \times \frac{\Gamma^1 + \Gamma^\nu}{(eFd + E^a - E^\nu)^2 + (\Gamma^1 + \Gamma^\nu)^2/4}, \quad (2.2.6)$$

where $n_F(x) = (1 + \exp(x/k_B T))^{-1}$ is the Fermi function, E_m^F is the Fermi energy in well m , $\rho_0 = m/\pi\hbar^2$ is the two dimensional density of state, and k_B is Boltzmann's constant. Using

$$n = \int_{E^a}^{\infty} dE \rho_0 n_F(E - E_m^F) = \rho_0 k_B T \ln \left(1 + \exp \frac{E_m^F}{k_B T} \right), \quad (2.2.7)$$

we may express the Fermi energy E_m^F is a function of the electron density n_m . Performing the integration in (2.2.6) and replacing E_m^F and E_{m+1}^F by n_m and n_{m+1} via (2.2.7), we finally find

$$j_{m \rightarrow m+1}(F_m, n_m, n_{m+1}) = \sum_{\nu} \frac{e}{\hbar} |\mathcal{H}_{m,m+1}^{1,\nu}|^2 \times \frac{\Gamma^1 + \Gamma^\nu}{(E^\nu - E^a - eF_m d)^2 + \left(\frac{\Gamma^a + \Gamma^\nu}{2}\right)^2} \times \left\{ n_m - \rho_0 k_B T \ln \left[\left(e^{\frac{n_{m+1}}{\rho_0 k_B T}} - 1 \right) e^{-\frac{eF_m d}{k_B T}} + 1 \right] \right\}. \quad (2.2.8)$$

In the following we will only take into account the two lowest minibands. The corresponding matrix elements can be obtained from (2.2.3) as $\mathcal{H}_{m,m+1}^{a,a} = T_1^1$ and $\mathcal{H}_{m,m+1}^{a,b} = -eFR_1^{a,b}$. Note that (2.2.8) is only valid for $F < 0$. For $F > 0$ we use the identity

$$j_{m \rightarrow m+1}(F_m, n_m, n_{m+1}) = -j_{m \rightarrow m+1}(-F_m, n_{m+1}, n_m). \quad (2.2.9)$$

For concreteness let us consider a superlattice of type A with the physical parameters given in Table 2.2. The well to well characteristic $j_{m \rightarrow m+1}(F_m, n_m, n_{m+1})$ for different values n_m is plotted in Fig. 2.2. The homogeneous characteristic $n_m = n_{m+1}$ (orange curve in Fig. 2.2) is point symmetric with respect to the origin as required by (2.2.9), and shows four pronounced extrema which we label by the letters A, B, C and D. The outer peaks A and D correspond to the resonant currents from E_m^a to E_{m+1}^b and E_{m+1}^a to E_m^b , respectively. On the other hand, the two inner peaks B and C are due to the tunneling current between E_{m+1}^a and E_m^a . If we now keep n_{m+1} fixed at the doping density N_D and vary n_m , we find that peak D is not affected at all, since the current from E_{m+1}^a to E_m^b only depends on n_{m+1} . On the other hand,

Parameter	Superlattice A	Superlattice B
barrier	AlAs	Al _{0.3} Ga _{0.7} As
well	GaAs	GaAs
b [nm]	4.0	5.0
w [nm]	9.0	8.0
d [nm]	13.0	13.0
E^a [meV]	47.1	41.5
E^b [meV]	176.5	160
Γ_a [meV]	4.0	4.0
Γ_b [meV]	4.0	4.0
T [K]	5	20
$R_1^{a,b}$ [mm]	0.268	12.7
N	40	100
N_D^{3D} [10^{15}cm^{-3}]	167	77
N_D [μm^{-2}]	2170	1000

Table 2.2: Superlattice parameters. Superlattices A corresponds to the experimental sample used in [46, 47]. Superlattice B is similar to the experimental lattice in [48], but with a different doping density.

we find that the current density at peak A is proportional to n_m and in particular vanishes for $n_m = 0$. The position of the peaks A and D does not change. This is in contrast to peak C, which moves from $F_m = 0$ at $n_m = 0$ to higher values of $|F_m|$ with increasing n_m . At the same time the height of the peak decreases, until it is hardly visible at $n_m = 5N_D$ (Fig. 2.2). On the other hand peak B gets more pronounced and moves towards $F_m = 0$ with increasing n_m . We note that for $n_m \neq n_{m+1}$ the current density does not vanish at $F_m = 0$, since the Fermi energies are different in both wells.

2.2.2 Global Coupling

The electron densities and the electric fields are coupled by the following discrete version of Gauss's law,

$$\epsilon_r \epsilon_0 (F_m - F_{m-1}) = e(n_m - N_D) \quad \text{for } m = 1, \dots, N, \quad (2.2.10)$$

where N_D is the two-dimensional doping concentration, N is the number of wells in the superlattice, F_0 and F_N are the fields at the emitter and collector barrier and ϵ_r and ϵ_0 are the relative and absolute permittivities. Eq. (2.2.10) can be derived from Gauss's Law in the integral formulation, with the integration volume being one well with finite width w . Then Eq. (2.2.10) follows under the conditions that the charge is localized within the wells, and that the charge distribution does not depend on the lateral coordinates. This is the case since the electron wave

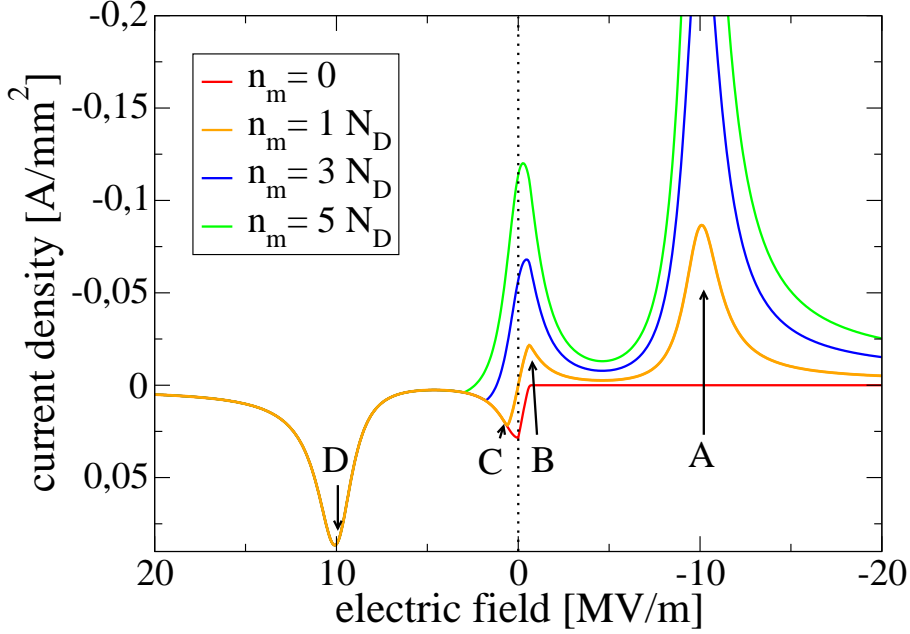


Figure 2.2: Well to well characteristic $j_{m \rightarrow m+1}(F, n_m, n_{m+1})$ (eq. (2.2.8)) of superlattice A (Table 2.2), for $n_{m+1} = N_D$ and various values of n_m .

functions are assumed to be Wannier functions in the vertical direction and plane waves in lateral direction, and the background charge due to doping is assumed to be confined to the center of the well.

The sum of the electric fields is then related to the total voltage drop U between emitter and collector by

$$U = - \sum_{m=0}^N F_m d. \quad (2.2.11)$$

Here we choose a sign convention for the voltage, which makes U positive, but the electric fields and current densities are negative. The global coupling by the external voltage U , will prove to decisively influence the dynamics of the superlattice. In particular, U may also depend on time as we will discuss in more detail in Chapter 6 (see also [49, 50]).

2.3 Boundary Currents

As will be discussed in Chapter 3, the proper choice of the boundary current $j_{0 \rightarrow 1}$ from the emitter to the first well decisively influences the dynamical front properties of the superlattice.

For the following numerical calculations, we use the following simple Ohmic

2 The Microscopic Model

boundary current densities [44]:

$$j_{0 \rightarrow 1} = \sigma F_0, \quad (2.3.1)$$

$$j_{N \rightarrow N+1} = \sigma F_N \frac{n_N}{N_D}. \quad (2.3.2)$$

where σ is the Ohmic conductivity, and the factor n_N/N_D is introduced in order to avoid negative electron densities at the collector. In Sec. 3.3.1 we will see that σ governs the injection of electron accumulation and depletion fronts at the emitter.

In [51] a more microscopic method for calculating the current from a highly doped emitter contact into the superlattice was proposed. A numerical implementation [52] shows that such a scheme also generates electron accumulation and depletion fronts at the emitter, which are equivalent to the fronts generated by the more simple Ohmic boundary currents.

In [53] an exponential boundary current density of the form

$$j_{0 \rightarrow 1} = a \exp(bF_0), \quad (2.3.3)$$

was considered. Here a and b are suitable parameters. Again it was found that the dynamical behavior of the superlattice is equivalent to the dynamics under Ohmic boundary currents.

From the experimental point of view, it is desirable to choose a specific dynamic scenario by tuning the contact conductivity σ . Recent experimental studies show that deep donors in the contact layers have a dramatic effect on the contact conductivity and a large increase of the contact resistance can be realized by decreasing the temperature below 200 K [54]. Since this effect is sensitive to illumination, it should be possible to adjust σ optically. Alternatively, the temperature dependence of the emitter current may also be exploited.

Other boundary conditions (Dirichlet and Neumann) have been used in earlier work [55, 56, 57, 58, 59, 60, 61].

3 Front Dynamics in One Spatial Dimension

It is not necessary to understand things in order to argue about them.

(Pierre Augustin Caron de Beaumarchais)

In a superlattice with a large number of quantum wells, charge accumulation and depletion fronts typically occur, and play a major role in the dynamical behavior of the system. Such fronts are either stationary or move with positive or negative velocities. Two typical examples of front dynamics are shown in Fig. 3.1. We see that particularly interesting scenarios may arise if fronts of opposite polarity collide and annihilate (see Fig. 3.1(a)). In this chapter we will discuss the basic dynamics of fronts in detail. The results of this chapter are the requisites for the *front* model which will be introduced in Chapter 4.

Our analysis starts from the microscopic sequential tunneling model which was explained in detail in Chapter 2. The model equations consist of the continuity equation (2.2.5), the discrete version of Gauss's law (2.2.10) and the global coupling by the external voltage (2.2.11), which we compile here once more for convenience:

$$e\dot{n}_m = j_{m-1 \rightarrow m} - j_{m \rightarrow m+1} \quad \text{for } m = 1, \dots, N, \quad (3.0.1)$$

$$\epsilon_r \epsilon_0 (F_m - F_{m-1}) = e(n_m - N_D) \quad \text{for } m = 1, \dots, N, \quad (3.0.2)$$

$$U = - \sum_{m=0}^N F_m d. \quad (3.0.3)$$

3.1 Dynamics of a Single Front

The dynamics of single fronts in discrete systems have been extensively studied in various contexts [62, 63, 64, 65], including the specific case of semiconductor superlattices [66, 67, 68, 69, 27]. Although the general theory of front propagation in discrete systems tends to become rather complicated [65], we will show that the basic properties of fronts in semiconductor superlattices can be understood easily by considering the “operating points” on the current density vs electric field characteristic across each barrier.

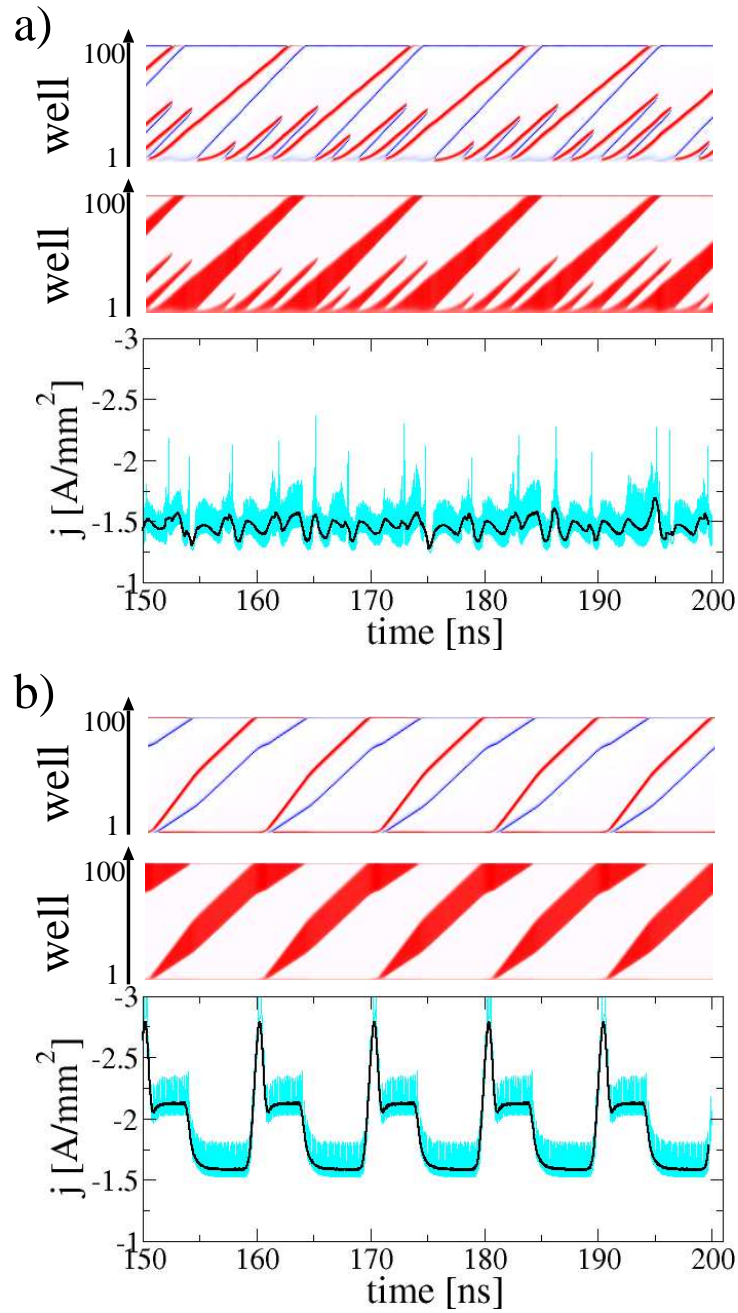


Figure 3.1: Examples for the evolutions of the electron densities (top panels), electric fields (middle panels) and current densities (bottom panels) of superlattice B for an external voltage $U = 2$ V and contact conductivity $\sigma = 0.5 \Omega^{-1}\text{m}^{-1}$ (a) and $\sigma = 1.3 \Omega^{-1}\text{m}^{-1}$ (b). In the top panels the electron accumulation and depletion layers are shaded in blue and red, respectively. The red areas in the middle panels show the high field domains. The raw current density data in the lower panels are plotted in cyan, while the black lines show a running average of the current over an interval of 0.5 ns.

Let us first consider the case of a single charge accumulation front, which is located far away from the contacts. This front is characterized by a number of consecutive quantum wells with indices m_l, \dots, m_r , where the electron densities are noticeably larger than the doping density N_D , whereas outside of the front the electron densities are approximately equal to N_D , i.e.

$$n_m > N_D + 5\% \quad \text{for } m \in [m_l, m_r], \quad (3.1.1)$$

$$n_m = N_D \pm 5\% \quad \text{else.} \quad (3.1.2)$$

Here a heuristic 5% accuracy cutoff is introduced since even far away from the front the electron density is never *exactly* equal to the doping density. An analogous definition for m_l and m_r applies in the case of a charge depletion front.

Instead of fixing the voltage drop U at the device by (3.0.3), it turns out to be advantageous to study the front motion at a fixed current density

$$j = \frac{1}{N+1} \sum_{m=0}^N j_{m \rightarrow m+1} \quad (3.1.3)$$

instead (here we neglected any contributions from the internal capacitance, since we are interested in the current inside the sample). Practically this is achieved by introducing a large external resistor R , and set

$$-U = -U_0 - RAj, \quad (3.1.4)$$

where A is the sample cross section, and U_0 is the fixed overall voltage. For a sufficiently large R we have $|U| \ll |RAj|$. The current density is then approximately fixed by

$$-j = \frac{U_0}{RA} - \frac{U}{RA} \approx \frac{U_0}{RA}. \quad (3.1.5)$$

Note that U itself is not assumed to be fixed. However, a change in U due to the internal degrees of freedom of the superlattice will only have a tiny effect on j , according to (3.1.5).

A typical profile for the electron density and the electric field of an electron accumulation front under fixed current density conditions is shown in Fig. 3.2. In this case the front width is about 6 wells.

Far away from the front, the well-to-well current densities obey the homogeneous current density vs field characteristic as in Fig. 3.3. Furthermore the electric field must be located on one of the branches with positive differential conductivity, since otherwise the configuration would not be stable against small charge fluctuations. For a fixed current density, this determines the low and high fields $F^l(j)$ and $F^h(j)$, respectively (see Fig 3.3). The field obeys Gauss's law (3.0.2) and therefore increases¹ from $F^l \approx 0$ to a large negative value F^h with increasing well number m .

¹Due to the negative sign of the electron, the electric fields and current densities are negative for our choice of the coordinate system. It is nevertheless customary to call F^h the *high* field and F^l the *low* field, although formally $0 > F^l > F^h$. Consequently, terms like *increasing* and *decreasing* are used in reversed logic in connection with fields and current densities.

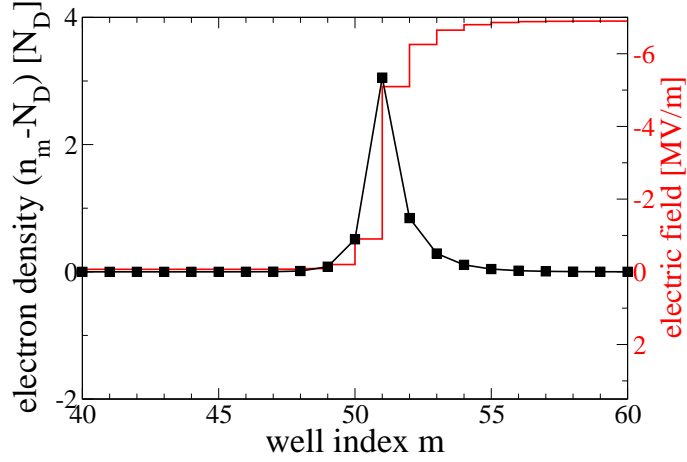


Figure 3.2: Electron density (black) and electric field (red) profile for a stationary charge accumulation front at constant current density. $j = -6.0 \text{ A/mm}^2$

The total charge $Q_a < 0$ per unit area in the accumulation front is then simply given by

$$Q_a(j) = \sum_{m=m_l}^{m_r} e(n_m - N_D) = \epsilon_r \epsilon_0 (F^h(j) - F^l(j)). \quad (3.1.6)$$

Here we assume that the current is fixed to the same value at both sides of the front, which is only possible if the current density is chosen in the interval where the multistability in the field occurs (cf. Fig. 3.3). Otherwise Q_a would be time-dependent, and the front would be unstable.

In the case of an electron depletion front, the electron density and field profiles are shown in Fig. 3.4. The electric field shows a drop from $F^h(j)$ to $F^l(j)$ with increasing well index m . By comparing with (3.1.6) it is obvious that the total charge of the depletion front is $Q_d = -Q_a$. We furthermore note that the charge profile of the depletion front is flatter and broader than for the accumulation front. The reason for this difference is that the electron density n_m is required to be positive. Therefore the contribution of one well to the total charge Q_d can not exceed $-eN_D$. Such a restriction does not apply for charge accumulation fronts, since there is no upper limit on n_m . In fact we see from Fig. 3.2 that for this choice of parameters, the majority of the charge in an accumulation front is located within one single well.

3.1.1 The Current Velocity Characteristic

In order to study the motion of charge fronts it is useful to define the position $p_{a/d}$ of the electron accumulation or depletion front by its center of charge,

$$p_{a/d} = \sum_{m=m_l}^{m_r} m d \frac{e(n_m - N_D)}{Q_{a/d}}. \quad (3.1.7)$$

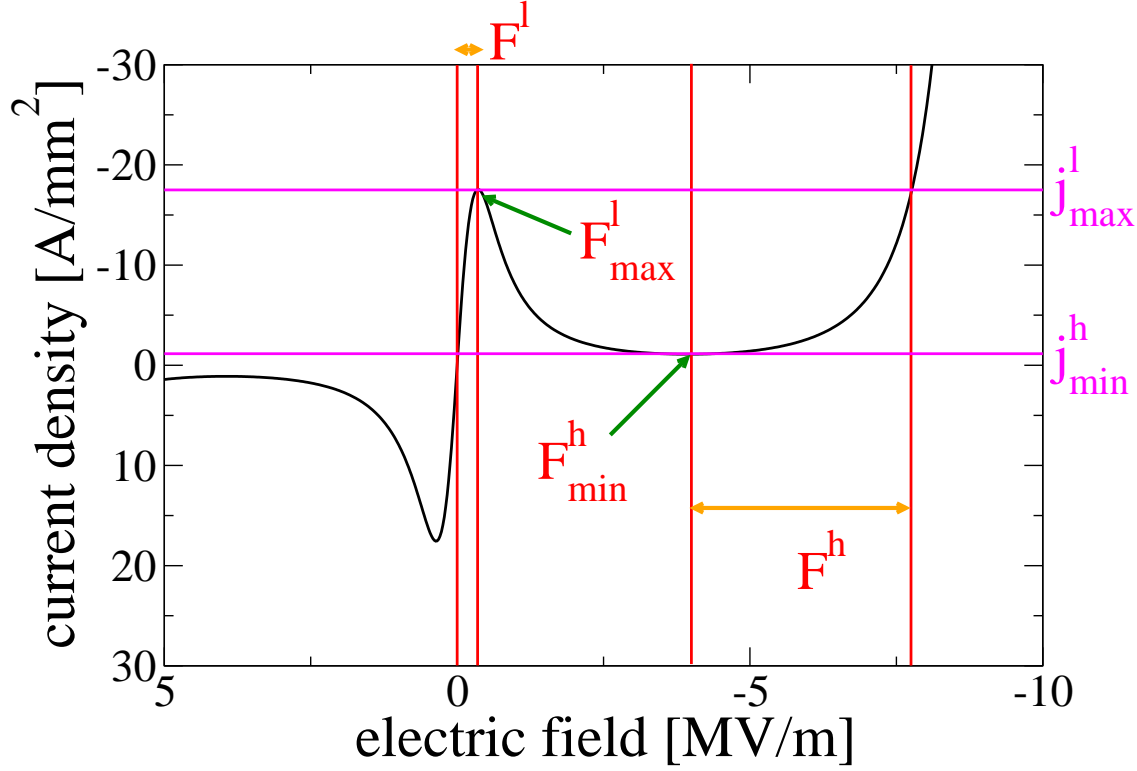


Figure 3.3: Homogeneous well-to-well current density vs field characteristic for a superlattice of type B. F^l and F^h denote the low and high field region on the first and third branch of the characteristic, respectively. The transition from the first branch to the second branch occurs at $(F_{\max}^l, j_{\max}^l) = (-0.36 \text{ MV/m}, -17.6 \text{ A/mm}^2)$ and the transition from the second to the third branch at $(F_{\min}^h, j_{\min}^h) = (-3.95 \text{ MV/m}, -1.10 \text{ A/mm}^2)$. Only the second branch exhibits negative differential conductivity. The orange double headed arrows indicate the possible ranges for F^l and F^h .

Note that $p_{a/d}$ is a real number, although the underlying superlattice is discrete. The velocity $v_{a/d}$ of an accumulation or depletion front can then be obtained by differentiating (3.1.7) with respect to time and using the continuity equation (3.0.1)

$$v_{a/d} = \dot{p}_{a/d} = \sum_{m=m_l}^{m_r} m d \frac{j_{m-1 \rightarrow m} - j_{m \rightarrow m+1}}{Q_{a/d}} \quad (3.1.8)$$

$$= \frac{d}{Q_{a/d}} \left(m_l j_{m_l-1 \rightarrow m_l} + \sum_{m=m_l}^{m_r-1} j_{m \rightarrow m+1} - m_r j_{m_r \rightarrow m_r+1} \right) \quad (3.1.9)$$

$$\approx \frac{d}{Q_{a/d}} \sum_{m=m_l}^{m_r-1} (j_{m \rightarrow m+1} - j), \quad (3.1.10)$$

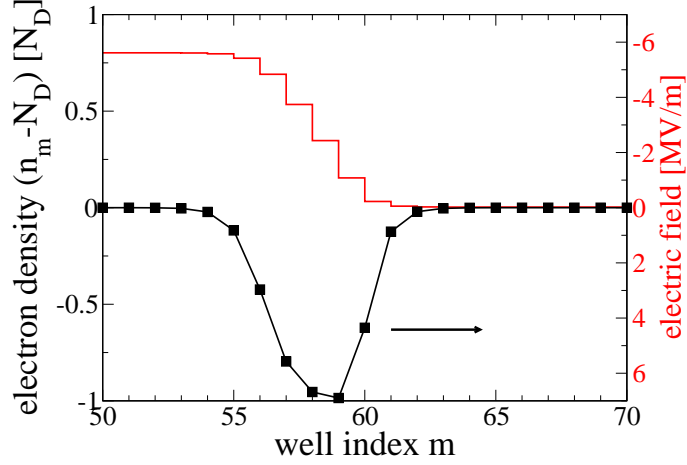


Figure 3.4: Electron density (black) and electric field (red) profile for a charge depletion front moving with positive velocity at a constant current density $j = -2.0 \text{ A/mm}^2$.

where in the last step we have used that $j_{m_l-1 \rightarrow m_l} \approx j_{m_r \rightarrow m_r+1} \approx j$, which is fulfilled to a high degree of accuracy for all current densities outside the front as defined by (3.1.1).

Further insight into the term $j_{m \rightarrow m+1} - j$ appearing in (3.1.10) can be gained by differentiating Gauss's law (3.0.2) with respect to t and using the continuity equation (3.0.1) to arrive at

$$\epsilon_r \epsilon_0 \frac{dF_m}{dt} = j - j_{m \rightarrow m+1} \quad \text{for } m = 0 \dots N. \quad (3.1.11)$$

Using (3.1.11) together with (3.0.2) and (3.0.3) leads to an alternative set of dynamical model equations in terms of electric fields, instead of electron densities, which is well studied in the literature [70, 71].

Substituting (3.1.11) into (3.1.10) and using the fact that $\dot{F}_m = 0$ for $m \notin [m_l, m_r]$ we obtain

$$v_{a/d} = -\frac{d}{Q_{a/d}} \sum_{m=0}^N \epsilon_r \epsilon_0 \frac{dF_m}{dt}. \quad (3.1.12)$$

Using (3.0.3) and (3.1.6) finally yields the simple relation

$$v_{a/d} = \pm \frac{1}{F^h(j) - F^l(j)} \frac{dU}{dt}. \quad (3.1.13)$$

We may use (3.1.13) to obtain the front velocities as a function of j numerically. For this purpose, we approximately fix the current density j using a large load resistor ($RA = 10^9 \Omega m^2$) according to (3.1.5). We then calculate the slope of the sample voltage $U(t)$ by numerical regression. The corresponding results are shown in Fig. 3.5. For the depletion front (red line in Fig. 3.5) we obtain an always

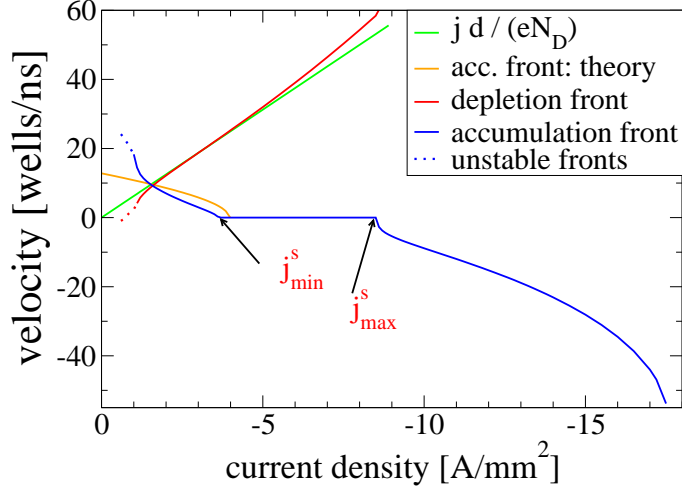


Figure 3.5: Front velocity vs current density for electron accumulation (blue) and depletion (red) fronts of superlattice B. The broken lines denote unstable fronts. j_{\min}^s and j_{\max}^s denote the minimum and maximum current for the stationary accumulation front. The orange and green lines are analytical predictions of the accumulation and depletion front velocities according to (3.1.25) and (3.1.14), respectively.

positive velocity which is approximately proportional to the current density. For small current densities however the depletion front becomes unstable (broken line) which is due to the fact that the high field branch $F^h(j)$ of the homogeneous current density characteristic can not support arbitrarily small currents, but has a minimum at $j_{\min}^h \approx -1.15 \text{ A/mm}^2$ (see Fig. 3.3). If we try to impose an external current density below j_{\min}^h , this will only affect the low field region, which is at the right of the front. Consequently more electrons are entering the front from the left than are leaving at the right border, until the depletion front has vanished.

For the electron accumulation front (blue line in Fig. 3.5) the velocity vs current density characteristic is more complicated. For small currents the front is unstable for the same reasons as the depletion front above. With increasing current the velocity drops from positive values to zero, which means that the front becomes stationary. The fact that the front can be *pinned* for a finite range of j is due to the discreteness of our system, and would disappear in the continuous limit $N \rightarrow \infty$, $d \rightarrow 0$. With further increase of the current, the front is unpinned and starts to move with negative velocity, i.e upstream towards the emitter [67]. Since currents larger than $j_{\max}^l \approx -17.5 \text{ A/mm}^2$ are not supported by the low field branch of the homogeneous characteristic (Fig. 3.3) the accumulation fronts become unstable beyond j_{\max}^l .

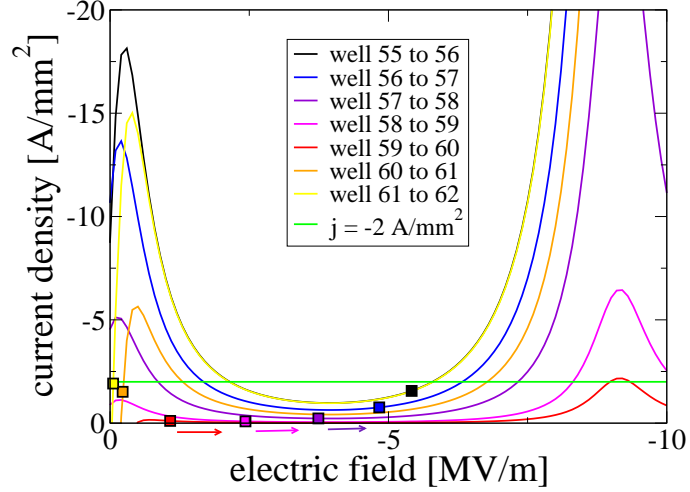


Figure 3.6: Various well-to-well characteristics $j_{m \rightarrow m+1}(F, n_m, n_{m+1})$ for the charge depletion front of Fig. 3.4 at $j = -2 \text{ A/mm}^2$. The framed squares denote the actual operating points $(F_m, j_{m \rightarrow m+1}(F_m, n_m, n_{m+1}))$ if the field profile of Fig. 3.4 is taken into account.

3.1.2 Depletion Front with Positive Velocity

The simplest case of front propagation is that of a depletion front (Fig. 3.4). For $m \in [m_l, m_r]$ the current density vs electric field characteristic $j_{m \rightarrow m+1}(F, n_m, n_{m+1})$ will not simply obey the homogeneous characteristic of Fig. 3.3, since n_m and n_{m+1} are different from N_D . But if the electron density profile n_m is known for one particular front, we can calculate the inhomogeneous characteristic $j_{m \rightarrow m+1}(F, n_m, n_{m+1})$ as a function of F at each m separately.

The resulting current density characteristics are shown in Fig. 3.6. We see that at the left and right borders of the front we obtain an almost homogeneous characteristic (black and yellow line in Fig. 3.6), since there the electron densities are not too different from the doping density. Inside the front the electron concentration is depleted and almost vanishes at the center of the front (see well 58 and 59 in Fig. 3.4). Following the discussion in Section 2.2.1, this results in severely suppressed current density characteristics (red and magenta lines in Fig. 3.6), which are in particular below the external current j (green line) for any field between F^l and F^h .

Let us now consider the operating points $(F_m, j_{m \rightarrow m+1})$. At the left boundary of the front the operating point is close to $(F^h(j), j)$ (black square in Fig. 3.6). With increasing well index m the field F_m decreases towards F^l and the current $j_{m \rightarrow m+1}$ drops to almost zero and rises again to j . We therefore note that all contributions to the velocity in (3.1.10) are positive, and we conclude $v_d > 0$.

A useful approximation for the velocity v_d can be obtained by considering (3.1.11) at the center of the front, where we can approximate $n_m \approx 0$. Then we have $j_{m \rightarrow m+1} = 0$, and $\dot{F}_m = j/(\epsilon_r \epsilon_0)$. From Gauss's law (3.0.2) we know on the other

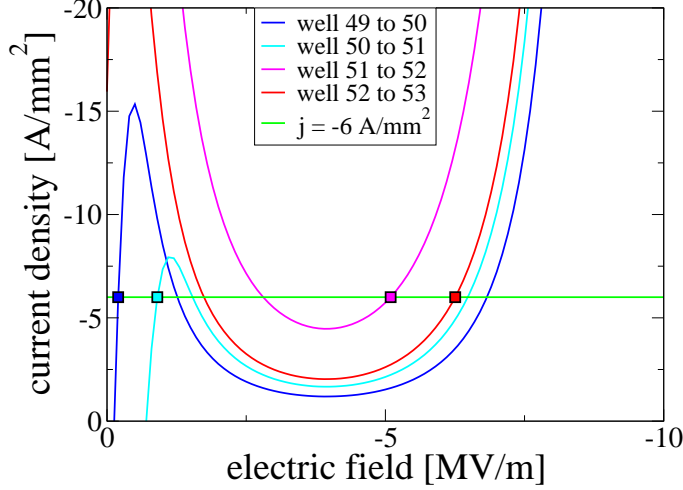


Figure 3.7: Well-to-well characteristics as in Fig. 3.6, but for a stationary charge accumulation front at $j = -6.0 \text{ A/mm}^2$. For the electric field and electron density profile of this front see Fig. 3.2.

hand that $F_{m-1} = F_m + eN_D/(\epsilon_r\epsilon_0)$. The time Δt at which $F_m(t + \Delta t) = F_{m-1}(t)$ is then given by $\Delta t = eN_D/j$. But Δt is also the time needed for the front to travel by one well period d . Thus the velocity of the depletion front is positive and can be approximated by [68, 66]

$$v_d \approx \frac{jd}{eN_D}. \quad (3.1.14)$$

From Fig. 3.5 we see that this approximation is in very good agreement with the numerical calculations, except for current densities close to the front instability. However, we stress that (3.1.14) is only valid for rather low doping density, i.e. $-eN_D < Q_d$ since the derivation depends on the presence of at least one completely depleted well with $n_m \approx 0$. It was in fact shown by Wacker [27] that for high doping values even negative velocities for v_d are possible.

3.1.3 Stationary Accumulation Front

Let us now consider a stationary accumulation front, i.e. $\partial_t n_m = 0$ for all m at a fixed external current density j (cf. Fig. 3.2). Let us denote by m_p the well with the highest electron concentration (for Fig. 3.2 we have $m_p = 51$). The individual well-to-well characteristics close to m_p are shown in Fig. 3.7.

We see that by approaching the front from the emitter side, we first observe an almost homogeneous characteristic (blue line in Fig. 3.7) and a current density electric field operating point close to (F^l, j) (blue square). But already at the next barrier the current density characteristic $j_{m_p-1 \rightarrow m_p}(F)$ (cyan line) shows a suppressed low field peak. This is due to the large electron concentration at well m_p inhibiting the tunneling of electrons into well m_p , as discussed in Sec. 2.2.1. Since

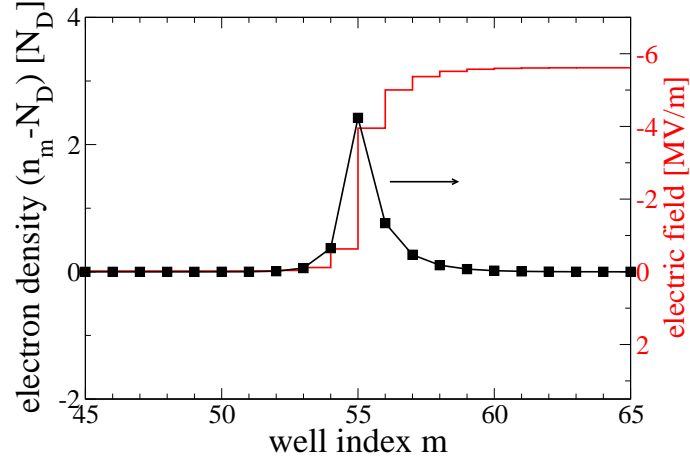


Figure 3.8: Electron density (black) and electric field (red) profile for a charge accumulation front moving in positive direction at constant current $j = -2.0 \text{ A/mm}^2$.

the electric fields are constant in time, we conclude from (3.1.11) that in particular $j_{m_p-1 \rightarrow m_p} = j$, while the electric field F_{m_p-1} is larger than F^l (cyan square). At the next barrier the current density takes advantage of the large electron density n_{m_p} which yields a characteristic $j_{m_p \rightarrow m_p+1}(F)$ (magenta line). The electric field F_{m_p} (magenta square) has increased by a large amount due to $n_{m_p} > N_D$, but the current is fixed at $j_{m_p \rightarrow m_p+1} = j$. For even larger m the characteristic again approaches the homogeneous characteristic and the operating point is close to (F^h, j) . Since at any barrier we have $j_{m_p \rightarrow m_p+1} = j$, the total velocity of the front is zero according to (3.1.10). Note that none of the operating points is located at the unstable branch with negative differential conductivity. This is only possible in a discrete system, where the field changes by a finite amount from one barrier to the next. It thus follows, that stationary fronts of this type can not appear in a continuous system, since there the branch with negative differential conductivity can not be avoided.

3.1.4 Accumulation Front with Positive Velocity

By lowering the external current j we arrive at well-to-well characteristics as in Fig. 3.9. By comparing with Fig. 3.7 we note that the characteristics themselves did not change considerably, but only the imposed external current j (green line) is lowered. In particular there is now no operating point, at which the characteristic $j_{m_p \rightarrow m_p+1}(F)$ could assume j , i.e the magenta characteristic and the green line in Fig. 3.9 do not intersect. Instead we have $j_{m_p \rightarrow m_p+1}(F_{m_p}) < j$, which results in a positive velocity by (3.1.10).

In order to estimate the velocity of the accumulation front with positive velocity it is instructive to look once more at the *stationary* case, just before the front starts to move. The corresponding characteristics for the minimal stationary current $j_{\min}^s =$

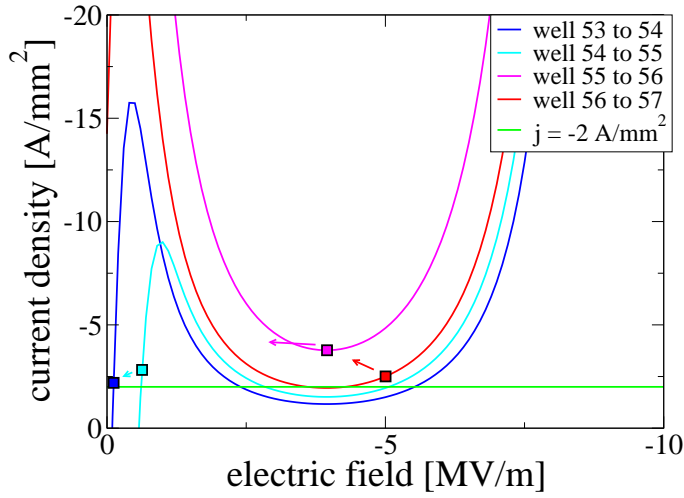


Figure 3.9: Well to well characteristics for a right moving charge accumulation front at $j = -2.0 \text{ A/mm}^2$ (profile in Fig. 3.8).

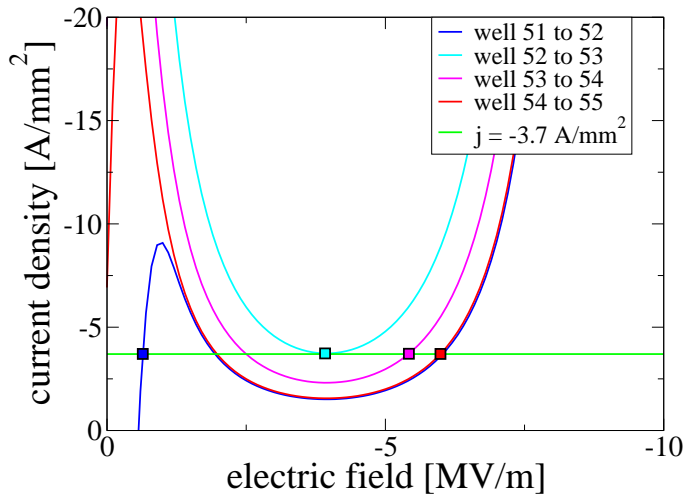


Figure 3.10: Well to well characteristics for a stationary charge accumulation front with $j = -3.7 \text{ A/mm}^2$ close to j_{\min}^s .

3 Front Dynamics in One Spatial Dimension

$-3.7\text{A}/\text{mm}^2$ is shown in Fig. 3.10. We see that now the external current density j (green line) intersects $j_{m_p \rightarrow m_p+1}(F)$ at its minimum value. We may approximate the homogeneous current density vs electric field characteristic $j_{m \rightarrow m+1}(F_m, N_D, N_D)$ for $F^h(j) < F < F_{\max}^l$ by a parabola going through (F_{\max}^l, j_{\max}^l) and with a minimum at F_{\min}^h . For the inhomogeneous case we can assume that

$$j_{m \rightarrow m+1}(F_m, n_m, n_{m+1}) \approx (n_m/N_D)j_{m \rightarrow m+1}(F_m, N_D, N_D), \quad (3.1.15)$$

which is appropriate if Pauli blocking can be neglected. This yields (in the fully degenerate limit)

$$j_{m \rightarrow m+1}(F_m, n_m, n_m + 1) \approx \frac{n_m}{N_D} \left[j_{\min}^h + (j_{\max}^l - j_{\min}^h) \left(\frac{F_m - F_{\min}^h}{F_{\max}^l - F_{\min}^h} \right)^2 \right]. \quad (3.1.16)$$

We can determine the minimal stationary current j_{\min}^s by requiring that the region with negative differential conductivity (NDC) is traversed in one step, i.e. $F_{m_p-1} \approx F_{\max}^l$ and $F_{m_p} \approx F_{\min}^h$ (see Fig. 3.10). Then we have

$$n_{m_p}(F_{m_p}) \approx N_D + \frac{\epsilon_r \epsilon_0}{e} (F_{m_p} - F_{\max}^l), \quad (3.1.17)$$

and arrive at the well know condition for stationarity [42, 72] (see also [71, 59])

$$j_{\min}^s \approx j_{m_p \rightarrow m_p+1}(F_{\min}^h, n_{m_p}, n_{m_p} + 1) \quad (3.1.18)$$

$$\approx \left[1 + \frac{\epsilon_r \epsilon_0}{e N_D} (F_{\min}^h - F_{\max}^l) \right] j_{\min}^h \approx -3.99 \text{ A}/\text{mm}^2. \quad (3.1.19)$$

which overestimates the numerical value $j_{\min}^s = -3.64 \text{ A}/\text{mm}^2$ of superlattice B slightly by about 10%.

By lowering j below j_{\min}^s the field F_{m_p} will move according to (3.1.11). We can estimate the time Δt during which F_m drops from F_{m_p} to F_{m_p-1} , which equals the time in which the front advances by one well. From (3.1.11) we obtain

$$\Delta t = \int_{F_{m_p}}^{F_{m_p-1}} \frac{\epsilon_r \epsilon_0}{j - j_{m_p \rightarrow m_p+1}(F_m, n_m, n_{m+1})} dF_m. \quad (3.1.20)$$

We can assume that the main contribution to the integral in (3.1.20) arises from the region close to $F_m \approx F_{\min}^h$, where the integrand has a maximum, while the exact choice of the boundaries is not crucial. Using the approximations (3.1.16) and (3.1.17) and the substitution

$$x = \frac{F_{m_p} - F_{\min}^h}{F_{\max}^l - F_{\min}^h}, \quad (3.1.21)$$

we get

$$\Delta t \approx -\alpha \frac{e N_D}{j_{\min}^h} \int_{-1}^1 \frac{dx}{\frac{j}{j_{\min}^h} - (1 + \alpha) + \alpha x - \beta x^2 + \alpha \beta x^3}. \quad (3.1.22)$$

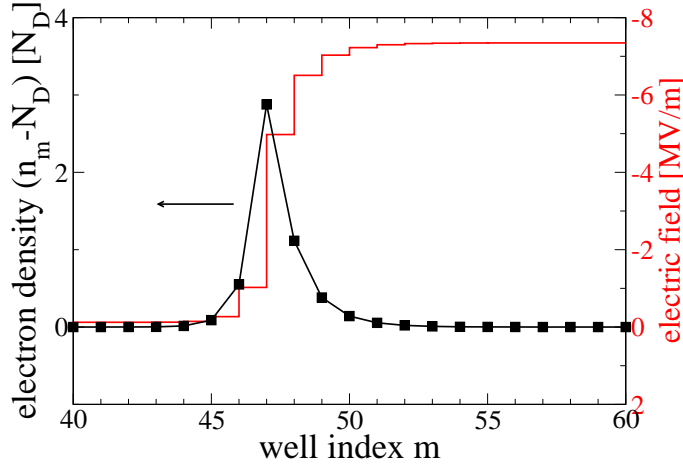


Figure 3.11: Electron density (black) and electric field (red) profile for a charge accumulation front moving in negative direction at constant current $j = -10.0 \text{ A/mm}^2$.

Here we used the abbreviations

$$\alpha = \frac{j_{\min}^s - j_{\min}^h}{j_{\min}^h} = \frac{\epsilon_r \epsilon_0}{e N_D} (F_{\min}^h - F_{\max}^l), \quad (3.1.23)$$

$$\beta = \frac{j_{\max}^l - j_{\min}^h}{j_{\min}^h}, \quad (3.1.24)$$

and for convenience integrate over the interval $[-1, 1]$. The numerical integration of (3.1.23) for given α and β is straightforward. For the parameters of superlattice B we have $\alpha \approx 2.63$ and $\beta \approx 15.0$. The velocity v_a is then obtained by

$$v_a = \frac{d}{\Delta t}, \quad (3.1.25)$$

and is plotted in Fig. 3.5 (orange line). In spite of the coarse approximations made, the analytical approximation agrees astonishingly well with the results from the numerical simulations. In particular the crossing point of the velocities of the accumulation and depletion fronts is well reproduced by the analytical approximations (3.1.25) and (3.1.14). At low values of $j \approx j_{\min}^h$ however, where the accumulation front becomes unstable, the velocity obtained from (3.1.25) underestimates v_a considerably.

3.1.5 Accumulation Front with Negative Velocity

Besides positive and zero velocities, the electron accumulation fronts show negative velocities for external currents larger than j_{\max}^s (see Fig. 3.5) [67]. For a charge accumulation front moving left, the charge and field profiles (Fig. 3.11) are very

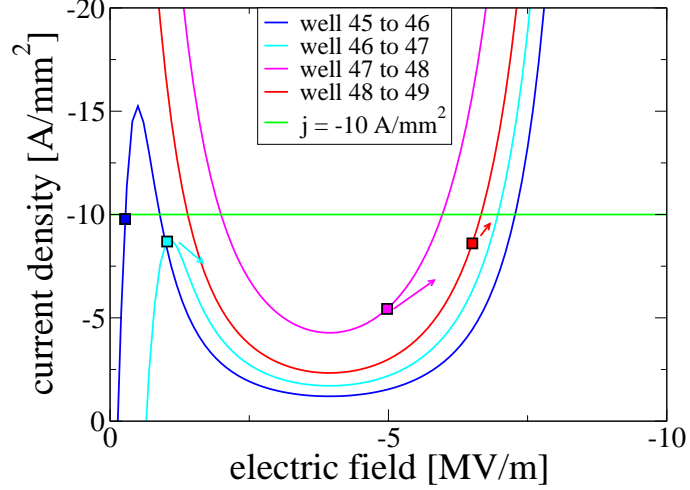


Figure 3.12: Well to well characteristics for the left moving charge accumulation front in Fig. 3.11.

similar to the stationary case (Fig. 3.2). Consequently the well to well characteristics in Fig. 3.12 are also similar to the stationary ones (Fig. 3.7) but with an external current j (horizontal green line in Fig. 3.12) at a higher value. Due to this rise of j there is now no intersection point of the characteristic $j_{m_p-1 \rightarrow m_p}(F)$ (cyan line) with j (green line) on the first branch. This means that the operating point $(j_{m_p-1 \rightarrow m_p}, F_{m_p-1})$ (cyan square) is below j and results in a negative contribution in (3.1.10). Since all other operating points are also less than or equal too j , we conclude that v_d in this regime will be negative.

In principle, it is possible to carry out a similar analysis for the negative front velocity as was done for the positive front velocities in Sec. 3.1.4. It is clear that the main contributions to an integral corresponding to (3.1.20) will now arise from the region $F \approx F_{\max}^l$, which is responsible for the moving instability. However in this case the approximation of the current density vs field characteristic close to F_{\max}^l is more complicated, since now the dependence of $j_{m \rightarrow m+1}$ on n_{m+1} can not be neglected. In particular the approximation (3.1.16) is not sufficient for negative velocities, and a diffusion term has to be included in the analysis. Since in this work we are mainly concerned with currents below j_{\min}^s we do not pursue this path any further, but refer the reader to [27], where negative velocities were analyzed in a continuous limit model.

3.2 Multiple Fronts under Fixed External Voltage

In the previous section we have studied the motion of a single front at fixed external current j far away from the contact and obtained the front velocity vs current density characteristic in Fig. 3.5. We now consider the case of several fronts, which

3.2 Multiple Fronts under Fixed External Voltage

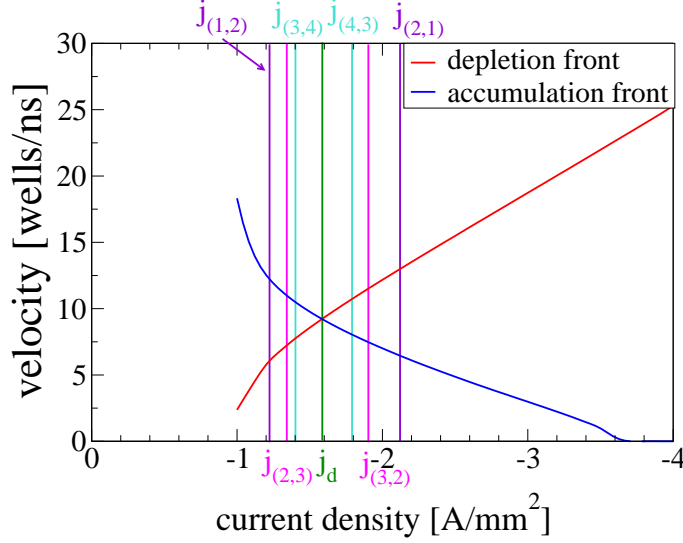


Figure 3.13: Velocity vs current density characteristic as in Fig. 3.5, in the region around j_d , where the accumulation and depletion front velocities are equal. $j_{(N_a, N_d)}$ denote the points where $N_a v_a = N_d v_d$ (cf. (3.2.2)), respectively.

are assumed to be well separated and far away from the contacts. Instead of fixing j we now fix the external voltage U , which is experimentally much more convenient.

Since the fronts are assumed to be separated, the indices m_l and m_r in (3.1.7) are well defined for each individual front, and we may therefore calculate the positions of each accumulation front $a_1 \dots a_{N_a}$ and depletion front $d_1 \dots d_{N_d}$. Here N_a and N_d are the number of accumulation and depletion fronts, respectively. Since accumulation and depletion fronts appear alternately in the vertical direction, we have

$$N_a - N_d = +1, 0, -1. \quad (3.2.1)$$

We may now conceive the superlattice as being split into $N_a + N_d$ smaller parts, each of which contains only one front. Since the total charge in each part is fixed to either Q_a or Q_d the current density at the boundaries of each part is also fixed to the same value j throughout the superlattice. We may therefore apply the results of Section 3.1 to each part separately. By summing (3.1.13) over all parts, and assuming that the external voltage U is constant we get the important relation:

$$N_a v_a(j) = N_d v_d(j). \quad (3.2.2)$$

Note that this relation is exact in the limit of well separated fronts.

If the number of fronts N_a and N_d is given, the current density j is fixed by (3.2.2). In the case $N_a = N_d$, i.e. an even number of fronts, we have $j = j_d$, where j_d is at the intersection point of $v_a(j)$ and $v_d(j)$, see Fig. 3.13. Similarly for the tripole configuration consisting of two accumulation fronts and one depletion front,

3 Front Dynamics in One Spatial Dimension

the current density $j = j_{(2,1)}$ is fixed by $2v_a(j_t) = v_d(j_t)$. For other configurations the corresponding current densities are described in Fig. 3.13. Since there is only a countable set of configurations, the set of possible j is discrete with j_d being the only limit point.

With this knowledge we can now explain the current density trace of Fig. 3.1(b), which alternates between a dipole and a tripole configuration. For a dipole configuration with one accumulation and one depletion front, the averaged current density is fixed to the constant value j_d , while in the tripole configuration with two depletion and one accumulation fronts, we obtain $j = j_{(2,1)}$ as predicted from (3.2.2). In this context it is instructive to realize the meaning of (3.2.2) directly from the field evolution (middle panel of Fig. 3.1(b)) in the tripole phase. Due to the fixed voltage, the total length of the red high field domain is required to be constant. Since the high field domain shrinks with the motion of the two accumulation fronts and increases by the depletion front, the velocity of the depletion front obviously has to be twice the velocity of the accumulation fronts.

In contrast to the averaged current density, the raw current density data (cyan line in Fig. 3.1(b)) shows rapid spikes which are due to the discreteness of the superlattice [52] (well-to-well hopping of charge packets, cf. [73]).

In the current density trace of Fig. 3.1(a) we also observe plateaus corresponding to the currents density $j_{(1,2)}$, $j_{(2,3)}$, $j_{(3,4)}$ and j_d , although they are not as flat and well developed as in Fig. 3.1(b). The reason for this difference will become clearer in Chapter 4.

3.3 Front Generation and Annihilation

So far we have only considered the free motion of charge fronts well separated from each other and the contacts. But for interesting dynamical scenarios as for example in Fig. 3.1(a), we also need front generation and front annihilation processes.

3.3.1 Front Injection at the Emitter

In the superlattices under consideration, both types of fronts are in general only generated at the emitter. We will see that the choice of the boundary conditions, as well as the imposed external current j play a decisive role for the front generation. For convenience we assume that the emitter contact is Ohmic (2.3.1),

$$j_{0 \rightarrow 1}(F_0) = \sigma F_0, \quad (3.3.1)$$

with σ the contact conductivity, and F_0 the electric field between the emitter and the first well. In the following we will choose σ such that the linear contact characteristic $j_{0 \rightarrow 1}(F_0)$ intersects the N -shaped homogeneous characteristic $j_{1 \rightarrow 2}(F_1, N_D, N_D)$ at a point (F_c, j_c) on its branch with negative differential conductivity (see Fig. 3.14).

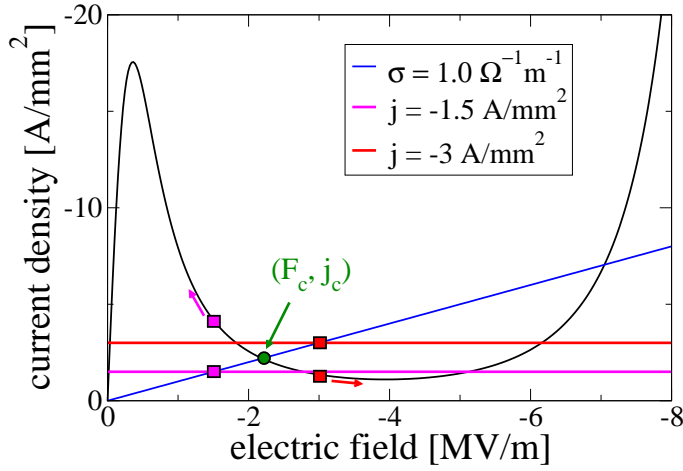


Figure 3.14: Emitter current density characteristic compared to homogeneous well to well characteristic $j_{m \rightarrow m+1}(F, N_D, N_D)$. The intersection point of the two characteristics is denoted by (F_c, j_c) .

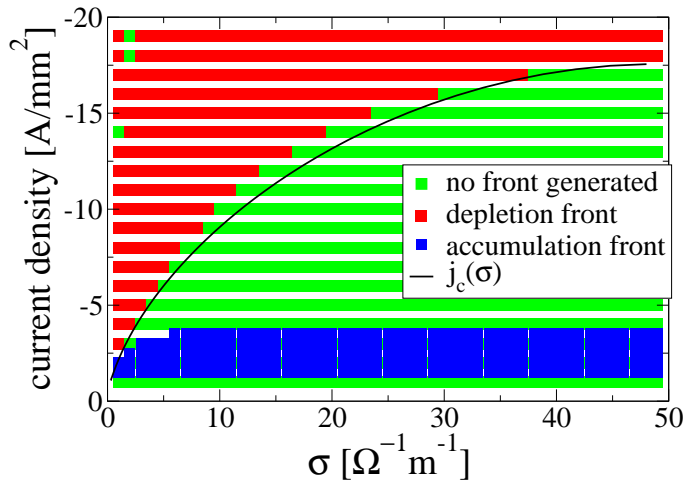


Figure 3.15: Intersection point of the homogeneous characteristic with the emitter characteristic $j_c(\sigma)$. The red (blue) squares denote a successful generation of a depletion (accumulation) front at the emitter. The green squares denote that no moving front was generated.

3 Front Dynamics in One Spatial Dimension

Let us consider a superlattice under fixed external current density j , with initial conditions

$$n_i(t=0) = N_D; \quad F_0(t=0) = j/\sigma. \quad (3.3.2)$$

It follows from (3.1.11) that F_0 is a stable fixed point. From (3.0.2) we see that $F_1(t=0) = F_0$. Let us first assume that j is larger than j_c (red horizontal line in Fig. 3.14). In this case F_0 and $F_1(t=0)$ are larger than F_c (red squares in Fig. 3.14), which means that

$$|j_{1 \rightarrow 2}| < |j_c| < |j| = |j_{0 \rightarrow 1}|. \quad (3.3.3)$$

Consequently, $F_1(t)$ will *increase* towards higher values due to (3.1.11) until it eventually reaches $F_1 \approx F^h(j)$ ². If on the other hand j is smaller than j_c (magenta line in Fig. 3.14) $F_1(t)$ will *decrease* for complementary reasons (magenta squares). It is now apparent that the choice of the external current j in comparison to the intersection point j_c is crucial. From the above discussion we come to the conclusions that

$$|j| > |j_c| \Rightarrow \text{high field at emitter, i.e. } F_1(t \gg 0) \approx F^h(j), \quad (3.3.4)$$

$$|j| < |j_c| \Rightarrow \text{low field at emitter, i.e. } F_1(t \gg 0) \approx F^l(j). \quad (3.3.5)$$

We may now argue that (3.3.4) and (3.3.5) are still approximately valid, even if the initial conditions (3.3.2) are not fulfilled. Let us consider a superlattice at a fixed external current j , which initially contains an accumulation front at a position p_a far away from the boundary, and possibly further fronts at positions $p > p_a$. Then the region to the left of p_a including the emitter region is in the low field domain. If j is larger than j_c the emitter region is required to be at a high field by (3.3.4). This apparent ‘‘conflict’’ can be resolved by the dynamic generation of a new charge depletion front at the emitter. A converse argument applies for the generation of an accumulation front. The preliminary rules for the front generation can therefore be summarized by

GI Generate accumulation front at emitter, if $|j| < |j_c|$ and if the leftmost front is a depletion front.

GII Generate depletion front at emitter, if $|j| > |j_c|$ and if the leftmost front is an accumulation front.

In Fig. 3.15 we checked numerically that the approximations leading to rules GI, GII are justified, by examining the front generation for different values of j and σ . We see that the conditions for depletion front generation can be accurately predicted by GII. In the case of the generation of accumulation fronts, GI can only be checked for currents $|j| < |j_{\min}^s|$ (Fig. 3.5), since otherwise the newly generated front has zero or negative velocity and will not detach from the emitter.

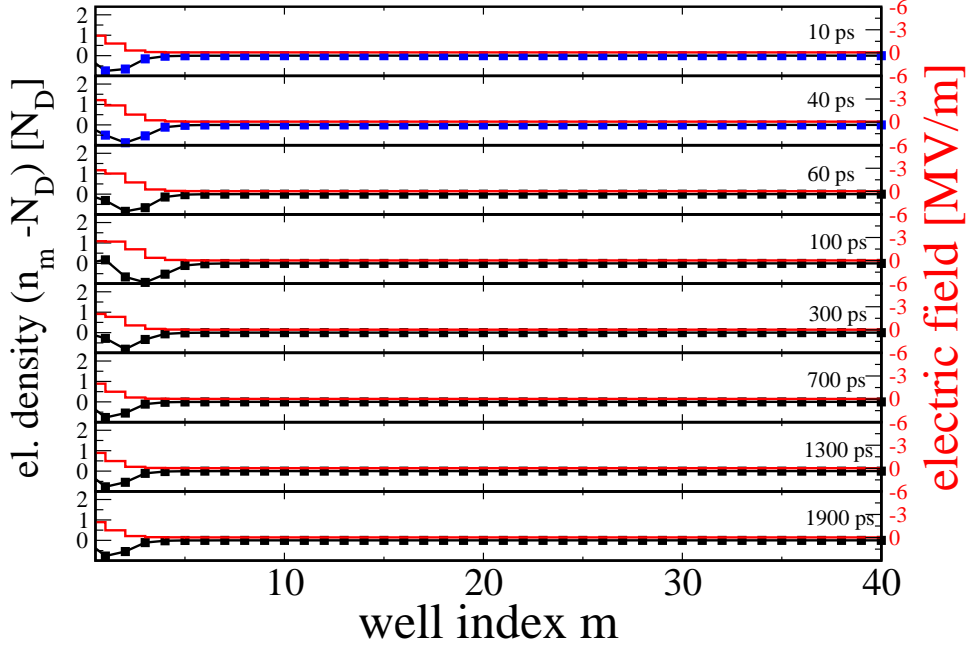


Figure 3.16: Electron density and electric field profiles for superlattice B with $\sigma = 1 \Omega^{-1}\text{m}^{-1}$ at different points in time for the first 40 wells. For $0 \leq t \leq 40$ ps the emitter is in the low field domain, i.e. the leftmost front (not plotted) is an accumulation front and $|j| > |j_c|$. A depletion front starts to form at the emitter (blue squares). At $t = 40$ ps the external current is switched to $|j| < |j_c|$ and the depletion front retracts to the emitter and the front generation is not successful.

Rules GI, GII only apply if the leftmost front is already fully detached from the emitter. Otherwise the newly generated front can annihilate a nearby front of opposite polarity. This may occur in the common scenario of a dipole injection as shown in Fig. 3.16. Here for $t < 40$ ps the conditions of rule GII are fulfilled, and a depletion front starts to form. But before the depletion front is fully developed, we switch the external current, such that GI applies. We see that in this case the half formed depletion front retracts to the emitter contact. This is in contrast to the scenario in Fig. 3.17, where the switching to the conditions of GI occurs at $t = 60$ ps. By that time, the depletion front has reached a critical size, which allows it to be detached from the emitter. Together with the subsequently generated accumulation front, a dipole is generated.

The rule GI for the generation of an accumulation front should therefore be modified, to require that the leftmost depletion front is at least $p_h \approx 2d$ away from the emitter and a similar parameter p_l should be introduced into GII. The revised

² F_1 is not exactly equal to $F^h(j)$, since for $t > 0$ we have $n_1 > N_D$. Therefore $j_{1 \rightarrow 2}$ does not obey the homogeneous characteristic and its high field intersection point with the external current j will be between F_{\min}^h and $F^h(j)$.

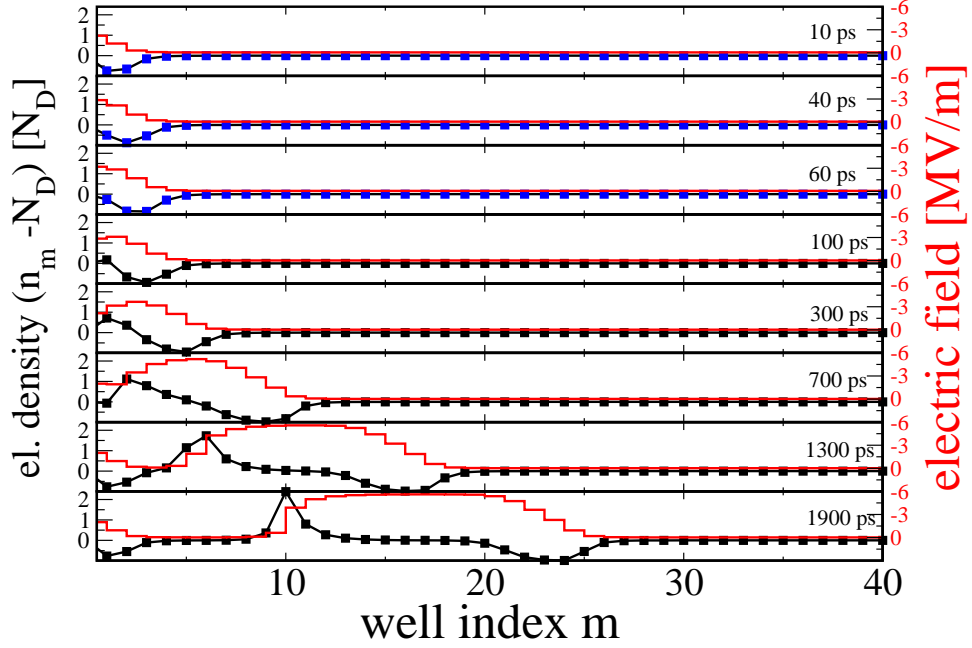


Figure 3.17: Same scenario as in Fig. 3.16, but j is switched at $t = 60$ ps. A dipole, consisting of a leading depletion front and a trailing accumulation front is successfully injected at the emitter.

rules for front generation at the emitter then read:

- GI' Generate accumulation front at emitter, if $|j| < |j_c|$ and if the leftmost front is a depletion front which is at least at position p_h .
- GII' Generate depletion front at emitter, if $|j| > |j_c|$ and if the leftmost front is an accumulation front which is at least at position p_l .

We may now reexamine the scenario in Fig. 3.1(b). At $t = 157$ ns we have a dipole configuration with a leading depletion and a trailing accumulation front. The current is therefore $j = j_d$. At $t = 160$ ns the depletion front reaches the collector, i.e. $N_d = 0$. Then (3.2.2) requires that the velocity of the remaining accumulation front drops to zero, and at the same time the current rises sharply due to Fig. 3.13. Eventually we have $|j| > |j_c| = 2.6$ A/mm² and a depletion front is injected at the emitter by GII'. After that j starts to drop towards j_d , but as soon as $|j| < |j_c|$, and the depletion front has traveled by p_h , the conditions for GI' are fulfilled, and a new accumulation front is injected at the emitter at $t = 161$ ns. All in all we see that the system responds to the event that the first depletion front hits the collector, by the generation of a dipole with a leading depletion and trailing accumulation front at the emitter. For the resulting tripole configuration, the current $j_{(2,1)}$ is required (see Fig. 3.13). Since $|j_{(2,1)}| < |j_c|$ and the leftmost front is an accumulation front, no new fronts will be generated (see GI', GII'), and a

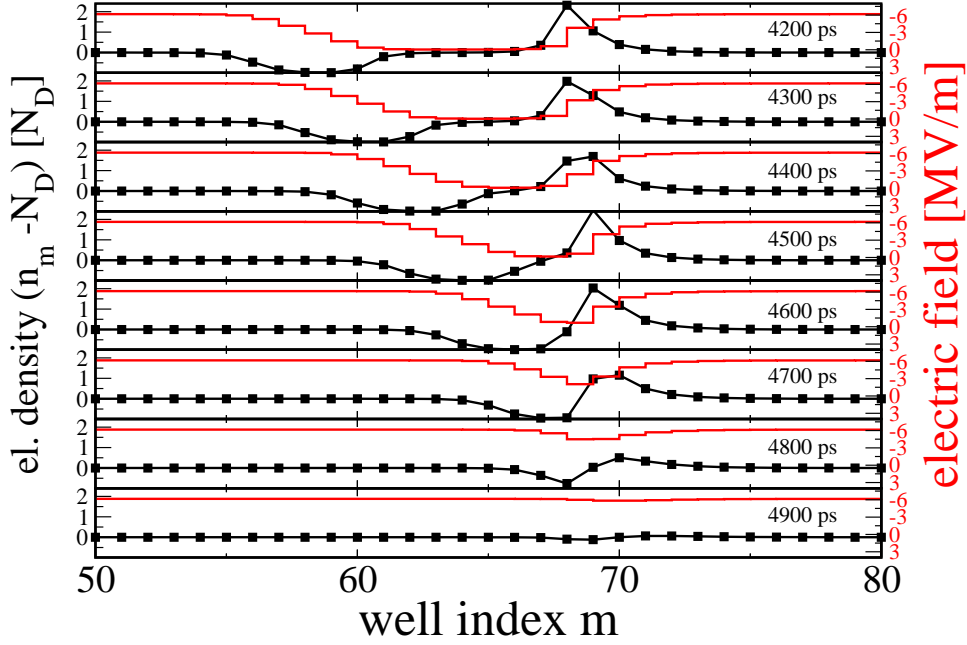


Figure 3.18: Electron density and electric field profiles for a collision and annihilation process of a fast depletion front with a slow accumulation front. Parameters: $\sigma = 1 \Omega^{-1}\text{m}^{-1}$; $j = -3 \text{ A/mm}^2$.

current plateau with $j = j_{(2,1)}$ is maintained until the rightmost accumulation front hits the collector at $t = 163 \text{ ns}$. The current then drops to j_d , but no new front is generated at the emitter, until the cycle starts over again with the next depletion front reaching the collector at $t = 170 \text{ ns}$.

3.3.2 Front Collisions

From the current velocity characteristic Fig. 3.13 and from (3.2.2) we conclude that the accumulation and depletion fronts may move at different velocities. This opens up the possibility for a collision of two fronts with opposite polarity, and may lead to interesting scenarios. Such a collision is shown in Fig. 3.18. We see that both fronts annihilate each other, as can be expected from the fact that $Q_a = -Q_d$.

A basic example, where the collision of opposite fronts plays a role, is shown in Fig. 3.19. This scenario resembles Fig. 3.1(b), since it also exhibits a tripole configuration with two accumulation and one depletion fronts with the corresponding current plateau $j = j_{(2,1)}$ (see Fig. 3.13). But now the fast depletion front catches up with the rightmost accumulation front before it reaches the collector, and those two fronts annihilate. The remaining accumulation front now triggers the generation of a dipole at the emitter, as explained in the previous subsection for Fig. 3.1(b). At any time we have an odd number of fronts present in the system, which explains, why the current does not reach j_d .

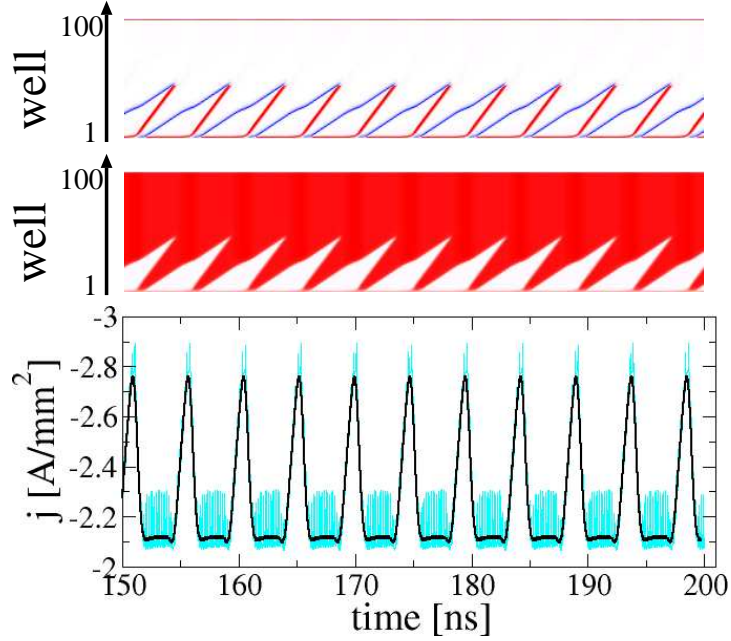


Figure 3.19: Front evolution as in Fig. 3.1, but for $U = 6 \text{ V}$ and $\sigma = 1.3 \Omega^{-1}\text{m}^{-1}$.

3.3.3 Front Annihilation at the Collector

A further rather unspectacular elementary process is a front reaching the collector. Such a front gets absorbed in the contact and vanishes from the system, thereby reducing N_a or N_d by one.

This concludes the set of elementary front processes, and we will see in the next chapter, how they can be deployed to describe a large part of the dynamical bifurcation scenarios found in superlattices. We stress however that here we only considered fully developed fronts and new interesting scenarios are expected, if we also take into account partly developed fronts. Since such fronts are not individually stable, and often occur in combination with other fronts, an analysis of such phenomena is rather complicated, and more likely to be specific for one particular set of parameters.

4 Chaotic Front Dynamics

Simplification good!
Oversimplification bad!

(Larry Wall)

In Chapter 3 we have studied the basic building blocks for the front dynamics in one spatial dimension. In this chapter we will examine how those elements can be combined to yield interesting bifurcation scenarios, including chaos. While chaoticity in periodically driven superlattices has been extensively studied theoretically [74, 75, 76, 77, 78] and experimentally [79, 80] we will concentrate on the question, how chaotic behavior can be obtained under fixed external voltage conditions [81, 23].

For a fundamental understanding of the underlying bifurcations we will introduce the *front model*, which retains the basic bifurcation structure, but is much easier to handle numerically and analytically.

4.1 Bifurcation Scenarios of the Microscopic Model

We consider an $N = 100$ period superlattice of type B (cf. Table 2.2 on page 12), and use the external voltage U and the contact conductivity σ as the bifurcation parameters. From the discussion in Sec. 3.3.1 we learned that σ governs the injection of fronts at the emitter contact via the critical current $j_c(\sigma)$ (Fig. 3.15). Since the resulting bifurcation scenarios are complicated, we will first study the particular case of $\sigma = 0.5 (\Omega\text{m})^{-1}$, and later consider the necessary modifications for general σ .

4.1.1 The Case $\sigma = 0.5 (\Omega\text{m})^{-1}$

For $\sigma = 0.5 (\Omega\text{m})^{-1}$ we have $|j_{(1,2)}| < |j_c(\sigma)| < |j_d|$ (c.f Fig. 3.13). If we vary the applied voltage U , we typically observe front patterns as in Fig. 4.1, which are reminiscent of the chaotic front dynamics in the Gunn-diode [82]. For a small voltage ($U = 0.50$ V) we observe that the fronts are generated as dipoles at the emitter, with a leading accumulation and a trailing depletion front. The leading accumulation front catches up with the depletion front of the preceding dipole, and the two fronts merge and annihilate at exactly the same position in each cycle. This scenario corresponds to the one in Fig. 3.19, with the role of the accumulation and depletion

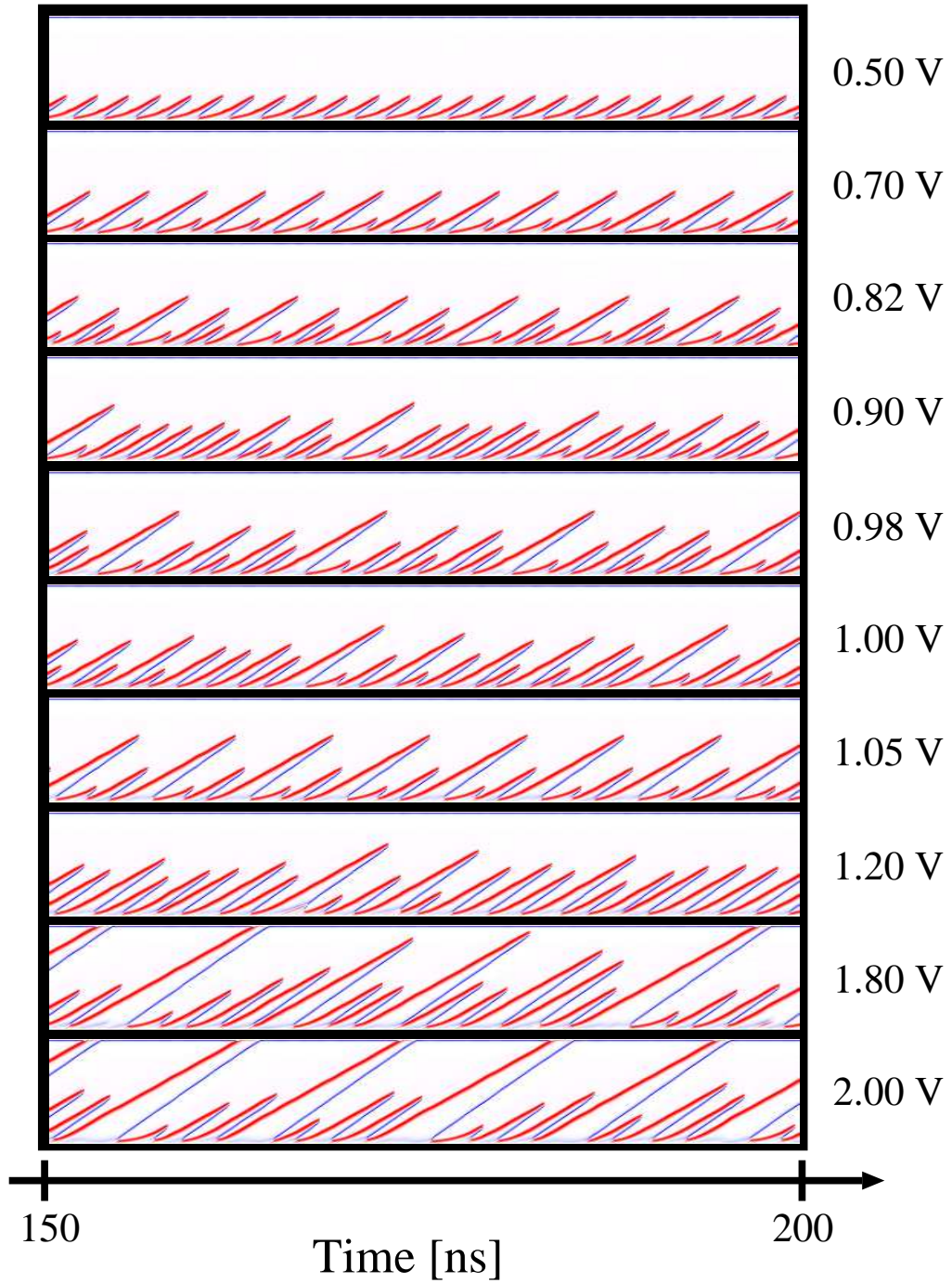


Figure 4.1: Dynamic evolution of the charge density for various voltages at $\sigma = 0.5 \Omega^{-1} \text{m}^{-1}$ in a superlattice of type B with $N = 100$ wells (space-time plots). Regions of electron accumulation and depletion are denoted by blue and red, respectively. In each panel the emitter (collector) is located at the lower (upper) edge.

fronts reversed. With increasing U , we observe what appears to be a period doubling cascade, with two ($U = 0.70$ V in Fig. 4.1) and four ($U = 0.82$ V) alternating positions where the front annihilation occurs. A further increase in the voltage yields irregular behavior ($U = 0.90$ V, 1.00 V, 1.20 V) interrupted by periodic windows ($U = 1.05$ V). For even higher voltages, the fronts may occasionally reach the collector, but even then the interchange between chaotic ($U = 1.80$ V) and periodic ($U = 2.00$ V) regimes persists.

The chaotic behavior can also be observed in the experimentally accessible current trace, as demonstrated in Fig. 4.2. Here we observe a further interesting feature, namely that not all fronts are *fully developed*. One example can be seen at $t = 155$ ns in the electron density plot of Fig. 4.2 (see also the case $U = 1.2$ V in Fig. 4.1). Here an accumulation front seems to detach from the emitter, but instead of catching up with the leading depletion front, it merges with a new depletion front from the emitter, before either of the fronts can be considered as fully developed. Such compositions of partly developed fronts can not be described in the framework of single stable fronts, which was developed in Chapter 3. In particular they do not obey the current velocity characteristic of Fig. 3.13. Such composite front phenomena, resemble the excitons in solid state physics, since they often appear in pairs without net charge, and form a bound state with limited life time. Their dynamics may be treated by a yet to be developed correlated front theory, which is however beyond the scope of the present work. In the following we will refer to this kind of phenomena as *excitonic* fronts. Similar effects also appear for pulses in excitable media [83].

The difference between periodic and chaotic behavior is also illustrated by the phase portraits as shown in Fig. 4.3, which show the system trajectory in the phase space projected onto the subspace defined by n_{10} and n_{20} . In Fig. 4.3(a) the trajectory in the phase space is complicated, but still periodic, while in the chaotic regime in Fig. 4.3(b) the trajectory is aperiodic.

The full bifurcation scenario is shown in Fig. 4.4(a), where for each voltage U the set of front annihilation positions $\{p_c\}$ is plotted. Here we may interpret a discrete set of p_c 's for a given voltage as an indication for periodic behavior (for instance the four points at $U = 0.82$ V, which correspond to a period four orbit), while a continuous set of collision points is an indication of chaotic behavior (cf. $U = 0.90$ V).

Starting from low voltages, we observe a period doubling bifurcation with periods 1, 2 and 4 in the regions A, B, and C of Fig. 4.4(a), respectively. The following region D contains two chaotic bands at its boundaries, which are separated by a period six orbit. While the chaotic band at the left edge of region D is rather narrow, the band at the right edge is comparatively broad. The most striking feature in region D is the center of a crossing of at least three straight lines, which in the following will be called a *cobweb* structure. In this case the cobweb is located in the chaotic band at the right edge of region D. This chaotic band ends with the transition to the period 4 behavior in region E. The following region F is again chaotic, and

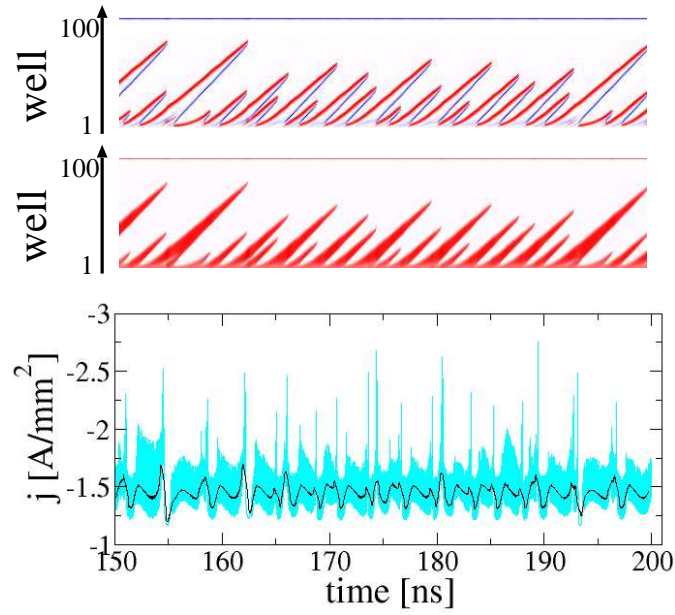


Figure 4.2: Electron density (upper panel), electric field (middle panel) and current evolution (bottom panel) in the chaotic regime. Parameters as in Fig. 4.1, but with $U = 1.15$ V. The color code is explained in Fig. 3.1. The black current trace in the bottom panel is the running average of the raw current data (cyan line) over an interval of 0.5 ns.

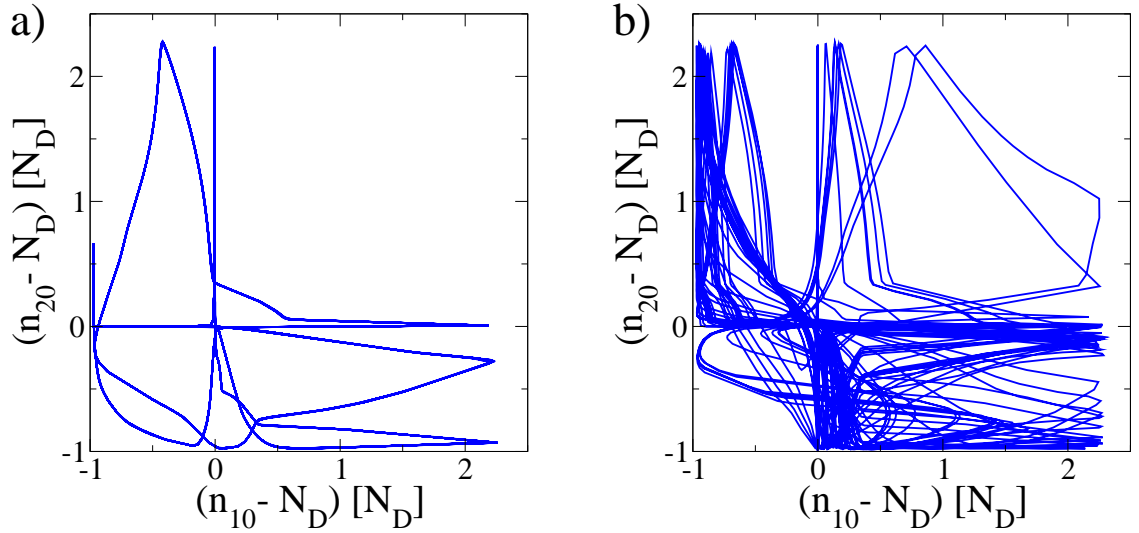


Figure 4.3: Phase portrait of the electron densities n_{20} vs. n_{10} for superlattice parameters as in Fig. 4.1 for time series from $t = 50 \dots 200$ ns. (a) periodic behavior at $U = 0.82$ V, (b) chaotic behavior at $U = 1.15$ V.

is bounded by the larger period three region G. In regions A to G we observe a number of continuous and almost straight lines, which exist across various regions, even in the chaotic regimes. These lines also give rise to the cobweb structure with its center in region D.

In the following voltage interval H in Fig. 4.4, we observe collisions close to the emitter. They are the footprints of the annihilation of excitonic fronts, as discussed before. Note however that the numerical method for collision detection only works reliably for well numbers $m > 5$, which may limit our ability to detect excitonic collisions which occur very close to the emitter. In region I fronts occasionally reach the collector, and we observe a dynamics with seven distinct collision points. The excitonic collisions are suppressed in this region, but they reappear in region J, where we have fronts reaching the collector and excitonic collisions.

In principle, the position of collision p_c is a real number, but in practice it is difficult to determine p_c with an error which is less than the width of the accumulation front (cf. Fig. 3.18). To distinguish between chaotic and periodic behavior, we may therefore consider a suitable Poincaré section of one of the continuous dynamical system variables. This is shown in Fig. 4.4(b) for the time difference between two consecutive maxima of the electron density in well 20, $n_{20}(t)$. This bifurcation shows the chaotic bands at the same locations as in Fig. 4.4(a) (note however the different voltage scale). We observe that chaotic and periodic behavior alternate up to a voltage of about $U = 3.6$ V, which corresponds to the case where about half of the superlattice is in the high field regime. For $U > 3.6$ V, the chaoticity suddenly disappears. From Fig. 4.5 we see that the reason for this change is associated with the transition from an operation mode, in which every third high field tongue reaches the collector ($U = 3.55$ V in Fig. 4.5) to a mode where only every second high field tongue reaches the collector ($U = 3.65$ V). For even higher voltages, no collisions occur, and all fronts reach the collector (cf. $U = 5.0$ V).

4.1.2 Varying σ

Now that we have an idea of the bifurcations appearing for $\sigma = 0.5 (\Omega\text{m})^{-1}$, we proceed to the case of general contact conductivity. As we have learned in Sec. 3.3.1, the parameter σ governs the injection of fronts at the emitter. From the analysis of the case $\sigma = 0.5 (\Omega\text{m})^{-1}$ we see that the excitonic regimes (regions H and J in Fig. 4.4(a)) complicate the analysis, and it would be nice if we could avoid them. This is addressed by choosing a slightly lower contact conductivity $\sigma = 0.45 (\Omega\text{m})^{-1}$, which leads to a lower critical current density, such that the condition $|j_{(1,2)}| < |j_c(\sigma)| < |j_{(2,3)}|$ holds. Furthermore, since the simplified models we will propose below are most successful in the regimes where no fronts reach the collector, we may also choose a longer superlattice. In Fig. 4.6 the bifurcation diagram for a $\sigma = 0.45 (\Omega\text{m})^{-1}$ and $N = 200$ well superlattice is shown. We see that the regions A to G show the same behavior as the corresponding regions in Fig. 4.4(a). However the excitonic regions have disappeared, and instead we observe a period 6 regime

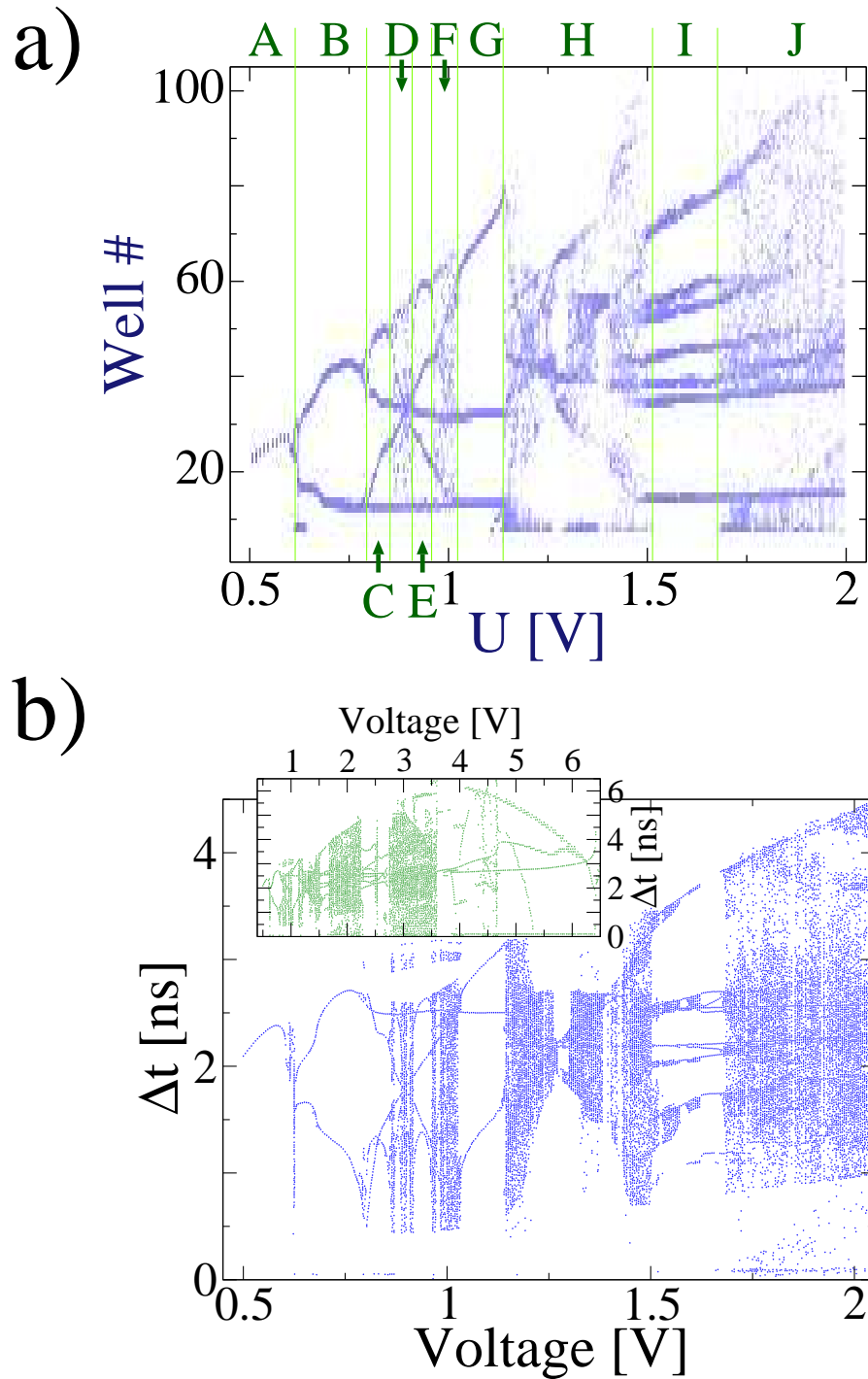


Figure 4.4: (a) Positions where accumulation and depletion fronts annihilate vs voltage at $\sigma = 0.5 \Omega^{-1}\text{m}^{-1}$. The color scale indicates high (blue) and low (white) numbers of annihilations at a given well. (b) Time differences between consecutive maxima of the electron density in well no. 20 ($n_{20}(t)$) vs voltage at $\sigma = 0.5 \Omega^{-1}\text{m}^{-1}$. Time series of length 600 ns have been used for each value of the voltage. The inset in (b) shows the time differences for a larger voltage range. Source: [81, 23].

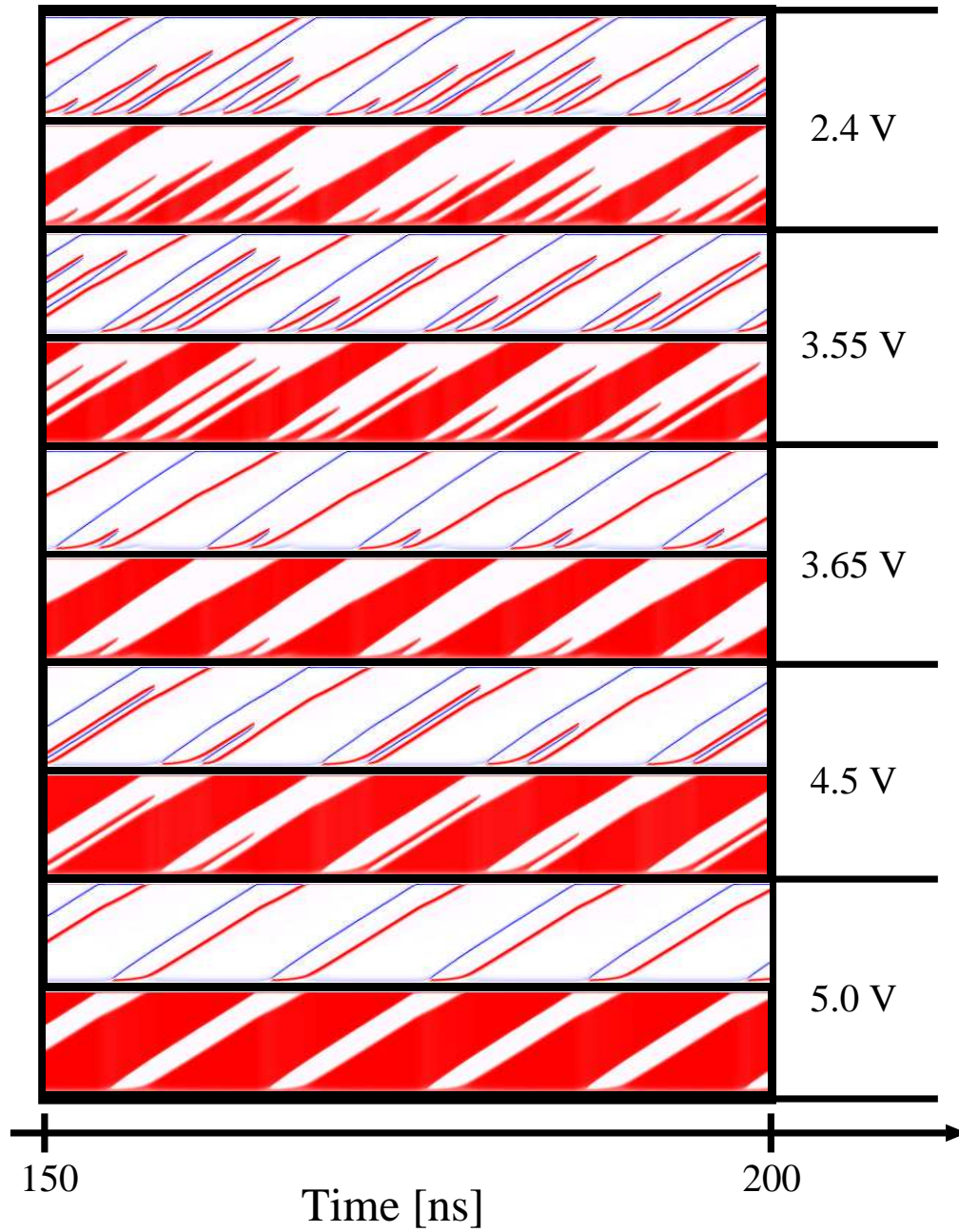


Figure 4.5: Dynamic evolution of the charge densities (upper panels) and electric fields (lower panels) for various voltages. Parameters are as in Fig. 4.1, color code as in Fig. 3.1.

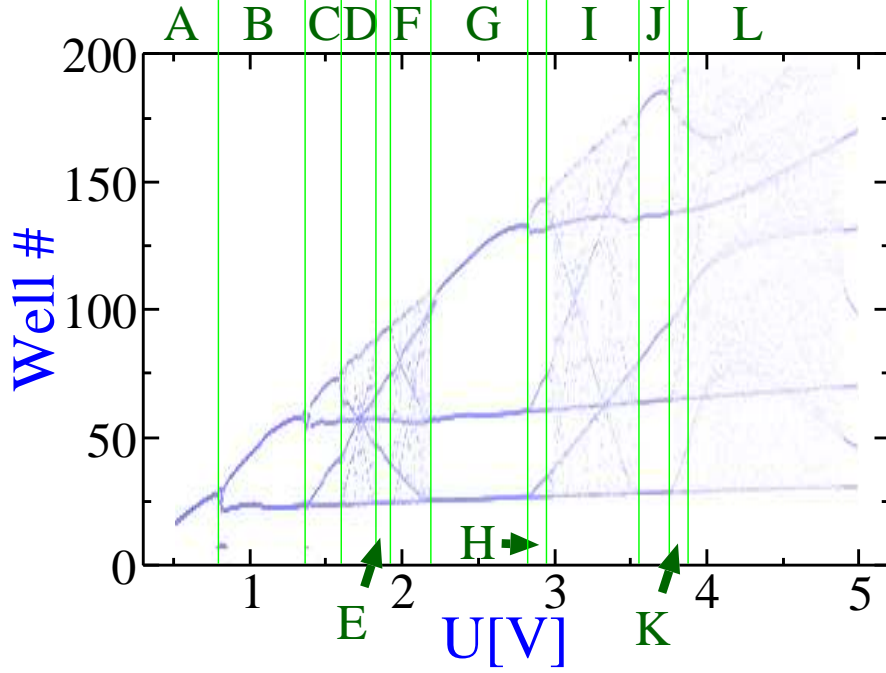


Figure 4.6: Bifurcation diagram as in Fig. 4.4(a), but with $N = 200$ and $\sigma = 0.45 \text{ } \Omega^{-1}\text{m}^{-1}$. From [84]. Other parameters as superlattice B (Table 2.2).

in region H. Region I shows chaotic behavior, except for a small period 7 band at its center. Furthermore we find a second cobweb structure in region I, which shares its horizontal line with the first cobweb in region D. The next region J has period 5. This is followed by a small chaotic region K, before the fronts start to reach the collector in region L. Note how again straight continuous lines run through the whole bifurcation diagram, and are then inflected as they reach the K region. The origins of the rich bifurcation scenario apparent in Fig. 4.6, including the chaotic bands, the cobweb structures and the sequence of the various periods will be explained by analytical considerations in Chapter 5.

We have seen that a small variation in σ has already a nontrivial effect on the bifurcation diagrams (Fig. 4.4 vs. Fig. 4.6). We may now ask, how the bifurcation diagram changes, as we further vary the contact conductivity. Since the calculation of the bifurcation diagrams is time consuming, we again use the short superlattice, with $N = 100$ wells. An overview of the different bifurcation scenarios for varying σ is given in Fig. 4.7. We note that for $\sigma = 0.4 (\Omega\text{m})^{-1}$ the scenario resembles the situation in regions A and B of Fig. 4.4, which corresponds to the periodic tripole configurations as in the first two panels of Fig. 4.1. We find the well known cobweb structure for $\sigma = 0.45, \dots, 0.52 (\Omega\text{m})^{-1}$, which however shifts to lower voltages and lower well numbers as σ increases. For $\sigma = 0.54 (\Omega\text{m})^{-1}$, the scenario seems to have fundamentally changed. The cobweb has disappeared the collisions close

to the emitter indicate the presence of excitonic fronts. Also the familiar period three window has disappeared, and instead we find a large period four window, with three collision points in the sample, and every fourth front reaching the collector. A small increase to $\sigma = 0.55 (\Omega\text{m})^{-1}$ again changes the bifurcation diagram completely. Fronts reach the collector already at voltages below 1V, and at the same time front collisions take place close to the emitter. There are now only very few continuous lines present, and the whole structure appears to be washed out. This trend continues for $\sigma = 0.57 (\Omega\text{m})^{-1}$. The bifurcation diagram for $\sigma = 0.60 (\Omega\text{m})^{-1}$ is missing in Fig. 4.7. The reason is that in this case no collisions within the sample occur. We have $j_c \approx j_d$, which means that we are at the symmetry point, where accumulation and depletion fronts have equal rights. At any time there are two fronts in the sample, which move in parallel, until the leading front reaches the collector and reappears at the emitter.

By further increasing σ , we enter the regime, where the depletion fronts are faster than the accumulation fronts. In this case it is numerically more difficult to detect the position of the annihilation with high accuracy. Thus the lines in Fig. 4.7 for $\sigma \geq 0.65 (\Omega\text{m})^{-1}$ are in general broader than before. Nevertheless the cobweb structure at $\sigma = 0.8 (\Omega\text{m})^{-1}$ is clearly visible, and also somewhat weaker for $\sigma = 0.75 (\Omega\text{m})^{-1}$. These cobwebs resemble the cobweb found at $\sigma = 0.45 (\Omega\text{m})^{-1}$ (Fig.4.6), but is flipped along the voltage axis. This is a consequence of the symmetry transformation, which we discuss below. Another interesting feature is the reconnection of the period doubling bifurcation, which occurs at $\sigma = 0.7 (\Omega\text{m})^{-1}$ and $\sigma = 0.65 (\Omega\text{m})^{-1}$, and causes a distinct bubble like structure in the bifurcation diagram.

It is now interesting to plot a “phase-diagram” of chaotic behavior in the (U, σ) -plane as shown in Fig. 4.8, which was obtained by considering the autocorrelation function $C(\tau) = \langle n_{20}(t)n_{20}(t+\tau) \rangle_t$ [23]. For periodic behavior $C(\tau)$ does not decay even for large values of $\tau > 20$ ns, while for chaotic behavior $C(\tau)$ decays with a correlation time less than 20 ns. We note that chaotic behavior is only possible, if we choose σ such that $|j_{(1,2)}| < |j_c(\sigma)| < |j_{(2,1)}|$. Furthermore there exist two larger disjoint regions which are very roughly “point symmetric” about a point at $(U \approx 3.5 \text{ V}, \sigma \approx 0.6 \Omega^{-1}\text{m}^{-1})$. The origin of this “symmetry” is the approximate invariance of the system under the simultaneous permutation of accumulation with depletion fronts, and low field with high field domains.

4.1.3 Lyapunov Exponents

To further confirm the chaoticity, the largest Lyapunov exponent λ for $U \approx 1.15\text{V}$, $\sigma \approx 0.5 \Omega^{-1}\text{m}^{-1}$ (Fig. 4.2) was calculated for a long ($t = 0 \dots 100 \mu\text{s}$) time series of $n_{20}(t)$ [23] using the Wolf algorithm [85]. The result $\lambda = 1.1 \times 10^9 \text{ s}^{-1}$ is a clear indication of chaos.

4 Chaotic Front Dynamics

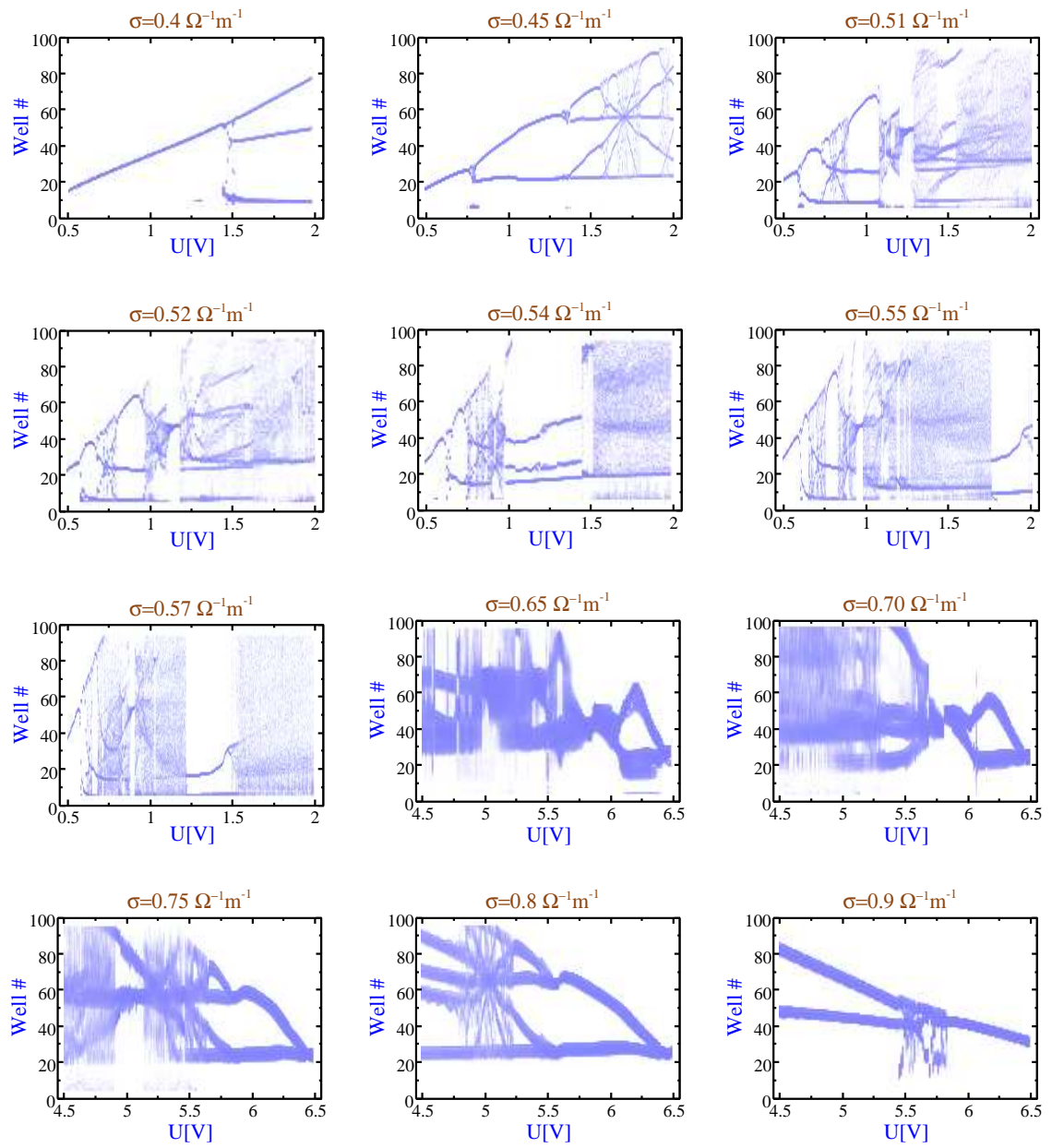


Figure 4.7: Bifurcation diagrams as in Fig. 4.4(a), for various σ .

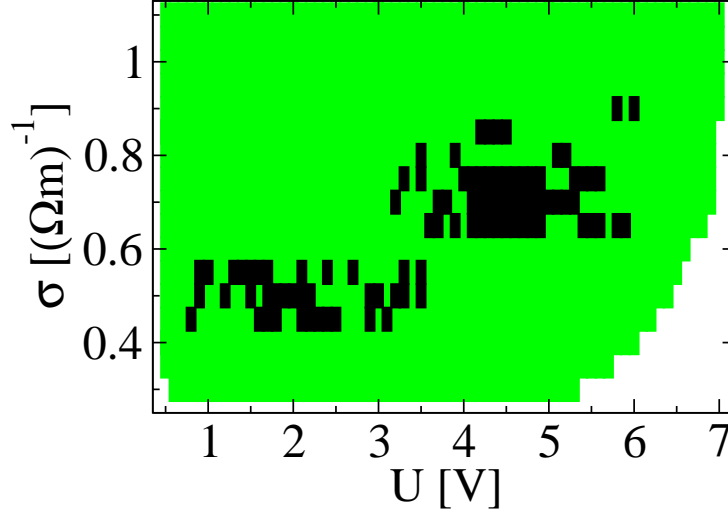


Figure 4.8: Two parameter bifurcation diagram. Black squares: chaotic behavior; green shading: periodic oscillations; white region: absence of oscillations. Source: [23].

4.2 The Front model

We are now in a position to approximate the microscopic dynamics of the electron densities n_i by means of a simple front model, in which the positions of the accumulation fronts $a_1 \dots a_{N_a}$ and the depletion fronts $d_1 \dots d_{N_d}$ and the overall current j are the new dynamical variables. Here N_a and N_d denote the number of accumulation and depletion fronts in the system. We will see that this step from the microscopic description to a front description does not only greatly reduce the dimensionality of the system, but also the number of physical parameters. The introduction of front positions was already shown to be useful in Sect. 3.2 for the case of the free motion of noninteracting fronts far away from the boundaries. We now make the assumption that the essential dynamics of the system can be described in terms of front positions, even if the fronts are close to each other or close to the boundaries. Such a “dilute gas” approximation will obviously fail if the density of fronts is large or if the typical time scale for interactions between fronts can not be assumed to be small.

4.2.1 Elimination of the current density

Let us define by

$$L_h(j) = \frac{-U - LF^l(j)}{F^h(j) - F^l(j)} \approx \frac{-U}{F^h(j)} \quad (4.2.1)$$

the partial length of the superlattice which is in the high field region. Here $L = Nd$ is the total length of the superlattice, and in the last step we have used the

4 Chaotic Front Dynamics

approximation $F^l \approx 0$. From (3.1.7) and (3.0.3) it follows that L_h imposes a global constraint on the front positions by

$$L_h(j) = \sum_{i=1}^{N_d} d_i - \sum_{i=1}^{N_a} a_i \pmod{L}. \quad (4.2.2)$$

The expression \pmod{L} in (4.2.2) means that L has to be added if $a_{N_a} > d_{N_d}$ such that $L_h \in [0, L]$. We stress that due to our center-of-mass-like definition of the front positions, (4.2.2) is exact, even for fronts with a finite width. In particular, the discreteness of the superlattice does not play a role here.

Differentiating (4.2.1) and (4.2.2) with respect to t for $U = \text{const}$ yields

$$\frac{\partial L_h}{\partial t} = \frac{-U}{(F^h)^2} \frac{\partial F^h}{\partial j} \frac{\partial j}{\partial t}, \quad (4.2.3)$$

and (using (3.1.8))

$$\frac{\partial L_h}{\partial t} = N_d v_d - N_a v_a, \quad (4.2.4)$$

respectively. By combining (4.2.3) and (4.2.4) we obtain the evolution equation for the current density,

$$\frac{\partial j}{\partial t} = (N_d v_d(j) - N_a v_a(j)) \frac{[F^h(j)]^2}{U \frac{\partial F^h}{\partial j}}. \quad (4.2.5)$$

From (4.2.5) it follows that the current will relax to a state, where (3.2.2) is fulfilled, i.e.

$$\frac{v_d(j)}{v_a(j)} = \frac{N_a}{N_d}. \quad (4.2.6)$$

From the denominator in (4.2.5) we note that this relaxation will be fast, if U and $\frac{\partial F^h}{\partial j}$ are small. For example we may consider the relaxation towards the dipole domain current density j_d with $N_d = N_a = 1$. In linear approximation we have

$$v_{a/d}(j) \approx v_{a/d}(j_d) + (j - j_d) \partial_j v_{a/d}(j_d). \quad (4.2.7)$$

From (3.1.14) we obtain $\partial_j v_d = d/(eN_D)$. From Fig. 3.13 we may further approximate (for this particular superlattice only) $\partial_j v_d(j_d) \approx -\partial_j v_a$. Using $v_a(j_d) = v_d(j_d)$ we get for the first factor in (4.2.5),

$$(N_d v_d(j) - N_a v_a(j)) \approx (j - j_d) (\partial_j v_d(j_d) - \partial_j v_a(j_d)) \approx (j - j_d) \frac{2d}{eN_D}. \quad (4.2.8)$$

Since this factor vanishes at $j = j_d$, the leading contribution from the second factor in (4.2.5) is in zeroth order of $(j - j_d)$. Using (4.2.1) we arrive at

$$\frac{1}{j_d} \frac{\partial j}{\partial t} \approx -\frac{j - j_d}{j_d} \frac{2d}{eN_D} \frac{F^h(j_d)}{L_h \partial_j F^h(j_d)} \approx -\frac{j - j_d}{j_d} \frac{d}{L_h} \frac{1}{\tau_{\text{eff}}}, \quad (4.2.9)$$

with $\tau_{\text{eff}} \approx 1$ ps. Since $L_h/d < N$, which is the number of wells in the high field domain, we obtain typical relaxation times of less than 100 ps. During this time, the fronts typically travel less than two wells, which justifies the simplification that the current relaxation according to (4.2.9) is almost instantaneous. This means that (4.2.6) is always immediately fulfilled. By formally inverting the left hand side of (4.2.6) and taking into account the results of Sec 3.2 we arrive at the conclusion that

$$j = j_{(N_a, N_d)} = j\left(\frac{N_a}{N_d}\right), \quad (4.2.10)$$

which is a monotonically increasing function, since v_d (v_a) is monotonically increasing (decreasing). We can therefore replace the condition $|j| < |j_c|$ appearing in rule GI' on page 34 by an equivalent condition

$$\frac{N_a}{N_d} < r_c, \quad (4.2.11)$$

where the parameter r_c is defined by $j_c = j(r_c)$. A similar statement applies to rule GII'. We have therefore managed to enslave the current density j to the fraction N_a/N_d . Note that in particular $j_d = j(1)$.

4.2.2 The rules for the front model

For the analysis of the bifurcation scenario, it is sufficient to consider the dynamics in the Poincaré section which is defined by the hyperplane, where N_a or N_d change. The absolute time between such events is not important, and we are therefore free to rescale the velocities to our convenience. In the following we rescale time such that $v_a + v_d = 2$, which together with (4.2.6) gives the front velocities as

$$v_a = \frac{2N_d}{N_a + N_d}, \quad v_d = \frac{2N_a}{N_a + N_d}. \quad (4.2.12)$$

We require that the fronts evolve according to (4.2.12), until an event which changes the number of fronts occurs. Such an event may be the generation of a new front at the emitter according to the rules GI' and GII' as described in Sec. 3.3.1. Furthermore two fronts can collide as described in Sec. 3.3.2, which will simply eliminate the corresponding d_i and a_i from the system of variables and decrease N_a and N_d accordingly by one. The third possibility is the annihilation of a front at the collector as described in (Sec. 3.3.3). We may summarize the complete front model by the following set of rules:

- FI The positions of the accumulation fronts a_i for $i = 1 \dots N_a$ and depletion fronts d_i for $i = 1 \dots N_d$ evolve according to $\dot{a}_i = v_a$ and $\dot{d}_i = v_d$ with the velocities (4.2.12) until one of the following rules applies.

4 Chaotic Front Dynamics

FII If $N_a/N_d < r_c$ and $p_h < d_1 < a_1$ then increase N_a by one, re-index $a_i \rightarrow a_{i+1}$ for all i and set $a_1 = 0$ (injection of accumulation front).

FIII If $N_a/N_d > r_c$ and $p_l < a_1 < d_1$ then increase N_d by one, re-index $d_i \rightarrow d_{i+1}$ for all i and set $d_1 = 0$ (injection of depletion front).

FIV If $a_{i'} = d_{j'}$ for any i', j' then decrease N_a and N_d by one, re-index $a_{i+1} \rightarrow a_i$ for $i \geq i'$ and $d_{j+1} \rightarrow d_j$ for $j \geq j'$ (annihilation of front pair).

FV If $a_{N_a} > L$ decrease N_a by one (accumulation front hits collector).

FVI If $d_{N_d} > L$ decrease N_d by one (depletion front hits collector).

Here p_h and p_l are the phenomenological distance parameters from GI' and GII' on page 34, which suppress the front generation for $d_1 \leq p_h$ and $a_1 \leq p_l$, respectively [86].

The only parameters appearing in the front model are r_c , p_h and p_l , which govern the generation of new fronts at the emitter and L , which influences the annihilation at the collector. The voltage parameter L_h is connected to the voltage by (4.2.1), and in principle also depends weakly on N_a/N_d due to (4.2.10), but for simplicity we consider L_h to be constant. Then L_h only enters in the initial condition for the front positions (see Eq. (4.2.2)). These five parameters should be contrasted to the large set of parameters of the microscopic model (Tables 2.1 and 2.2). However, in particular p_h and p_l might be difficult to derive quantitatively from the microscopic model, and should rather be regarded as *fit parameters*. Again p_h and p_l can in principle depend on N_a and N_d , but for simplicity we assume them to be constant.

The dynamical variables of the systems are the positions d_i and a_i of the fronts. Due to the constraint given by (4.2.2), the number of degrees of freedom is then given by $f^d = N_a + N_d - 1$ and we have $f^d \leq N_a^{\max} + N_d^{\max} - 1 = 2n - 2$, which in general is much smaller than N , the number of degrees of freedom of the full microscopic model. It is however a peculiarity of this system that f^d changes dynamically. To avoid the mathematical complications that arise from the fact that the number of dynamical system variables is not constant, we formally extend the arrays of front positions to the maximal possible size, $a_1, \dots, a_{N_a^{\max}}$ and $d_1, \dots, d_{N_d^{\max}}$ and consider additionally N_a and N_d as discrete system variables. The new additional front positions $a_{N_a+1} \dots a_{N_a^{\max}}$ and $d_{N_d+1} \dots d_{N_d^{\max}}$ do not appear in the front rules FI to FVI on page 49 and we can just set them to zero for definiteness. By this formal transformation we have now obtained a system with $N_a^{\max} + N_d^{\max}$ continuous and two discrete variables¹. This type of system therefore belongs to the mathematical class of *hybrid* systems. Hybrid models are of fundamental interest in the field of theoretical computer science, where they are used to describe the interaction of a digital (i.e. discrete) computer with an analog environment [87].

¹Since the product of two countable sets is also countable, we may as well replace the two discrete variables by only one.

r_c	n	N_a^{\max}	N_d^{\max}
0	1	0	1
$(0, \frac{1}{2}]$	2	1	2
$(\frac{1}{2}, \frac{2}{3}]$	3	2	3
$(\frac{2}{3}, \frac{3}{4}]$	4	3	4
$(\frac{n-2}{n-1}, \frac{n-1}{n}]$	n	$n-1$	n
1	∞	∞	∞
$[\frac{n}{n-1}, \frac{n-1}{n-2})$	n	n	$n-1$
$[\frac{3}{2}, 2)$	3	3	2
$[2, \infty)$	2	2	1
∞	1	1	0

Table 4.1: Maximum possible number of accumulation and depletion fronts and the number of necessary tanks n (see Sec. 5.2) for various values of r_c .

Note that the rules of the front model are invariant under the simultaneous transformation of

$$\begin{aligned} a_i &\leftrightarrow d_i, & N_a &\leftrightarrow N_d, & p_h &\leftrightarrow p_l, \\ r_c &\rightarrow \frac{1}{r_c}, & L_h &\rightarrow L - L_h, \end{aligned} \quad (4.2.13)$$

i.e. accumulation and depletion fronts are exchanged, r_c is inverted, and the high field and low field domains are exchanged ($L_h \rightarrow L - L_h$). This exact symmetry can therefore explain the qualitative point symmetry found in Fig. 4.8, since the transition $r_c \rightarrow r_c^{-1}$ induces a corresponding transformation $\sigma(j(r_c)) \rightarrow f^s(\sigma(j(r_c)))$ with the fixed point $\sigma(j_d) = f^s(\sigma(j_d))$.

In view of the symmetry of (4.2.13) we may restrict our analysis to the case $r_c < 1$. We furthermore set $p_l = 0$ since the accumulation fronts are rather narrow and should not suppress the generation of a trailing depletion front. In this case rule FIII always applies, if the first front is an accumulation front, since in this case $N_a/N_d \geq 1$ and injects a new depletion front. On the other hand rule FII can only apply if $N_d = N_a + 1$. It does not apply as long as $N_a > r_c/(1 - r_c)$ and N_a can then only decrease, since FII is the only process which generates new accumulation fronts. Consequently r_c imposes the following limits on the number of fronts:

$$N_d \leq n, \quad N_a \leq n - 1, \quad (4.2.14)$$

where n is the largest integer less than $1/(1 - r_c) + 1$. The dependence of the maximum front numbers N_a^{\max} and N_d^{\max} on r_c is summarized in Table 4.1.

Once the conditions for FII are fulfilled and an accumulation front is injected, it is immediately followed by the injection of a depletion front due to rule FIII.

Effectively we therefore inject a pair of fronts, i.e. a dipole, with a leading accumulation and a trailing depletion front. In the language of field domains, this process detaches a high field domain from the emitter and opens a new one.

In Table 4.1 we also list the parameter n , which is defined as

$$n = \max [N_a^{\max}, N_d^{\max}]. \quad (4.2.15)$$

Since n is invariant under the symmetry transformation (4.2.13), we propose that n will be a suitable parameter for classifying different bifurcation behaviors. Indeed we will see in Chapter 5 that n corresponds to the number of tanks, which are necessary to describe a given dynamics.

4.2.3 The case $n = 3$

The numerical integration of the front model is facilitated by the fact that the evolution of the front positions is piecewise linear due to FI with the velocities given in (4.2.12). We can therefore calculate the times $t_{\text{FII}}, \dots, t_{\text{FVI}}$, until the corresponding conditions in FII...FIV would be fulfilled under the assumption that N_a and N_d would not change. The actual event is then determined by the minimum time t_{FX} , with $X = \text{II} \dots \text{VI}$. The fronts are then moved to the new positions $a'_i = a_i + t_{\text{FX}}v_a$ and $d'_i = d_i + t_{\text{FX}}v_d$, and the changes in the discrete variables N_a and N_d are performed as prescribed by the respective rule FX.

The numerical solution of the front model for $p_l = 0$, and $N_a^{\max} = 2$ yields a typical front pattern as in Fig. 4.9. We see that for small L_h the front which is closest to the collector, is always a depletion front. Since the fronts are generated in pairs at the emitter, we have $N_d = N_a + 1$, and therefore $v_a > v_d$. That means that the accumulation fronts can catch up and annihilate with the respectively preceding depletion fronts. This is the same behavior as observed in Sec. 4.1 for the microscopic model. In fact the front pattern at low L_h in Fig. 4.9 can be directly related to the ones in Fig. 4.1. As a particular striking example compare the period seven orbits at $L_h = 0.202$ in Fig. 4.9 and at $U = 0.98\text{V}$ in Fig. 4.1. As long as the fronts do not reach the collector, the only relevant length scale for L_h is the distance parameter p_h . In the microscopic model, this parameter corresponds to the minimal distance between the first depletion front and the newly generated accumulation front and will in general depend on the buildup time of the accumulation front and other microscopic parameters in a complicated way.

In its present form the front model is not chaotic, which is in contrast to the full microscopic model. Instead arbitrarily long stable periodic orbits are possible. We will discuss in the following Chapter 5, how chaoticity can be introduced in a generic way. At higher values of L_h , we find the characteristic ‘‘tongues’’ ($L_h = 0.595$ in Fig. 4.9), which also occur in the microscopic model (see $U = 3.55\text{V}$ in Fig. 4.5), but we did not succeed in finding the other patterns in Fig. 4.5. One reason, why the front model does not describe well the high L_h case becomes apparent, if we

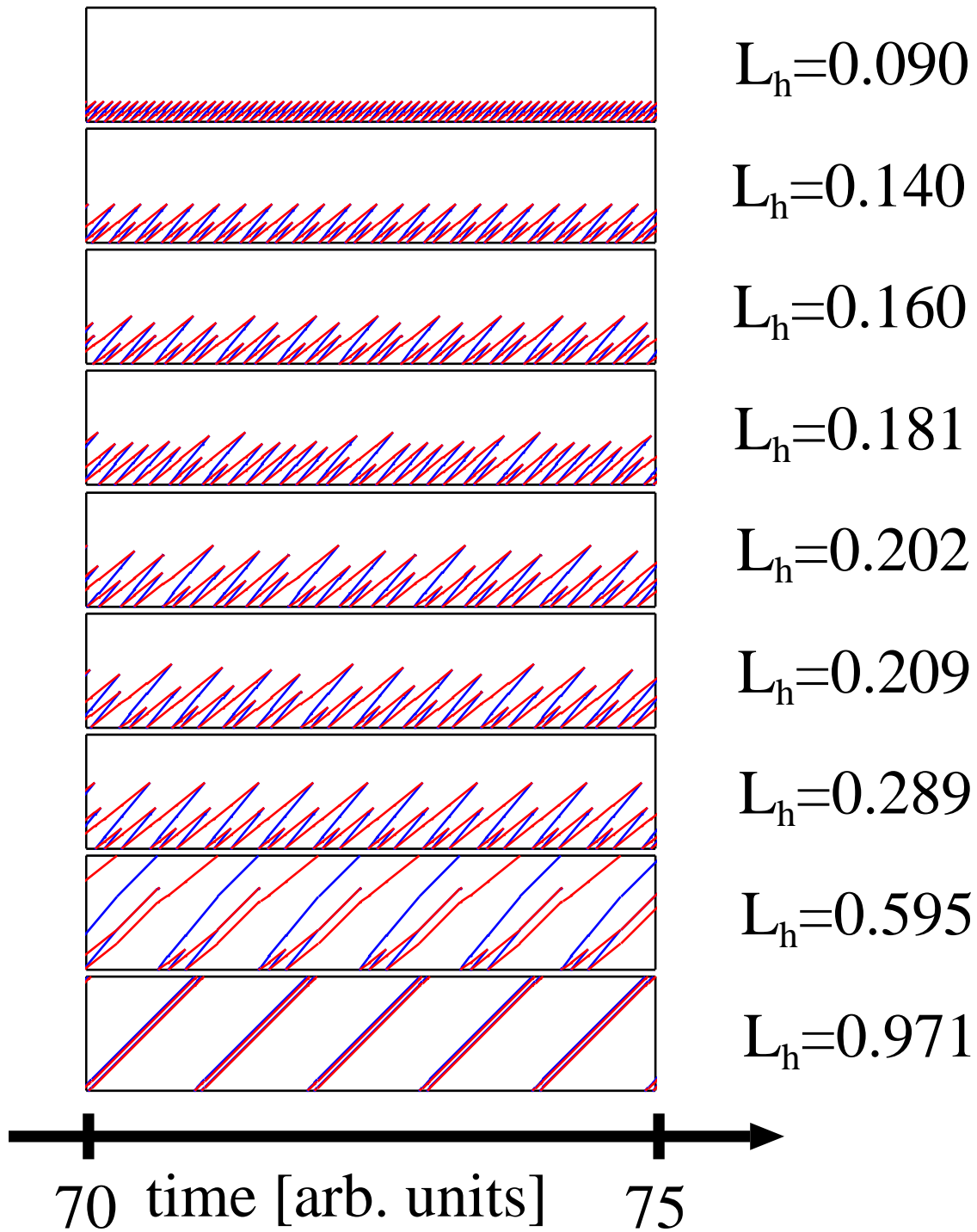


Figure 4.9: Front evolution in front model for $n = 3$, $p_l = 0$, $p_h = 0.115$, $r_c = 0.51$, $L = 1$ and various values of L_h . Accumulation (depletion) fronts are denoted by blue (red) lines. L_h corresponds to the voltage U in the microscopic model (cf. Figs. 4.1, 4.5).

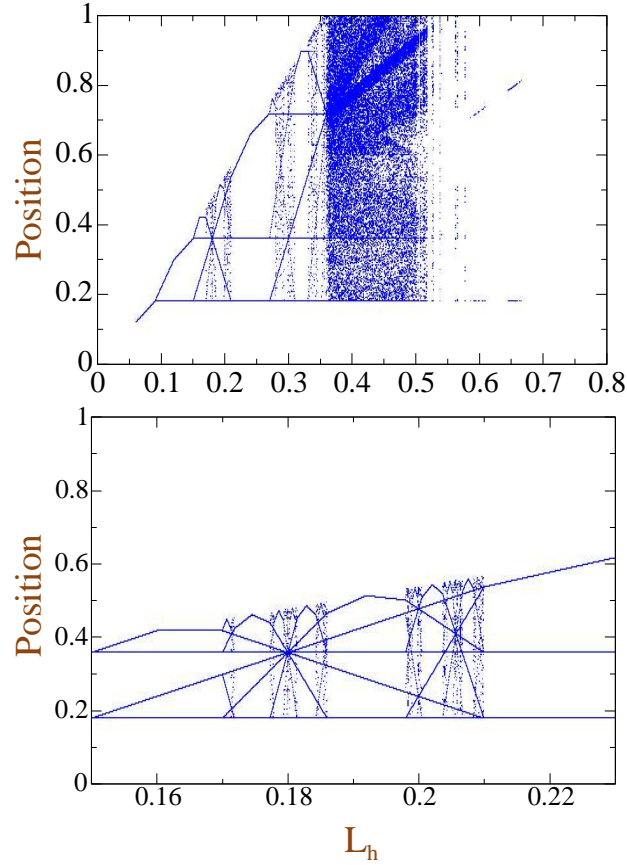


Figure 4.10: Bifurcation diagrams for positions of front collision vs L_h obtained from the front model for $n = 3$ on two different scales. Parameters: $p_h = 0.06$, $p_l = 0$, $r_c = 0.52$, $L = 1.0$.

compare $L_h = 0.971$ in Fig. 4.9 and $U = 4.5$ V in Fig. 4.5, where fronts of opposite polarity traverse the whole superlattice at only a very small distance to each other. This is obviously not possible in the microscopic approach, since the fronts would tend to annihilate. Thus the front model can still be improved in the high voltage regime.

A further touchstone for the usefulness of the front model is given by its bifurcation diagram as shown in Fig. 4.10. The prominent feature is again the cobweb-like pattern at low voltages, which has a striking similarity with the corresponding patterns in Fig. 4.4(a) and Fig. 4.6. In fact all regions from A to K of Fig. 4.6 can also be identified in Fig. 4.9, only region K does not fit perfectly. In particular, the vertical bands in Fig. 4.10(b) can be identified with the three chaotic bands in the regions D and F of Fig. 4.6. However, since the front model, is not really chaotic in this regime, they actually consist of ever finer subbands as shown in the lower panel of Fig. 4.10. Apparently a period of more than seven different collision points, appears chaotic in the microscopic model. Another feature of the original

bifurcation scenario that is well reproduced by the front model is that the chaotic behavior suddenly becomes periodic at about $L_h = 0.53$. On the other hand, we do not observe periodic windows for $L_h \in [0.36, 0.53]$ which were present in the microscopic model.

The fact that the topology of the nontrivial pattern up to the large period three window $U = 1.1V$ in Fig. 4.4 can be reproduced by the simple rules of the front model, is a hint that such a pattern might be even more generic, as we will see in Chapter 5.

We could now proceed to extract the detailed features of the bifurcation diagram by a thorough analysis of the algebraic properties of the front model. For example the horizontal lower line appearing in Fig. 4.10 is caused by p_h . If $N_a = 1$ and $N_d = 2$, we can inject a new accumulation front by FII as soon as d_1 has reached p_h . As argued before, this will entail as well the injection of a depletion front, and we have the situation:

$$N_a = 2, \quad N_d = 3, \quad a_1 = d_1 = 0 \quad d_2 = p_h \quad d_3 - a_2 = L_h - p_h. \quad (4.2.16)$$

From (4.2.12) we get $v_a - v_d = 2/5$. If now additionally $L_h > 2p_h$, it follows that $d_3 - a_2 > d_2 - a_1$ and therefore the fronts d_2 and a_1 will be the first to annihilate. If $L_h > 3/2p_h$, then the fronts d_3 and a_2 will be the first to annihilate, but by that time $d_1 > P_h$ and therefore a new dipole is immediately injected at the emitter. This maintains the velocities of the original d_2 and a_1 and in both cases the collision occurs at a position

$$p^{z1} = p_h \frac{v_a}{v_a - v_d} = np_h. \quad (4.2.17)$$

For $n = 3$ and $p_h = 0.06$ this yields the horizontal line in Fig. 4.10 at $p^{z1} = 0.18$. A further analysis of the structure of the bifurcation diagram along these lines is possible, but cumbersome. We will therefore in the next chapter introduce a model which is better suited to an analytical approach.

4.2.4 Arbitrary n

In Fig. 4.11 the bifurcation diagrams of the front model for $n = 4$ and $n = 5$ are plotted. After the successful identification of many common features in the bifurcation diagrams of the microscopic model and the front model for $n = 3$, we would hope that at least some features from Fig. 4.11 also appear in one of the panels of Fig. 4.7. However, this is apparently not the case. The reason for this failure seems to be that with a large number of fronts, the approximation that fronts can be considered as independent point-like ‘‘quasi-particles’’ breaks down. In the language of statistical physics, the dilute gas approximation is no longer valid, and we have to take into account three front interactions, and other complications. We may speculate however that for very large superlattices with narrow fronts, a bifurcation scenario as in Fig. 4.11 should arise.

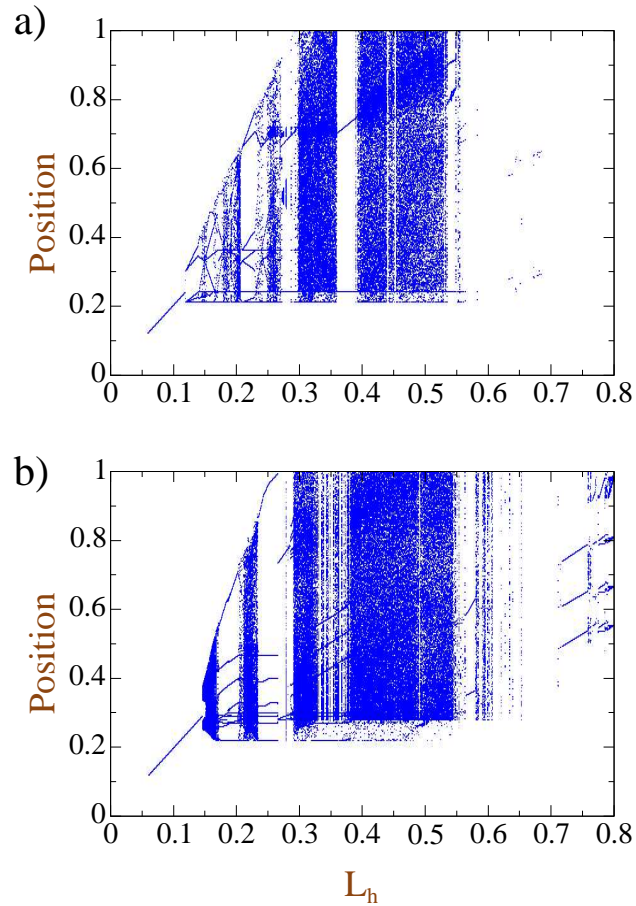


Figure 4.11: Bifurcation diagrams for positions of front collision vs L_h obtained from the front model for (a) $n = 4$ ($r_c = 0.67$) and (b) $n = 5$ ($r_c = 0.76$). Parameters: $p_h = 0.06$, $p_l = 0$, $L = 1.0$.

It is nevertheless still interesting to scan the (L_h, r_c) plane of the front model for regions of long periods, since they correspond to chaotic regimes of the microscopic model. By varying r_c and L_h simultaneously we obtain the two parameter bifurcation diagram of Fig. 4.12. Note that the broad horizontal bands in Fig. 4.12 are due to the fact that the changes in r_c within the intervals given by Table 4.1 do not affect the dynamics of the system. The basic structure of the bifurcation diagram obeys the symmetry of (4.2.13) and conforms well with the corresponding bifurcation diagram of the microscopic model in Fig. 4.8.

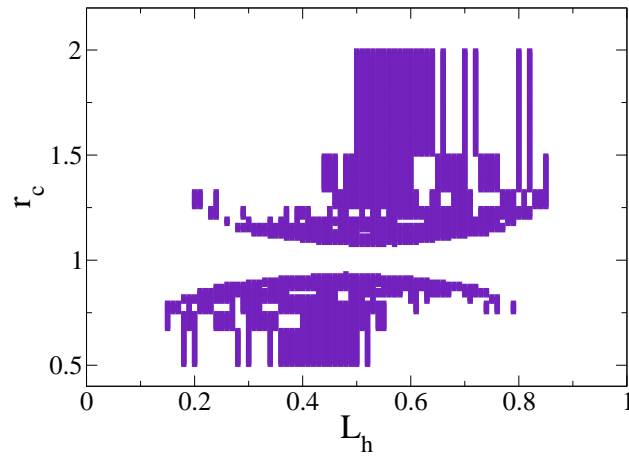


Figure 4.12: Two parameter bifurcation diagram for the front model. Dark region corresponds to (L_h, r_c) pairs with at least 10 different points of front collisions. Parameters: $L = 1.0$; for $r_c < 1$: $p_h = 0.06$, $p_l = 0$; for $r_c > 1$: $p_h = 0$, $p_l = 0.06$. In the microscopic superlattice model, L_h and r_c correspond to U and σ , respectively (cf. Fig.4.8).

5 The Tank Model

In the previous Chapter 4 we have introduced a simple front model, which astonishingly well reproduces many features of the complex microscopic model, at least in the low and intermediate voltage regimes, when no fronts reach the collector. We will now further simplify the front model in this regime and will finally arrive at a *tank model*. Such models have been extensively studied in computer science and applied mathematics, since they describe the dynamic of production processes [88, 89]. Typically one obtains a “strange billiard” behavior [90, 91], which means that the system evolves piecewise linearly, and only changes its direction at the boundary of a specific domain. The advantage of such an approach, is that these type of models can often be treated analytically. As we will see, this simplification allows us to relate the bifurcation scenario of the front system to the bifurcations obtained in a simple low dimensional iterated map system. In the most simple nontrivial case this map will be only one dimensional.

A connection between maps and single fronts has previously been studied in the case of coupled map lattices [92] and for periodically driven systems [93]. In contrast to those works, however, we are here concerned with the use of maps for a system with interacting fronts [86].

5.1 Deduction from the Front Model

Let us now derive the tank model from the front model on page 49. The idea is that instead of dealing with the position of accumulation and depletion fronts, we restrict ourselves to the dynamics of the high field domains, which appear between two fronts, or between the emitter and the first depletion front. Technically it is again easier to start with the case $p_l = 0$, but we will see that in principle, the tank model even holds for general p_l .

5.1.1 The Case $p_l = 0$

We again assume $r_c < 1$ and for the moment $p_l = 0$. Our first task is to derive a condition, for which no fronts will reach the collector. We consider a situation where $N_d = N_a + 1 \leq n$, at the point in time where a dipole is injected at the emitter by the rules FII and FIII of the front model (see page 49). We then have $a_1 = 0$, $d_1 = 0$ and $d_2 \leq L_h$ by (4.2.2). From (4.2.12) we see that $v_a - v_d > 2/(2n - 1)$ and therefore the time until a_1 and d_2 collide will be $t^{\text{collision}} < L_h(n - 1/2)$. On the other hand we

variable N_d . The global constraint (4.2.2) is translated to the new variables by

$$L_h = \sum_{i=1}^{N_d} x_i. \quad (5.1.4)$$

From the front velocities (4.2.12) we may obtain the shrinking and growing velocities of the high field domains by

$$\dot{x}_i = \begin{cases} v_d = \frac{2N_d-2}{2N_d-1} & \text{if } i = 1, \\ v_d - v_a = -\frac{2}{2N_d-1} & \text{else.} \end{cases} \quad (5.1.5)$$

$$= -\mu + \lambda\delta_{i1}, \quad (5.1.6)$$

with

$$\mu = \frac{2}{2N_d-1} \quad \lambda = N_d\mu. \quad (5.1.7)$$

The conditions for rule FII are expressed in terms of the new variables, by requiring that $N_d < n$ and $x_1 < p_h$. As usual FIII follows FII, and this combination detaches a high field domain from the emitter and creates a new one. The conditions for the collision rule FIV is rephrased by requiring that one of the x_i becomes zero.

We can then summarize this model by the following set of rules:

TI The high field lengths x_i evolve according to (5.1.5) until one of the following rules applies.

TII If $N_d < n$ and $x_1 > p_h$ then increase N_d by one, re-index $x_i \rightarrow x_{i+1}$ for all i and set $x_1 = 0$.

TIII If $x_{i'} = 0$ then decrease N_d by one, re-index $x_{i+1} \rightarrow x_i$ for all $i \geq i'$.

In the following we will refer to the rules TI–TIII together with the initial condition (5.1.4) as the *tank model*. The reason for this name will become obvious in Sec. 5.2. The tank model has n continuous dynamical variables $x_i, i = 1 \dots n$ and one discrete dynamical variable N_d . Like the front model (see page 49) it is therefore a *hybrid* model. It furthermore depends on one discrete parameter n , and the two continuous parameters p_h and L_h .

5.1.2 The Case $p_l > 0$

The above derivation of the tank model was restricted to the special case $p_l = 0$. This restriction is not necessary for the derivation of the tank model, and we now show that for general p_l the rules TI–TIII are still valid without modification, although the condition (5.1.1) and the definition of the time axis has to be adapted.

For $p_l > 0$ the front model rule FIII does not follow immediately FII, but the injection of the depletion front is delayed, until $a_1 > p_l$ is fulfilled. During this time

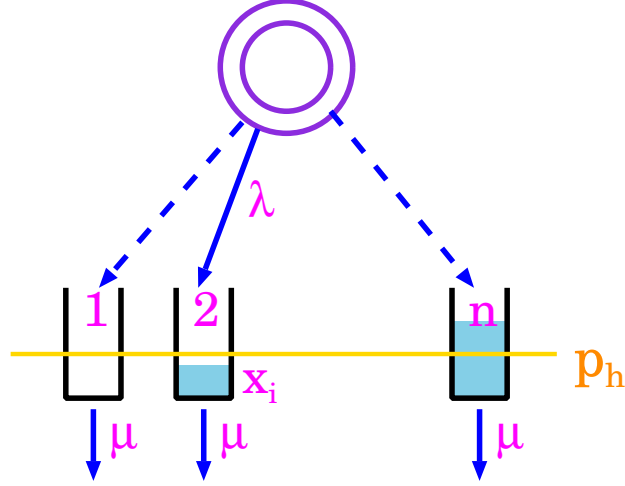


Figure 5.2: Scheme of an n -tank switched arrival system with minimal filling height p_h . The server filling rate is λ , the draining rate of all tanks is $-\mu$.

we have $N_a = N_d$ and hence $v_a = v_d = 1$, which means that no collisions occur, and all front positions are just increased by p_l . Equivalently, instead of adding the constant p_l to every front position, one can also reduce the effective lattice length L by the amount p_l each time a new accumulation front is injected. During the transit of an accumulation front to the emitter, this may happen at most $L/(p_h + p_l) + 1$ times, since two accumulation fronts are at least separated by a distance $p_l + p_h$. Therefore the condition (5.1.1) that no fronts reach the collector has to be modified for the case $p_l \neq 0$ to read

$$L_h \left(n - \frac{1}{2} \right) < \frac{3}{4} \left(L \frac{p_h}{p_l + p_h} - p_l \right). \quad (5.1.8)$$

Furthermore during the time between FII and FIII, all high field fronts are bounded by an accumulation and a depletion front and $\dot{x}_i = 0$ for all i . The net effect of a non vanishing p_l is then to increase the time variable by the amount p_l , each time a high field front is disconnected from the emitter, but otherwise follow the rules TI–TIII. This effect will obviously not influence the dynamic bifurcation scenario, and can be eliminated completely by a suitable redefinition of the time axis.

5.2 Connection to Water Tanks

Let us now justify the use of the term *tank model* for the model described by the rules TI–TIII, by showing that surprisingly the same set of rules describes a completely different system. Consider a system of n water tanks as in Fig. 5.2. Here a switching server fills one of the tanks with a filling rate λ , and at the same

time all N_d nonempty tanks drain at a rate $-\mu$. To keep the total amount of water at a constant value L_h , we require $\lambda = \mu N_d$. The server switches to one of the $n - N_d$ empty tanks only under the condition that the tank which it is currently filling has already reached the minimum filling height p_h . This model is equivalent to what we formulated by the rules TI-TIII and the initial condition (5.1.4). The variables x_i of the high field domains are up to some trivial re-indexing the filling heights of the water tanks. The high field domain x_1 at the emitter is interpreted as the tank connected to the server, while the other nonempty tanks represent detached high field domains inside the superlattice. A switching of the server corresponds to the detaching of the old high field domain at the emitter, and the generation of a new one by TII. The rule that the server should not switch if the currently filled tank has a filling height less than p_h , obviously agrees with the requirement of TII that a high field domain may only be detached from the emitter, if it has a certain minimal length p_h . The constant amount of water corresponds to the constant total length of the high field regime L_h .

Variants of such models are well studied in the context of production processes [89]. For example in [91] a model with a *maximum* filling height was considered. In computer science similar models are relevant for the description of *queuing systems* [94], where the server can for example represent a CPU, and the tanks are the different tasks, which should be served by the CPU. Even the requirement of a minimal filling height makes sense in this context, since in a multitasking computer system, the switching of the task involves a certain overhead, which forbids arbitrarily fast task switching.

5.3 The Poincaré Map

A natural way to proceed is to consider a suitable Poincaré section. Since all tanks with the exception of tank #1, which is connected to the server, are equivalent, we now adopt the sorting convention that $x_i > x_{i+1}$ for $i \geq 2$. Thus the dynamics of the system is confined to an $n - 1$ dimensional simplex of the form

$$A^n = \{\mathbf{x} \in \mathbb{R}^n \mid \sum_{j=1}^{n-1} x_j = L_h \wedge x_1 \geq 0 \wedge x_2 \geq \dots \geq x_n \geq 0\}. \quad (5.3.1)$$

As a suitable hyperplane for the Poincaré section we consider the $n - 2$ dimensional simplex

$$B^n = \{\mathbf{x} \in A^n \mid x_1 \geq p_h \wedge x_n = 0\}, \quad (5.3.2)$$

which precisely contains the set of points, for which the conditions of rule TII are fulfilled. A sketch of A^n and B^n for the case $n = 3$ is shown in Fig. 5.3.

Let us assume that at a certain time t_m we have $\mathbf{x}(t_m) \in B^n$. We now look for a Poincaré map

$$P^n : B^n \rightarrow B^n, \quad \mathbf{x}(t_m) \mapsto \mathbf{x}(t_{m+1}), \quad (5.3.3)$$

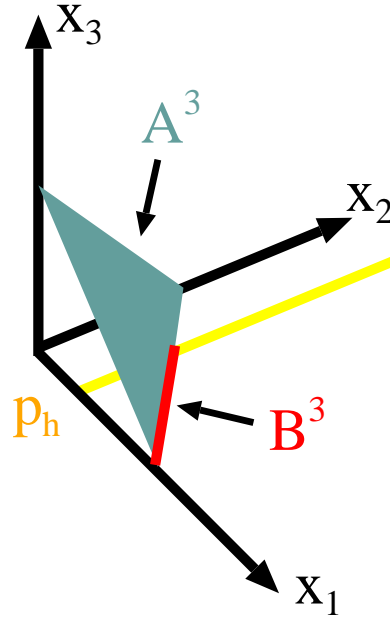


Figure 5.3: Sketch of the simplex A^3 (5.3.1) and the Poincaré section B^3 (5.3.2) for $n = 3$.

which relates $\mathbf{x}(t_m)$ to the point $\mathbf{x}(t_{m+1})$ of the next visit of the simplex B^n . For $n = 2$ the simplex B^2 is reduced to a point $B^2 = \{(L_h, 0)\}$, which by P^2 is simply mapped onto itself. The dynamics is therefore trivially periodic. In the following we assume $n \geq 3$.

The application of rule TII at t_m triggers the generation of a new high field domain at the emitter, or in the language of water tanks, the switching of the server to a new tank. This is achieved by a relabeling of the tank indices such that old x_1 is enqueued among the $x_2 \dots x_{n-1}$ and the new x_1 is set to zero. Explicitly we write

$$\mathbf{x}(t_m^+) = M^{\text{TII}} \mathbf{x}(t_m), \quad (5.3.4)$$

where t_m^+ denotes the time just after the application of TII. The matrix M^{TII} takes care of the ordering of the filling heights and is given by

$$M^{\text{TII}} = \begin{cases} \delta_{j_0, j} & \text{for } j = 1, \\ \delta_{i, j} & \text{for } 2 \leq j < j_0, \\ \delta_{i+1, j} & \text{for } j \geq j_0, \end{cases} \quad (5.3.5)$$

$$\text{with } x_{j_0-1}(t_m) \geq x_1(t_m) \geq x_{j_0}(t_m). \quad (5.3.6)$$

In particular we note that

$$x_1(t_m^+) = 0, \quad (5.3.7)$$

$$x_n(t_m^+) = \min(x_{n-1}(t_m), x_1(t_m)), \quad (5.3.8)$$

and therefore $\mathbf{x}(t_m^+) \notin B^n$. This guarantees that $t_{m+1} > t_m$.

We first consider the case with $(n-1)x_n(t_m^+) > p_h$, which by (5.3.8) is equivalent to

$$(n-1)x_{n-1}(t_m) > p_h. \quad (5.3.9)$$

Then the tank #1 receives water from the $n-1$ other tanks, and will have reached the filling height p_h before tank # n is empty. Therefore the time t_{m+1} , at which $\mathbf{x}(t)$ visits B^n is given by

$$t_{m+1} = t_m + \frac{x_n(t_m^+)}{\mu}. \quad (5.3.10)$$

For $t \in [t_m^+, t_{m+1}^-]$ there are no empty tanks, i.e. $N_d(t) = n$, and we may write explicitly

$$x_i(t_{m+1}) = \begin{cases} (n-1)x_n(t_m^+) & \text{for } i = 1, \\ x_i(t_m^+) - x_n(t_m^+) & \text{for } i = 2 \dots n-1, \\ 0 & \text{for } i = n. \end{cases} \quad (5.3.11)$$

In the case that (5.3.9) is not fulfilled, the last tank is empty before the first tank has reached its minimal switching height p_h . The switching time t_{m+1} is therefore determined by the condition $x_1(t_{m+1}) = p_h$. For the construction of the Poincaré map, we need to know the number of nonempty tanks \tilde{N}_d at the time t_{m+1}^- just before we visit B^n . A little thought shows that this is given by

$$\tilde{N}_d = N_d(t_{m+1}^-) = \max \left\{ k \in \mathbb{N} \left| \sum_{i=k+1}^n x_i(t_m^+) + (k-1)x_k(t_m^+) > p_h \right. \right\} \quad (5.3.12)$$

$$= \max \left\{ k \in \mathbb{N} \left| \sum_{i=k}^{n-1} x_i(t_m) + (k-1)x_{k-1}(t_m) > p_h \right. \right\}. \quad (5.3.13)$$

Using the definition

$$\Delta x_e = \frac{p_h - \sum_{j=\tilde{N}_d}^{n-1} x_j(t_m)}{\tilde{N}_d - 1}, \quad (5.3.14)$$

we find

$$t_{m+1} = t_m + \frac{\Delta x_e}{\mu}, \quad (5.3.15)$$

and finally

$$x_i(t_{m+1}) = \begin{cases} p_h & \text{for } i = 1, \\ x_i(t_m^+) - \Delta x_e & \text{for } i = 2 \dots \tilde{N}_d, \\ 0 & \text{for } i > \tilde{N}_d. \end{cases} \quad (5.3.16)$$

Collecting the pieces together, (5.3.11), (5.3.16) and (5.3.4) define the Poincaré map P^n of (5.3.3) for general n . In the following we will explicitly examine the cases P^3 and P^4 .

In the limiting case of $p_h = 0$ no tank has to wait for filling. We obtain a switched arrival system [88] and the Poincaré map can be written explicitly as

$$\mathbf{x}(t_{m+1}) = M^{\text{III}}\mathbf{x}(t_m) + \min[x_1(t_m), x_{n-1}(t_m)] \begin{pmatrix} n-1 \\ -1 \\ \vdots \\ -1 \end{pmatrix}. \quad (5.3.17)$$

As shown in [90] this system is chaotic for all $n > 2$ and has a constant invariant probability measure.

5.4 Bifurcation Analysis for $n = 3$

In the case $n = 3$, the Poincaré section B^3 in (5.3.2) is one-dimensional, and we have for $\mathbf{x} \in B^3$ the conditions $x_3 = 0$, $x_1 \in [p_h, L_h]$ and $x_2 = L_h - x_1$ (cf. Fig. 5.3). Thus we may parametrize B^3 by the coordinate x_1 , and the Poincaré map is fully determined by a one-dimensional map

$$P^3 : [p_h, L_h] \rightarrow [p_h, L_h], \quad x_1(t_m) \mapsto x_1(t_{m+1}), \quad (5.4.1)$$

which we will now determine explicitly.

Following (5.3.4) we find

$$x_1(t_m^+) = 0 \quad (5.4.2)$$

$$x_2(t_m^+) = \max[x_1(t_m), x_2(t_m)] = \max[x_1(t_m), L_h - x_1(t_m)] \quad (5.4.3)$$

$$x_3(t_m^+) = \min[x_1(t_m), L_h - x_1(t_m)] \quad (5.4.4)$$

and condition (5.3.9) can be written as

$$2(L_h - x_1(t_m)) > p_h. \quad (5.4.5)$$

In the case that (5.4.5) is fulfilled we have from (5.3.11)

$$x_1(t_{m+1}) = 2 \min[x_1(t_m), L_h - x_1(t_m)], \quad (5.4.6)$$

and otherwise $x_1(t_{m+1}) = p_h$.

Thus we may summarize the resulting Poincaré map in the case $n = 3$ by

$$P^3 : [p_h, L_h] \rightarrow [p_h, L_h] \quad (5.4.7)$$

$$P^3(x_1) = \begin{cases} 2x_1 & \text{for } x_1 \in [p_h, \frac{1}{2}L_h) \\ 2L_h - 2x_1 & \text{for } x_1 \in [\frac{1}{2}L_h, L_h - \frac{1}{2}p_h) \\ p_h & \text{for } x_1 \in [L_h - \frac{1}{2}p_h, L_h] \end{cases} \quad (5.4.8)$$

$$= \max\{(L_h - |L_h - 2x_1|), p_h\}. \quad (5.4.9)$$

The graph of this map is schematically drawn in Fig. 5.4(a) and for various values of L_h in Fig. 5.4(b).

The dynamics of the iterated map (5.4.8) depends on the two positive¹ parameters

¹Similar maps with negative p_h have been considered in [95].

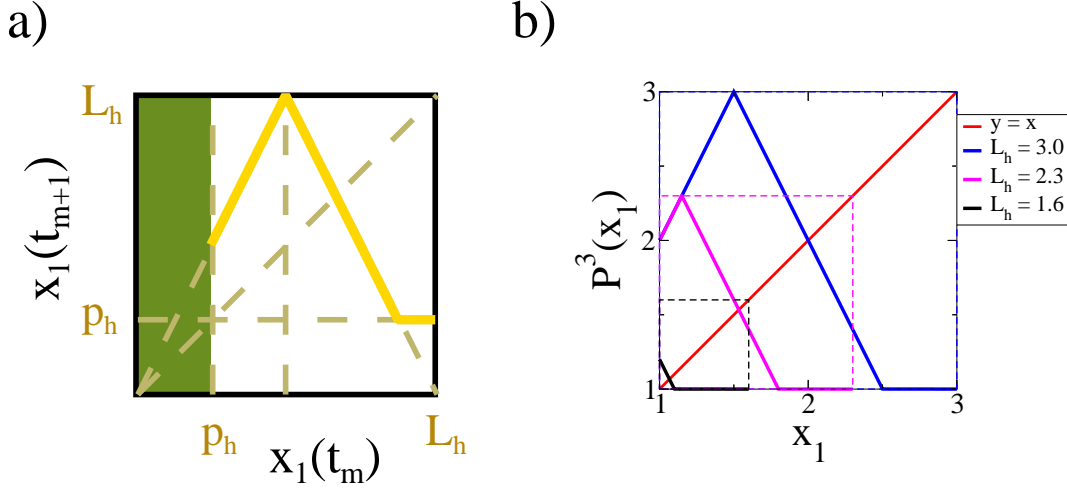


Figure 5.4: (a) Schematic graph of the one-dimensional Poincaré map P^3 for the $n = 3$ tank model according to Eq. (5.4.8). In the shaded region the map is not defined. (b) Graph of P^3 for $p_h = 1$ and various values of L_h .

p_h and L_h . The numerically calculated bifurcation diagram of $P^3(x_1)$ for fixed p_h and increasing L_h is shown in Fig. 5.5. We see that we recover a bifurcation structure which is very similar to the front model at low L_h (cf. Fig. 4.10). At any point with the same L_h/p_h both bifurcation diagrams show the same periodicity. This is not surprising, since the only necessary condition in the derivation of the tank model was that no fronts should reach the collector [see (5.1.1)]. The nature of the bifurcations was not affected. However, the meaning of the variables has changed. While in Fig. 4.10 the positions of the collisions is plotted, Fig. 5.5 shows the size of the high field domain, when it is detached from the emitter. The information about the position of the collisions was lost in the derivation of the tank model, when the number of system variables was reduced from $2n - 1$ to n .

5.4.1 Connection with the Flat-Topped map

One-dimensional iterated maps are usually defined on the unit interval $[0, 1]$. This requirement may be met by an expansion of the domain of P^3 to $[0, L_h]$ followed by a rescaling off all lengths in units of L_h :

$$P^3(x_1) = L_h \hat{P}_z^3 \left(\frac{x_1}{L_h} \right), \quad (5.4.10)$$

$$\hat{P}_z^3(x) = \begin{cases} 2x & \text{for } x \in [0, \frac{1}{2}), \\ 2 - 2x & \text{for } x \in [\frac{1}{2}, 1 - \frac{1}{2}z), \\ z & \text{for } x \in [1 - \frac{1}{2}z, 1]. \end{cases} \quad (5.4.11)$$

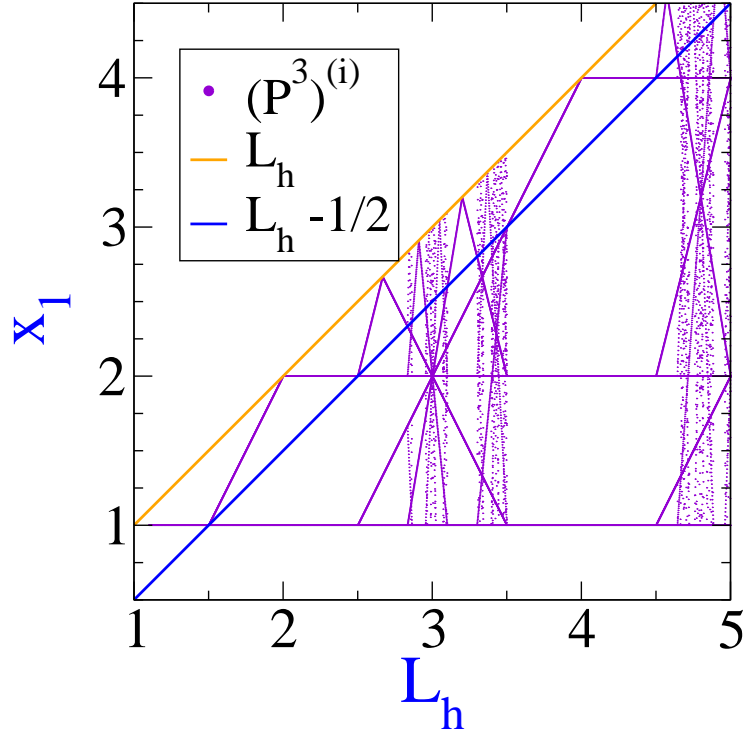


Figure 5.5: Bifurcation diagram of the Poincaré map P^3 according to (5.4.8) for fixed $p_h = 1$ and varying L_h . Starting from a random $x_1^0 \in [p_h, L_h]$ we calculate at each L_h the i th iteration $x_1^i = P^3(x_1^{i-1})$. The plotted points are $x_1^{200} \dots x_1^{300}$. The blue and orange lines denote the left and right boundaries of the flat region of P^3 , respectively.

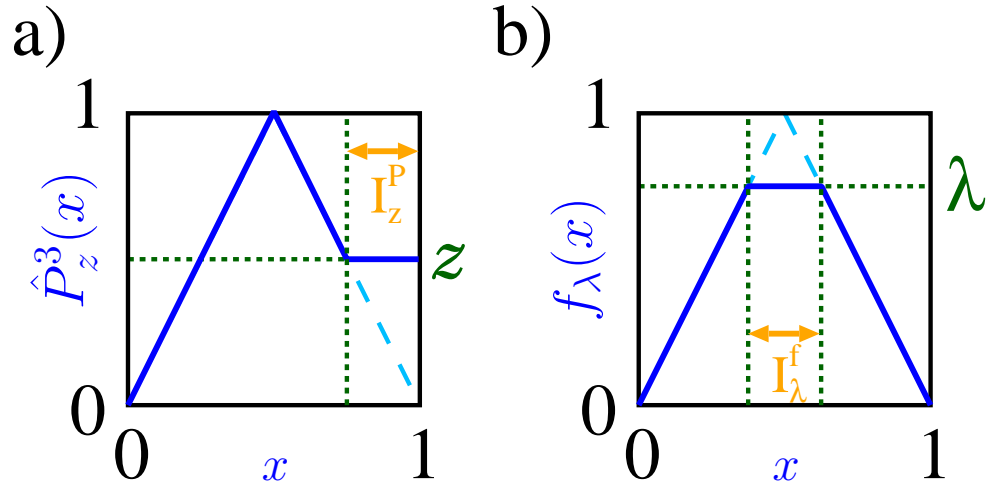


Figure 5.6: Graphs of (a) \hat{P}_z^3 according to Eq. (5.4.11) and (b) $f_\lambda(x)$ according to Eq. (5.4.12).

The flat segment of the map $\hat{P}_z^3(x)$ is located at the right edge of its domain in the interval $I_z^P = [1 - z/2, 1]$ [cf. Fig. 5.6(a)]. In the mathematical and physical literature, however, a slightly different class of *flat-topped* or *trapezoidal* maps of the form [see Fig. 5.6(b)]

$$f_\lambda(x) = \min[1 - |2x - 1|, \lambda] \quad \text{for } \lambda \in [0, 1] \quad (5.4.12)$$

has been studied extensively [96, 97, 98]. The bifurcation diagram for this map is shown in Fig. 5.7(a). Here the flat segment is at the maximum of the map in the interval

$$I_\lambda^f = [\lambda/2, 1 - \lambda/2] = \left[\frac{1}{2} - \frac{1 - \lambda}{2}, \frac{1}{2} + \frac{1 - \lambda}{2} \right]. \quad (5.4.13)$$

The boundaries of I_λ^f are indicated by colored lines in Fig. 5.7(a).

We observe that by choosing

$$\lambda = 1 - \frac{z}{2} = 1 - \frac{p_h}{2L_h} \quad (5.4.14)$$

the flat segment of f_h is exactly the preimage of the flat segment of \hat{P}_z^3 , i.e.

$$I_\lambda^f = \left(\hat{P}_z^3 \right)^{-1} (I_z^P). \quad (5.4.15)$$

Consider now the two trajectories x^1, x^2, x^3, \dots and y^1, y^2, y^3, \dots of some initial point $x^0 = y^0 \notin I_z^P$, with $x^i = \hat{P}_z^3(x^{i-1})$ and $y^i = f_\lambda(y^{i-1})$. Let m be the first index, such that $x^m \in I_z^P$. From (5.4.15) we conclude that the first index n for which $x^n \in I_\lambda^f$, is given by $n = m - 1$. Therefore the two trajectories y^i and x^i are identical for $i < m$. Since $y^{m-1} \in I_\lambda^f$ we have $y^m = \lambda$ and, using (5.4.14) we find $y^{m+1} = 2 - 2\lambda = z = x^{m+1}$. This means that the trajectories x^1, x^2, x^3, \dots and y^1, y^2, y^3, \dots only differ at indices m with $x^m \in I_z^P$, where we have $y^m = \lambda$. Apart from this difference, all other properties of the two trajectories such as periodicity or stability are identical. Hence we may restrict ourselves to the consideration of the *unimodal* map f_λ , which completely reproduces the bifurcation scenario of P^3 .

This equivalence can also be seen directly from the bifurcation diagram of P^3 in Fig. 5.5. For any L_h there is only one point in the interval between the blue and the orange line. If we map this point to the blue line, we obtain exactly the appropriately scaled bifurcation diagram of f_λ in Fig. 5.7(b).

5.4.2 The Tent-Map Case $\lambda = 1$

For $\lambda = 1$ [i.e. $L_h \rightarrow \infty$ according to Eq. (5.4.14)], the function $f_1(x)$ in Eq. (5.4.11) reduces to the well known *tent-map*

$$f_1(x) = 1 - |2x - 1|. \quad (5.4.16)$$

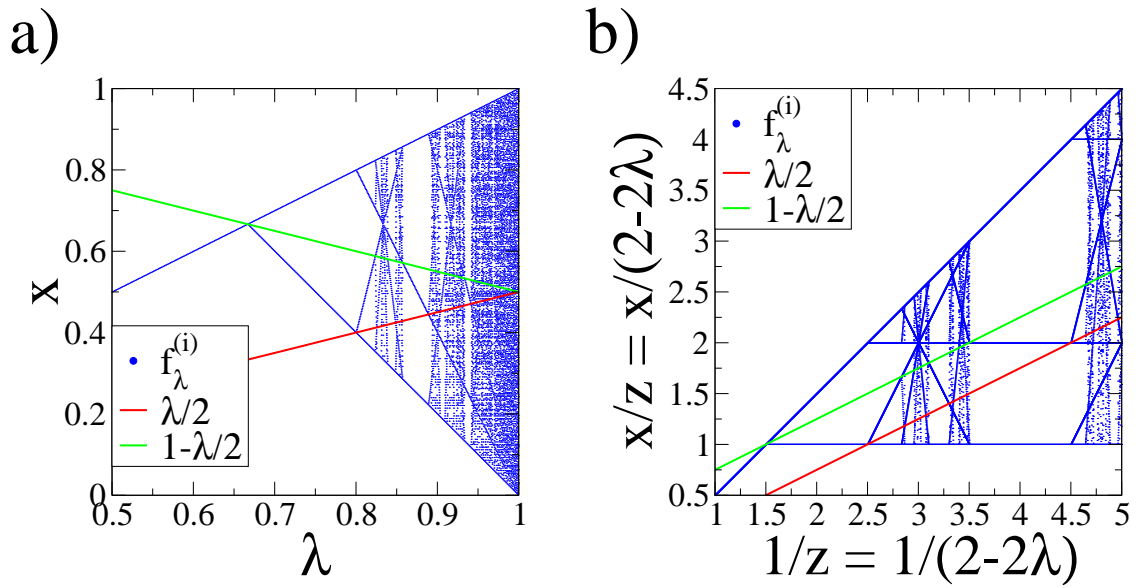


Figure 5.7: Bifurcation diagrams of the flat topped map $f_\lambda(x)$ [cf. Eq. (5.4.12) and Fig. 5.6(b)]. The red and green lines show the left and right boundaries of I_λ^f (5.4.13). Note that the left and right panels only differ in the axes scaling.

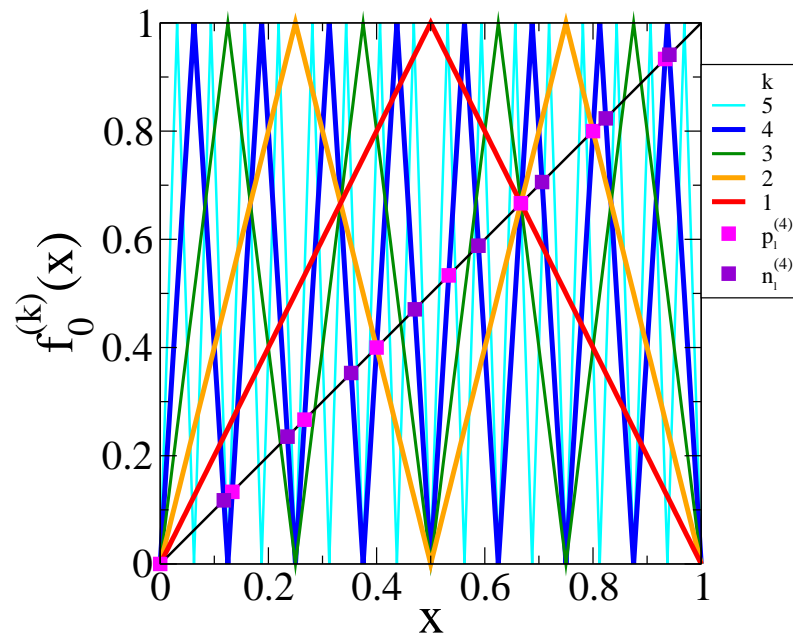


Figure 5.8: Iterations of the tent-map $f_0^{(k)}$ for various k according to Eq. (5.4.17), and fixed points $p_l^{(k)}$ and $n_l^{(k)}$ according to Eq. (5.4.18).

The tent-map is an archetype of a chaotic map [99] that can be treated analytically. The results for this special case turn out to be useful in the discussion of the more complicated case $\lambda < 1$ (see Sec. 5.4.3).

The k th iterate of f_1 , which we denote by $f_1^{(k)}$ has 2^k branches and is given by

$$f_1^{(k)}(x) = 1 - 2^k \left| x - \frac{2l+1}{2^k} \right| \quad \text{for } x \in \left[\frac{l}{2^{k-1}}, \frac{l+1}{2^{k-1}} \right], \quad l = 0 \dots 2^{k-1} - 1. \quad (5.4.17)$$

The fixed points of $f_1^{(k)}$, which are the points of period k , are explicitly given by

$$\begin{aligned} p_l^{(k)} &= \frac{2l}{2^k - 1} \\ n_l^{(k)} &= \frac{2l + 2}{2^k + 1} \end{aligned} \quad \text{for } l = 0 \dots 2^{k-1} - 1. \quad (5.4.18)$$

The slopes of $f_1^{(k)}(x)$ at the fixed points are given by $\partial_x f_1^{(k)}(p^{(k)}) = 2^k$ and $\partial_x f_1^{(k)}(n^{(k)}) = -2^k$. Thus all fixed points are unstable, which means that the tent map f_1 has no stable periodic orbits. The dynamics is chaotic [100] and has a constant invariant measure². Furthermore it follows that

$$f_1^{(k)}(x) > x \quad \text{for } x \in [p_l^{(k)}, n_l^{(k)}], \quad l = 0 \dots 2^{k-1} - 1. \quad (5.4.19)$$

In Fig. 5.8 the iterates $f_1^{(k)}$, and the fixed points $p_l^{(4)}$ and $n_l^{(4)}$ for $k = 4$ are depicted.

It is worthwhile to note that the fixed points $x_l^{(k)}$ follow a remarkable pattern, when written in binary notation. The variable l in (5.4.18) can be written as a binary number $l = \%Q$, where Q is a string consisting of $k - 1$ letters of 0 or 1 (we fill up with leading 0s as necessary) and the $\%$ indicates a binary number. We denote by \tilde{Q} the bitwise inverse of Q (i.e. $\% \tilde{Q} = 2^k - \%Q$). A few lines of algebra show that the fixed points in (5.4.18) are given in the binary number base by

$$\begin{aligned} p_l^{(k)} &= p_Q^k = \%0.Q0Q0Q0Q0Q\dots \\ n_l^{(k)} &= n_Q^k = \%0.Q1\tilde{Q}0Q1\tilde{Q}0Q\dots \end{aligned} \quad \text{for } l = \%Q = 0 \dots 2^{k-1} - 1. \quad (5.4.20)$$

The appearance of the patterns in (5.4.20) is also directly explained by considering the tent map (5.4.16) in binary notation [99],

$$f_1(\%0.X) = \begin{cases} \%0.Y & \text{for } X = 0Y \\ \%0.\tilde{Y} & \text{for } X = 1Y. \end{cases} \quad (5.4.21)$$

For $f_1^{(k)}$ we then find

$$f_1^{(k)}(\%0.X) = \begin{cases} \%0.Y & \text{for } X = Q0Y \\ \%0.\tilde{Y} & \text{for } X = Q1Y. \end{cases} \quad \text{for } \%Q = 0 \dots 2^{k-1} - 1 \quad (5.4.22)$$

²Formally, there are infinitely many fixed points of the Perron Frobenius operator for f_1 , but only the constant measure is natural, in the sense that it is stable against fluctuations (see Exercise 7.5 in [99]).

and requiring $X = Y$ or $X = \tilde{Y}$ yields directly the patterns for p_Q^k or n_Q^k of Eq. (5.4.18), respectively.

5.4.3 The Case $\lambda < 1$

In order to finally explain the bifurcation scenarios in Fig. 5.5, we now want to characterize the stable periodic trajectories of f_λ . In the following we will discuss the trajectory of $x_\lambda^0 = 1/2$ given by

$$x_\lambda^1, x_\lambda^2, x_\lambda^3, \dots \quad \text{with } x_\lambda^k = f_\lambda(x_\lambda^{k-1}) \text{ and } x_\lambda^1 = f_\lambda\left(\frac{1}{2}\right). \quad (5.4.23)$$

From (5.4.13) we see that $x_\lambda^0 = 1/2 \in I_\lambda^f$ and thus $x_\lambda^1 = \lambda$. Let $k = k(\lambda)$ be the first index with $x_\lambda^k \in I_\lambda^f$ and let us assume that³ $k < \infty$. Then $x_\lambda^{k+1} = \lambda$ and the trajectory (5.4.23) has period $k(\lambda)$. Since $\partial_x f(x^k) = 0$ we find

$$\frac{\partial f_\lambda^{(k)}(x_\lambda^i)}{\partial x} = \prod_{j=i}^{i+k-1} \frac{\partial f_\lambda(x_\lambda^j)}{\partial x} = 0, \quad \text{for } i \leq k \quad (5.4.24)$$

and the trajectory $x_\lambda^1, \dots, x_\lambda^k$ is a stable period $k(\lambda)$ orbit.

We now want to determine the function $k(\lambda)$. This can in principle be done, by considering the iterates $f_\lambda^{(j)}$, but this approach is analytically quite involved. Instead, we make use of the known iterates $f_1^{(j)}$ of the tent map [see Eq. (5.4.17)]. Since f_λ differs from the tent map f_1 only in the interval I_λ^f , and $x_\lambda^i \notin I_\lambda^f$ for $1 < i < k$, we may write

$$x_\lambda^i = f_1^{(i-1)}(\lambda), \quad \text{for } 1 < i \leq k. \quad (5.4.25)$$

The condition $x_\lambda^k \in I_\lambda^f$ for a stable period k orbit, can then be rephrased in term of the tent map as $f_1(x_\lambda^k) \geq f_\lambda(x_\lambda^k) = \lambda$. Formally we may thus express $k(\lambda)$ as

$$k(\lambda) = \min \left\{ i \in \mathbb{N} \mid f_1^{(i)}(\lambda) \geq \lambda \right\}. \quad (5.4.26)$$

This formula allows for a simple ‘‘graphical’’ interpretation with the help of Fig. 5.8. To find $k(\lambda)$, choose the point (λ, λ) on the diagonal, and find the smallest k , such that $f_1^{(k)}$ is above the diagonal. In this way, we may for instance find $k(\lambda) = 4$ for $\lambda \in [p_6^{(4)}, n_6^{(4)}]$. In the following we will show that all intervals with fixed k are of this form.

Let us now consider the trajectories of x_λ^i under variation of λ . Applying the chain rule to (5.4.25) yields

$$\frac{\partial x_\lambda^i}{\partial \lambda} = (-1)^{N_R(i)} 2^{[(i-1) \bmod k]}, \quad (5.4.27)$$

$$\text{where } N_R(i) = \left| \left\{ j \mid x_\lambda^j > \frac{1}{2} \wedge 1 \leq j \leq [(i-1) \bmod k] \right\} \right|, \quad (5.4.28)$$

³It was shown in [96] that the set $\{\lambda \mid k(\lambda) \rightarrow \infty\}$ has Lebesgue measure zero.

and $|\cdot|$ denotes the cardinal number. Here N_R counts the number of minus signs that are picked up by visiting the negative slope region of f_1 . The bifurcation parameter λ only enters implicitly in the right hand side of Eq. (5.4.27) via $k(\lambda)$. Let us for example consider a λ range, for which a minimal k_0 exists, such that $k_0 \leq k(\lambda)$. Then we have $x_\lambda^i \notin I_\lambda^f$ for $i < k_0$, and $N_R(i)$ in (5.4.28) will be constant across the considered λ range. Thus x_λ^i for $i \leq k_0$ will depend linearly on λ by Eq. (5.4.27). This naturally explains the appearance of the straight lines in Fig. 5.7(a) even across complicated bifurcations. These straight lines are preserved under the axis transformation leading to Fig. 5.7(b). We can now also explain the appearance of the cobweb structures, for instance at $\lambda_c = 5/6$ [cf. $1/z = 3$ in Fig. 5.7(b)]. This yields a trajectory with $x_\lambda^i = 2/3$ for $i \geq 2$. Thus $k(\lambda_c)$ formally diverges, and we can find intervals around λ_c with arbitrary high k_0 . Therefore the points x_λ^k for $2 \geq k \leq k_0$ will converge in straight lines to $x_\lambda^k \rightarrow 2/3$ for $\lambda \rightarrow \lambda_c$. This explains the typical cobweb structure, where bundles of straight lines appear to converge in a single point.

Due to (5.4.27), the point $x_\lambda^k \in I_\lambda^f$ has the largest absolute slope with respect to λ of all points in the trajectory $x_\lambda^0, \dots, x_\lambda^k$. Bifurcations, i.e. a change in $k(\lambda)$, will only appear, if either with increasing λ the point x_λ^k leaves I_λ^f , or another point x_λ^i with $i < k$ enters I_λ^f . This latter case is not independent from the first one, since for any λ , there cannot exist simultaneously two distinct points x_λ^i, x_λ^k in I_λ^f . Since x_λ^k moves continuously, it must leave I_λ^f as x_λ^i enters it. With the help of (5.4.26) and (5.4.19) we infer that the bifurcation points are fixed points of $f_1^{(k)}$, and that the intervals with constant $k(\lambda)$ are of the form [see (5.4.20)]

$$I_Q^k = [p_Q^k, n_Q^k], \quad (5.4.29)$$

with a *suitable* binary string Q of length $k - 1$. Suitable in this context means that

$$f_1^{(i)}(\lambda) \leq \lambda \quad \text{for all } \lambda \in I_Q^k \text{ and } i < k. \quad (5.4.30)$$

The question is now, how to construct those suitable Q . The following construction is essentially analogous to the classical construction of the universal U-sequences [101] and will finally result in Table 5.1, where all Q s up to period 7 are listed. Here we have the advantage that in our case all intervals can be calculated explicitly, and we can avoid symbolic dynamics in the derivation, but in hindsight we see that symbolic arguments yield essentially the same results. We stress that the U-sequence is different from the well known Sarkovskii ordering [102, 100], since the latter is only a statement about the existence of periods, and not about their stability. The U-sequence however predicts the exact sequence of all stable periods, as one bifurcation parameter is changed.

#	k	Q	p_Q^k	n_Q^k	itinerary
1	1	empty	0	$0.\overline{10}$	empty
2	2	1	$0.\overline{10}$	$0.\overline{1100}$	R
3	4	110	$0.\overline{1100}$	$0.\overline{11010010}$	RLR
4	8	1101001	$0.\overline{11010010}$	$0.\overline{1101001100101100}$	RLR^3LR
5	6	11010	$0.\overline{110100}$	$0.\overline{110101001010}$	RLR^3
6	7	110101	$0.\overline{1101010}$	$0.\overline{11010110010100}$	RLR^4
7	5	1101	$0.\overline{11010}$	$0.\overline{1101100100}$	RLR^2
8	7	110110	$0.\overline{110110}$	$0.\overline{110111001000}$	RLR^2LR
9	3	11	$0.\overline{110}$	$0.\overline{111000}$	RL
10	6	11100	$0.\overline{111000}$	$0.\overline{111001000110}$	RL^2RL
11	7	111001	$0.\overline{1110010}$	$0.\overline{11100110001100}$	RL^2RLR
12	5	1110	$0.\overline{11100}$	$0.\overline{1110100010}$	RL^2R
13	7	111010	$0.\overline{1110100}$	$0.\overline{11101010001010}$	RL^2R^3
14	6	11101	$0.\overline{111010}$	$0.\overline{111011000100}$	RL^2R^2
15	7	111011	$0.\overline{1110110}$	$0.\overline{11101110001000}$	RL^2R^2L
16	4	111	$0.\overline{1110}$	$0.\overline{11110000}$	RL^2
17	7	111100	$0.\overline{1111000}$	$0.\overline{11110010000110}$	RL^3RL
18	6	11110	$0.\overline{111100}$	$0.\overline{111101000010}$	RL^3R
19	7	111101	$0.\overline{1111010}$	$0.\overline{11110110000100}$	RL^3R^2
20	5	1111	$0.\overline{11110}$	$0.\overline{1111100000}$	RL^3
21	7	111110	$0.\overline{1111100}$	$0.\overline{11111010000010}$	RL^4R
22	6	11111	$0.\overline{111110}$	$0.\overline{111111000000}$	RL^4
23	7	111111	$0.\overline{1111110}$	$0.\overline{1111110000000}$	RL^5

Table 5.1: Intervals with constant period up to period 7 (with the exception of the period 8 pattern in line 4).

5.4.4 Elementary Intervals

The most elementary strings Q , which fulfill the condition (5.4.30) are simply of the form

$$Q^k = \underbrace{1 \dots 1}_{k-1} = 1^{k-1}, \quad (5.4.31)$$

where we have used a convenient exponential notation a^b , i.e. a b -fold repetition of the letter a . Then we have from (5.4.29),

$$I_{Q^k}^k = [\%0.1^{k-1}01^{k-1}0 \dots, \%0.1^k0^k1^k0^k \dots], \quad (5.4.32)$$

which means that any $\lambda \in I_{Q^k}^k$ is of the form $\lambda = \%0.1^{k-1}X$, with $\%0.\tilde{X} \leq \lambda$. Consequently, by

$$f_1^{(i)}(\lambda) = 0.0^{k-i-1}\tilde{X} \leq \lambda \quad \text{for } 1 \leq i < k, \quad (5.4.33)$$

condition (5.4.30) is fulfilled. On the other hand $f_1^k(\lambda) \geq \lambda$ by construction [cf. (5.4.19)] and thus for $\lambda \in I_{Q^k}^k$, we have indeed a stable period k orbit. This construction yields the lines #1, 2, 9, 16, 20, 22, 23 of Table 5.1.

5.4.5 Period Doubling Cascade

The next basic bifurcation scenario is the period doubling of any given suitable pattern Q_1 . Assume that Q_1 fulfills (5.4.30) and consider the interval $I_{Q_2}^{2k}$ with Q_2 being the harmonic extension of Q_1 defined by

$$Q_2 = H(Q_1) = Q_1 1 \tilde{Q}_1 \quad (5.4.34)$$

Then the boundaries of $I_{Q_2}^{2k}$ are of the form

$$p_{Q_2}^{2k} = \%0.Q_2 0 Q_2 0 Q_2 0 \dots = \%0.Q_1 1 \tilde{Q}_1 0 Q_1 1 \tilde{Q}_1 0 Q_1 1 \tilde{Q}_1 0 = n_{Q_1}^k, \quad (5.4.35)$$

$$n_{Q_2}^{2k} = \%0.Q_2 1 \tilde{Q}_2 0 Q_2 1 \tilde{Q}_2 0 \dots = \%0.Q_1 1 \tilde{Q}_1 1 \tilde{Q}_1 0 Q_1 0 Q_1 1 \tilde{Q}_1 1 \tilde{Q}_1 0 Q_1 0 \dots \quad (5.4.36)$$

The interval $I_{Q_2}^{2k}$ therefore connects consecutively to $I_{Q_1}^k$ from the right, with only the boundary point in common.

We now want to show that $I_{Q_2}^{2k}$ fulfills the condition (5.4.30). Assume that Q_2 would not fulfill (5.4.30), i.e. we can find a $\lambda \in I_{Q_2}^{2k}$ and $i < 2k$, such that $f_1^{(i)}(\lambda_i) > \lambda_i$. Since $f_1^{(i)}(n_{Q_1}^k) \leq n_{Q_1}^k$ we find by continuity $\lambda_0 \in I_{Q_1}^k$ with $f_1^{(i)}(\lambda_f) = \lambda_f$. This λ_f is then also a fixed point of $f_1^{(2i)}, f_1^{(3i)}, \dots$. In particular, we may choose $j = mi$, such that $k \leq j < 2k$, and will find a

$$\lambda_j \in I_{Q_1}^k \quad \text{with } f_1^{(j)}(\lambda_j) > \lambda_j \text{ and } k \leq j < 2k. \quad (5.4.37)$$

Since

$$f_1^{(k)}(p_{Q_2}^{2k}) = n_{Q_1}^k \in I_{Q_1}^k \quad (5.4.38)$$

$$f_1^{(k)}(n_{Q_2}^{2k}) = \%0.Q_1 0 Q_1 1 \tilde{Q}_1 \dots \in I_{Q_1}^k \quad (5.4.39)$$

we have

$$f_1^{(k)}(I_{Q_2}^{2k}) \subset I_{Q_1}^k, \quad (5.4.40)$$

and in particular $f^{(k)}(\lambda_j) \in I_{Q_1}^k$. By (5.4.37) we infer that $f^{(j-k)}(f^{(k)}(\lambda_j)) > n_{Q_1}^k$, but this is not possible, since it would contradict the assumption that Q_1 fulfills the condition (5.4.30). Thus Q_2 must also fulfill the condition (5.4.30), and $I_{Q_2}^{2k}$ is a suitable interval. This argument can be repeated for $Q_3 = H(Q_2)$, etc. leading to a classical period doubling cascade.

We can now apply the period doubling construction to all patterns Q^k found in Sec. 5.4.4. This yields the lines #2, 3, 4, 10 of Table 5.1.

The first period doubling starting with the empty string $Q^1 = Q_1$ was also studied by different methods in Ref. [98]. It was found that the Feigenbaum parameter δ ,

which is the ratio of two subsequent intervals in the period doubling cascade is not constant but scales as

$$\delta(k) = 2^k. \quad (5.4.41)$$

Since k itself obviously doubles at every period doubling, this yields an exponentially fast convergence of the sequence of bifurcation points.

5.4.6 Intermediate Intervals

We now want to recursively construct the remaining Q s of Table 5.1. Assume that we are given an ordered list of all intervals $I_{Q_i}^{k_i}$ up to a certain period k_{\max} and let Q_A and Q_B be two strings characterizing two neighboring intervals $I_{Q_A}^{k_A}$ and $I_{Q_B}^{k_B}$ with $n_{Q_A}^{k_A} < p_{Q_B}^{k_B}$ (which implies that $Q_B \neq H(Q_A)$). Let us then consider the following common substring Q , given by

$$n_{Q_A}^{k_A} = \%0.Q0X_A, \quad (5.4.42)$$

$$p_{Q_B}^{k_B} = \%0.Q1X_B. \quad (5.4.43)$$

We then see immediately that $p_Q^k < p_{Q_B}^{k_B}$ and $n_Q^k > n_{Q_A}^{k_A}$. Thus the interval I_Q^k is between the intervals $I_{Q_A}^{k_A}$ and $I_{Q_B}^{k_B}$, but since we assumed that we had started with a complete list up to period k_{\max} , it follows that $k > k_{\max}$, and Q is a suitable string in the sense of (5.4.30). Applying this construction repeatedly to all pairs of neighboring intervals, we can construct new lists with larger and larger k_{\max} . This finally yields all remaining lines in Table 5.1. With this construction we have thus explicitly calculated the bifurcation points of the map f_λ , and at the same time solved the original bifurcation problem of P^3 . We know now the exact sequence of periodic orbits as λ , or in the case of P^3 , the parameter L_h increases. Up to about period seven this sequence can be readily confirmed by the microscopic model (cf. Fig. 4.6).

5.4.7 Symbolic Dynamics

At this point we seize the opportunity and make contact to the subject of *symbolic dynamics*, which since the classical work of Metropolis, Stein and Stein [101] has developed into a powerful tool in the study of universal features in nonlinear systems [99, 96, 103, 104].

Let us consider the trajectory x_λ^i of the tent map and write a string, $M_\lambda = X_1X_2X_3\dots$ with letters

$$X_i = \begin{cases} L & \text{for } x^i < 1/2, \\ R & \text{for } x^i \geq 1/2. \end{cases} \quad (5.4.44)$$

Instead of dealing with the explicit binary representation of λ , one can now use the itinerary M_λ instead, since it can be shown that there exists a one to one

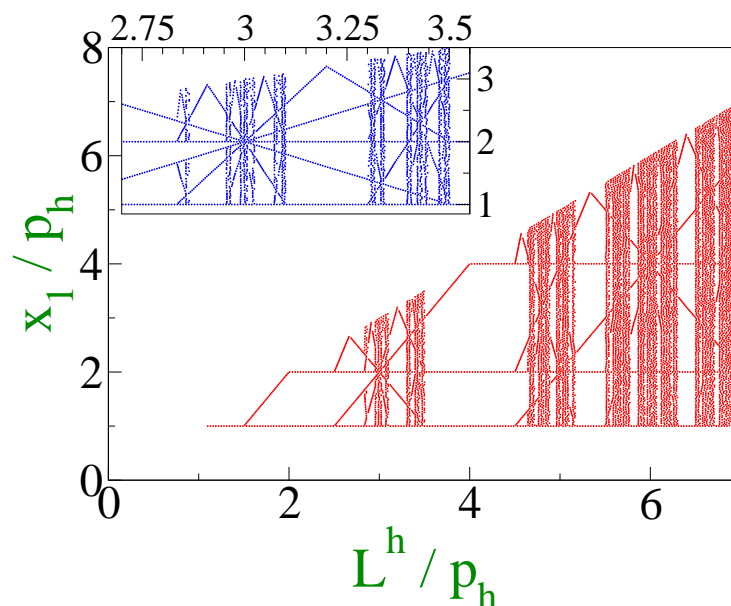


Figure 5.9: Bifurcation diagram as in Fig. 5.5, but for the map (5.4.8) with a flat region modified by a finite slope $m = 0.001$ (cf. Fig.5.6).

correspondence between the two representations [99]. The advantage of the itinerary approach is that it is applicable to a large class of one dimensional maps, although the construction of Table 5.1 is less explicit and intuitive [101]. Comparing the itineraries in Table 5.1 with the Table in the appendix of Ref. [101], however shows that both approaches are indeed equivalent.

5.4.8 Chaoticity

The maps P^3 and f_λ we have considered in the previous sections show rich bifurcation scenarios, with infinitely long periods, which we can now explain sufficiently well by means of the U-sequences. Nevertheless they are not truly chaotic. The reason is obviously the flat segment, which will eventually be visited by the trajectory, and will render any orbit stable. Such flat segments are however not physical, since they would correspond to an exact projection of a continuous set of phase points onto one single phase point. Since in the derivation of the tank model, a number of approximations were made, it is more likely that the flat segment is not exactly flat, but has at least a tiny slope $0 < m \ll 1$. Since this finite slope however increases in the iterated map as $2^k m$ it will destabilize periodic orbits of period $k(\lambda) > \log(1/m)$ and result in chaotic behavior. As shown in Fig. 5.9, this leads to continuous bands similar to the ones observed in the microscopic model (cf. Fig. 4.6) .

5.5 Bifurcation Analysis for $n = 4$

In the case $n = 4$, the Poincaré simplex B^4 in (5.3.2) is two-dimensional, and may be conveniently parametrized by x_1 and x_3 as follows:

$$B^4 = \{ \mathbf{x} \in \mathbb{R}^4 | x_1 \in [p_h, L_h] \wedge x_3 \in [0, (L_h - x_1)/2] \wedge x_2 = L_h - x_3 - x_1 \wedge x_4 = 0 \}. \quad (5.5.1)$$

The corresponding region in the (x_1, x_3) plane is shown in Fig. 5.10(a). We may now construct the associated two-dimensional Poincaré map,

$$P^4 : \begin{pmatrix} B^4 \\ x_1(t_m) \\ x_3(t_m) \end{pmatrix} \begin{matrix} \rightarrow \\ \mapsto \end{matrix} \begin{pmatrix} B^4 \\ x_1(t_{m+1}) \\ x_3(t_{m+1}) \end{pmatrix}. \quad (5.5.2)$$

We first note that according to Eq. (5.3.13) the domain B assumes the following partition with respect to \tilde{N}_d ,

$$\tilde{N}_d = 4 \Leftrightarrow x_3(t_m) > \frac{p_h}{3} \quad (5.5.3)$$

$$\tilde{N}_d = 3 \Leftrightarrow x_3(t_m) > 2L_h - 2x_1(t_m) - p_h \quad (5.5.4)$$

$$\tilde{N}_d = 2 \quad \text{else,} \quad (5.5.5)$$

which is indicated by the color scheme in Fig. 5.10(a). For $\tilde{N}_d = 4$ we have

$$x_1(t_{m+1}) = 3 \min [x_1(t_m), x_3(t_m)] \quad (5.5.6)$$

$$x_3(t_{m+1}) = |\min [x_1(t_m), L_h - x_1(t_m) - x_3(t_m)] - x_3(t_m)|. \quad (5.5.7)$$

The resulting three branches are marked by three different red colors in Fig. 5.10(a). The ranges of these three branches partly overlap, as is indicated by the striped regions in Fig. 5.10(b). In particular points with $x_1 \in (3p_h, L_h)$ have in general three preimages, one from each branch. In the case of $\tilde{N}_d = 3$, we find for P^4 :

$$x_1(t_{m+1}) = p_h \quad (5.5.8)$$

$$x_3(t_{m+1}) = \min [x_1(t_m), L_h - x_1(t_m) - x_3(t_m)] - \frac{p_h - x_3(t_m)}{2}. \quad (5.5.9)$$

These two branches correspond to the two green colored regions in Fig. 5.10(a), which are mapped to the green lines in Fig. 5.10(b). Finally for $\tilde{N}_d = 2$ the Poincaré map P^4 reduces to

$$x_1(t_{m+1}) = p_h \quad (5.5.10)$$

$$x_3(t_{m+1}) = 0. \quad (5.5.11)$$

This corresponds to the yellow region in Fig. 5.10(a), which is mapped to the yellow dot in in Fig. 5.10(b). The Jacobian of (5.5.10) vanishes, and therefore any periodic trajectory visiting the $\tilde{N}_d = 2$ region will be stable.

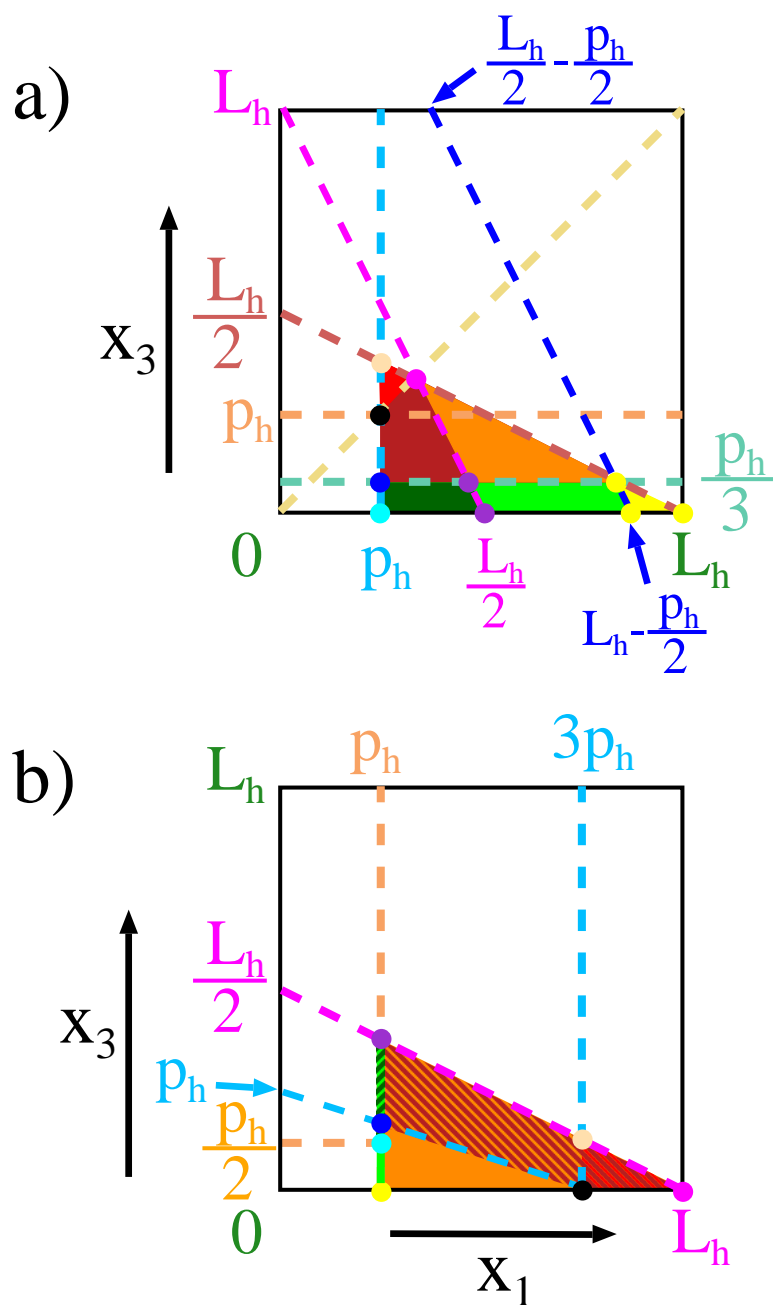


Figure 5.10: Graphical representation of the Poincaré map P^4 . (a) The colored areas define the domain B^4 of the Poincaré map P^4 (5.5.2) in the (x_1, x_3) parametrization. The reddish areas indicate the domain of $\tilde{N}_d = 4$, greenish colors indicate $\tilde{N}_d = 3$ and the yellow color the $\tilde{N}_d = 2$ regions (cf. Eq. (5.3.13)). (b) range of the colored regions from (a) under P^4 . The colors in (b) correspond to the color of the preimages in (a). The striped areas and striped lines, indicate regions with more than one preimage. The yellow region in (a) is mapped to the yellow dot in (b) at $(p_h, 0)$.

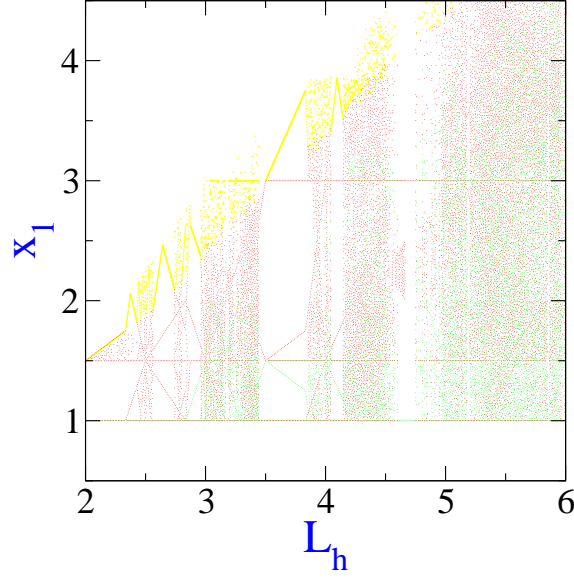


Figure 5.11: Bifurcation diagram of x_1 versus L_h for the Poincaré map P^4 given by (5.5.12). Red, green, and yellow dots fall into regions with $\tilde{N}_d = 4, 3,$ and $2,$ respectively (cf. Fig. 5.10).

Combining the three Eqs. (5.5.6) (5.5.8) (5.5.10) we can express the Poincaré map explicitly by

$$P^4 : B^4 \rightarrow B^4, \quad \mathbf{x}(t_m) \mapsto \mathbf{x}(t_{m+1}) \quad (5.5.12)$$

$$x_1(t_{m+1}) = \max \{3 \min [x_1(t_m), x_3(t_m)], p_h\} \quad (5.5.13)$$

$$x_3(t_{m+1}) = \max \left\{ 0, \quad x_3(t_m) - x_1(t_m), \quad (5.5.14)$$

$$\min [x_1(t_m), L_h - x_1(t_m) - x_3(t_m)] - \max \left[x_3(t_m), \frac{p_h - x_3(t_m)}{2} \right] \right\}.$$

P^4 is obviously continuous, since max and min are continuous.

The bifurcation diagram for P^4 is shown in Fig. 5.11. Note that the bifurcation scenario is now remarkably different from the $n = 3$ case (Fig. 5.5) but instead resembles the corresponding diagram of the front model for $n = 4$ [see Fig. 4.11(a)]. In particular the cobweb structure is now less pronounced, than in the $n = 3$ case, and the large period three window is missing. The general theory for two dimensional iterated maps of the type P^4 is considerably more involved than for the one dimensional case. A systematic approach in the language of *border collisions* was proposed in [105, 106] (for a practical application see also [107]). Since we did not see a clear evidence for $n = 4$ behavior from the microscopic superlattice model, we are not pursuing this path further, although this bifurcation scenario is of fundamental interest for the tank model.

6 Nonstationary External Voltage

So far we have only considered configurations with a fixed external voltage U . However recent experimental [108, 109, 47, 110, 50] and theoretical [68, 111, 112, 49] results show that qualitatively new features occur under nonstationary external voltage conditions.

In this chapter we will first consider switching processes, where the external voltage is increased instantaneously at a certain time $t = 0$, and then proceed to consider ramping processes, where the external voltage is continuously increased over one or more discontinuities of the current voltage characteristic. Parts of those theoretical considerations have been published in Refs. [68, 111] and were later confirmed experimentally with astonishingly high accuracy by Rogozia *et al.* [110].

At the end of this chapter we will also briefly examine the behavior of a superlattice under an external voltage, which is the sum of an ac and dc voltage. Such a configuration has been experimentally considered in the case of driven chaos [80] and high frequency oscillations in a resonator [50], but here we are mainly interested in theoretical predictions for the frequency dependent impedance of the superlattice device.

For easier comparison with existing work, we now use a superlattice of type A (cf. Table 2.2 on page 12), with $N = 40$ wells and a cross section of $A = 14400 \mu\text{m}^2$, at a temperature of $T = 5 \text{ K}$. These parameters are in accordance with the experimental superlattice used in the switching and sweeping experiments in Refs. [109, 47, 110] and were also used as the starting point for the theoretical consideration in [68, 111, 112]. We use again simple Ohmic boundary currents at the emitter and the collector (cf. Sec. 2.3). Reasonable agreement with the overall shape of the experimental current–voltage characteristic is obtained by choosing the contact conductivity $\sigma = 0.01 (\Omega\text{m})^{-1}$.

From the homogeneous current density characteristic in Fig. 6.1(a) we note that the critical current density j_c is larger than the maximum current density j_{max}^s for which stationary accumulation fronts occur (cf. velocity current characteristic in Fig. 6.1(b)). Then according to (3.3.5) the low field domain at the emitter is stable, and the complete current-voltage characteristic exhibits the typical sawtooth pattern of Fig. 6.2 [55, 56, 113, 114]. The upper and lower branches in Fig. 6.2 correspond to the up- and down-sweep of the external voltage, respectively. Each upper branch can be continuously extended to a lower branch, by slowly decreasing the voltage (violet lines in Fig. 6.2). Then each branch corresponds to a configuration with a stationary electron accumulation front located at one particular well. At the discontinuity points of a branch, the accumulation front moves to a different

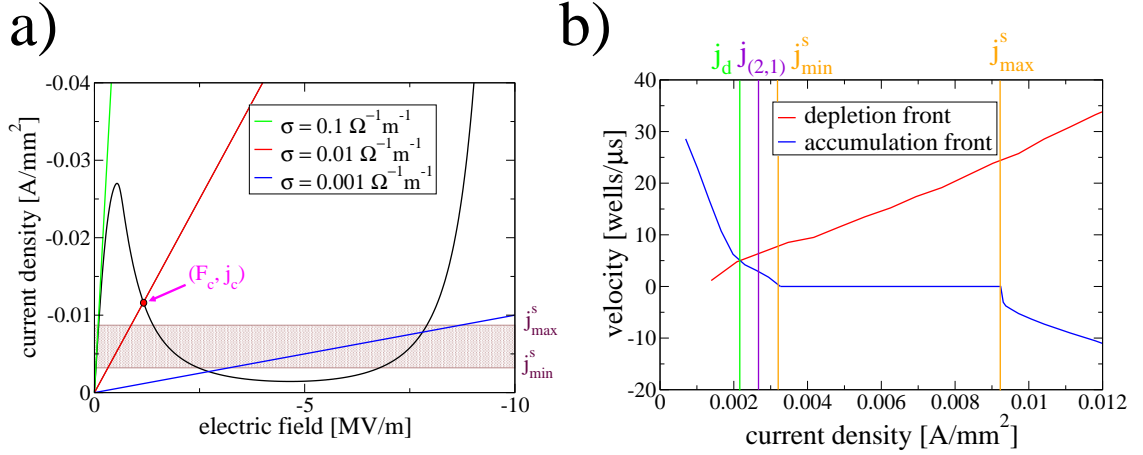


Figure 6.1: (a) Current density vs electric field characteristic between neutral wells (black) and at the emitter, with various conductivities σ for superlattice A (Table 2.2). (F_c, j_c) denotes the intersection point of the two characteristics. The shaded area between the current values j_{\min}^s and j_{\max}^s marks the regime of stationary accumulation fronts. (b) Corresponding velocity current characteristic.

well, and thus the operating point jumps onto a new branch. For one value of the external voltage, we find in general multiple stable solutions which are associated with different branches and different currents. For the parameters of superlattice A, we observe threefold (cf. $U = 1.5 \text{ V}$) and fourfold (cf. $U = 1.8 \text{ V}$) multistability.

6.1 Switching

Let us first consider the situation, where the time-dependent external voltage is given by a step function of the form

$$U(t) = \begin{cases} U_i & \text{for } t < 0, \\ U_f = U_i + U_{\text{step}} & \text{for } t \geq 0, \end{cases} \quad (6.1.1)$$

with the step size U_{step} and the initial and final voltage U_i and U_f , respectively. We will use the terms *up jump* and *down jump* for the cases $U_{\text{step}} > 0$ and $U_{\text{step}} < 0$, respectively.

We start from an operating point at $t < 0$, which is on the upper branch for the fixed initial voltage $U_i = 1.5 \text{ V}$, and apply voltage steps at $t = 0$ of various sizes. The initial and final operating points on the current voltage characteristic are denoted by arrows in Fig. 6.2.

The most simple scenario occurs if U_{step} is small enough, such that the initial branch is still present at the final voltage $U_f = U_i + U_{\text{step}}$, as for $U_{\text{step}} = -0.2 \text{ V}$

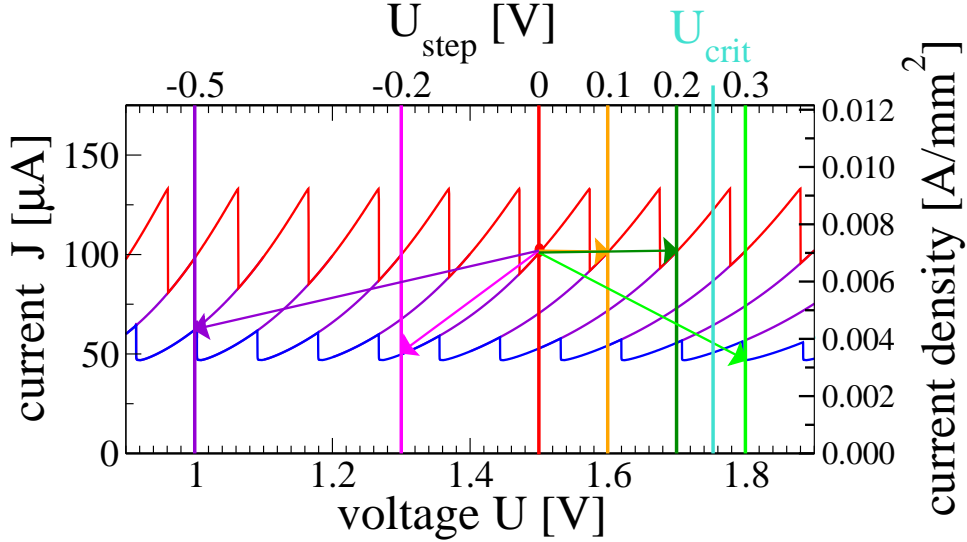


Figure 6.2: Up sweep (red) and down sweep (blue) current-voltage characteristic for a stationary superlattice of type *A* (parameters as in Table 2.2), $\sigma = 0.01(\Omega m)^{-1}$. The intermediate branches (violet) are obtained by sweeping along each individual branch. The arrows denote the starting and end points of various switching scenarios. For $U_{\text{step}} > U_{\text{crit}}$ final operating points are on the down-sweep branch.

in Fig. 6.2. Then the system prefers to remain on the initial branch (unless we are very close to a discontinuity point, as we will see later). Since the maximum of the electron distribution remains at the same well, no major charge redistributions are involved and only the position of the center of charge p_a (see (3.1.7)) is shifted to account for the changed voltage. Thus the current response in Fig. 6.3 shows an almost instantaneous relaxation to the final current value, which is in agreement with the experimental data of [110] as shown by the current trace A in Fig. 6.4(a).

6.1.1 Down Jumps

If the initial branch does not exist at the final voltage, the system is forced on a new branch. However, due to the multistability of the system, it is not a priori clear, which branch will be chosen. For a down jump with $U_{\text{step}} < 0$ we observe the lower branch at the final voltage is always preferred, independently of the size of U_{step} . Consider for instance the case $U_i = 1.5 \text{ V}$ and $U_{\text{step}} = -0.5 \text{ V}$. From Fig. 6.2 we see that we will finally end up on the lowest stable branch for $U_f = 1.0 \text{ V}$. The current response for this case (violet line in Fig. 6.3) shows a sharp drop at the switching time $t = 0$, which is due to the instantaneous decrease of all electric fields by U_{step}/L . The current density then drops below j_{min}^s , and the accumulation front will move in positive direction, towards the collector, as shown in the electron density plot in Fig. 6.5. As the accumulation front moves to the collector, the high field domain

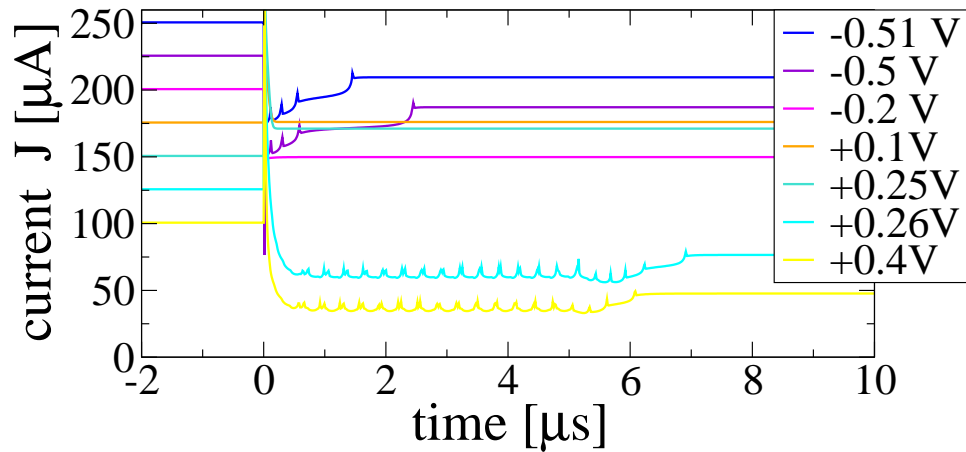


Figure 6.3: Current response versus time for $U_i = 1.5$ V and various U_{step} . Parameters as in Fig.6.2. The individual current traces are spread by $25 \mu\text{A}$ for clarity.

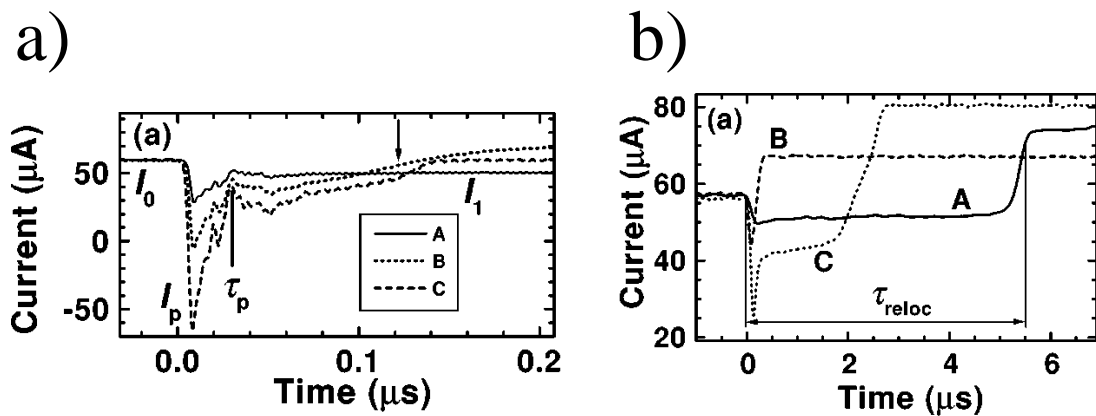


Figure 6.4: (a) Experimental time traces for down jumps from the third branch to the third (A), second (B) and first branch (C), respectively. (b) Experimental time traces for down jumps from the fourth branch to the third branch (A and B) and second branch (C), respectively. The final voltage for trace A is closer to the discontinuity with the fourth branch than for current trace B. Note that the time scales of (a) and (b) are different. Reprinted from [110].

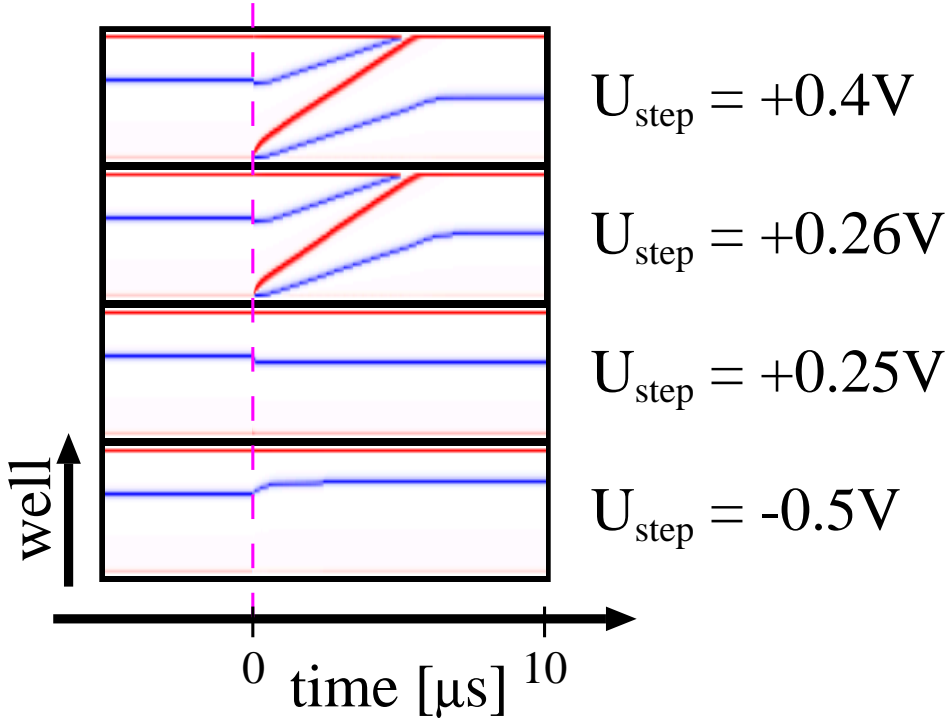


Figure 6.5: Space time plot of the electron density evolution of the switching processes indicated in Fig.6.3, with $U_i = 1.5 \text{ V}$ and various U_{step} . Regions of electron accumulation (depletion) are shaded in blue (red).

decreases, and thus the fields in the low and high field domain, will increase again. This leads to an increase in the current, which is however intermitted by small spikes, due to the motion of the maximum of the electron density to a new well. Thus for $U_{\text{step}} < 0$ we have always a direct motion of the accumulation front to its new position, irrespective of the size of U_{step} . This finding is corroborated by recent experiments [110] (cf. Fig. 6.4(b)).

A further remarkable feature in the case $U_{\text{step}} = -0.5 \text{ V}$ is the plateau in the current trace (Fig. 6.3) from $t = 0.7 \dots 2.2 \mu\text{s}$, just before the last spike brings us to the final current value. This is caused by the vicinity of V_f to the discontinuity of the down-sweep characteristic (Fig. 6.2). As the accumulation front approaches this discontinuity, the current density is only slightly below j_{min}^s , and the accumulation front will accordingly move rather slowly, as is also evident from the electron density plot in Fig. 6.5. This effect is further enhanced by the flat slope at the discontinuity points of the down-sweep branches (as opposed to the steep slope at the discontinuity points of the up-sweep branches). If the final point is however farther away from the discontinuity, the switching time is reduced as is demonstrated by the current trace for $U_{\text{step}} = -0.51 \text{ V}$ in Fig. 6.3). The sharp spikes, associated with the well to well hopping of the maximum electron concentration can not be resolved

experimentally, however the plateau structure and the dependence of the switching time on the distance from the discontinuity agrees with the experimental results as shown by the experimental current traces in Fig. 6.4(b) [110].

6.1.2 Up Jumps

For up jumps, the final operating point turns out to depend non trivially on the exact value of U_{step} . Consider again the fixed initial voltage $U_i = 1.5 \text{ V}$. Then there exists a threshold voltage step U_{crit} , such that for small positive jumps $U_{\text{step}} < U_{\text{crit}}$, the final position of the operating point is located at the upper branch of the final voltage U_f on the next or the next but one branch (cf. orange and dark green arrows in Fig. 6.2). The corresponding current traces ($U_{\text{step}} = +0.1 \text{ V}$ and $U_{\text{step}} = +0.25 \text{ V}$ in Fig. 6.3) show a sharp current peak at the switching time, due to the sudden increase of all electric fields in the superlattice. As long as the current density surpasses j_{max}^s the accumulation front acquires a negative velocity due to Fig. 6.1(b). The front moves towards the emitter, as is evident from the charge density evolution for $U_{\text{step}} = +0.25 \text{ V}$ in Fig. 6.5. This motion decreases the fields again by Gauss's law (3.0.2), until the current density drops below j_{max}^s and the accumulation front stops. Similar to the case of down jumps, the relaxation time τ_r until the final current is reached depends sensitively on the distance of the final operating point from the previous branch discontinuity. Typically we have $\tau_r < 0.5 \mu\text{s}$.

For $U_{\text{step}} > U_{\text{crit}}$, the system behavior changes dramatically. Now the final operating point is on the lower branch of the final voltage U_f . This is surprising, since points on the down sweep branches, can ordinarily only be reached after first sweeping to higher voltages. Also the current trace shows a remarkable behavior, as shown for the voltages $U_{\text{step}} = +0.26, +0.4 \text{ V}$ in Fig. 6.3. The initial peak at the switching time, is followed immediately by a sharp drop to a level well below $j_{\text{min}}^s A$. The current then shows a spiky behavior, but remains on this plateau for about $6 \mu\text{s}$. It finally rises to a constant value, which corresponds to an operating point, which is located on the lower branch of the current voltage characteristic.

The explanation for this puzzling scenario can be seen from the electron density evolution in Fig. 6.5 (upper panels for $U_{\text{step}} = +0.26, +0.4 \text{ V}$). We see that at the switching time $t = 0$, the original accumulation front moves towards the emitter, just as in the $U_{\text{step}} = +0.25 \text{ V}$ case. But at the same time, a new dipole, consisting of a leading depletion and a trailing accumulation front is injected at the emitter. As we have learned in Section 3.3.1, this dipole injection is triggered by the rise of the current beyond j_c for a sufficiently long time. This triggering condition is fulfilled for $U_{\text{step}} > U_{\text{crit}}$. After the injection of the dipole, we obtain a tripole configuration, and according to Sec. 3.2, the current density is fixed at $j_{(2,1)}$ (Fig. 6.1), which explains the plateau like current trace in Fig. 6.3, which is also visible in the experimental data in Fig. 6.7(a). The well to well hopping of the fronts of the tripole are responsible for the spikes in this plateau. As the fronts move towards the collector, the depletion front moves at twice the velocity of the two accumulation fronts, as

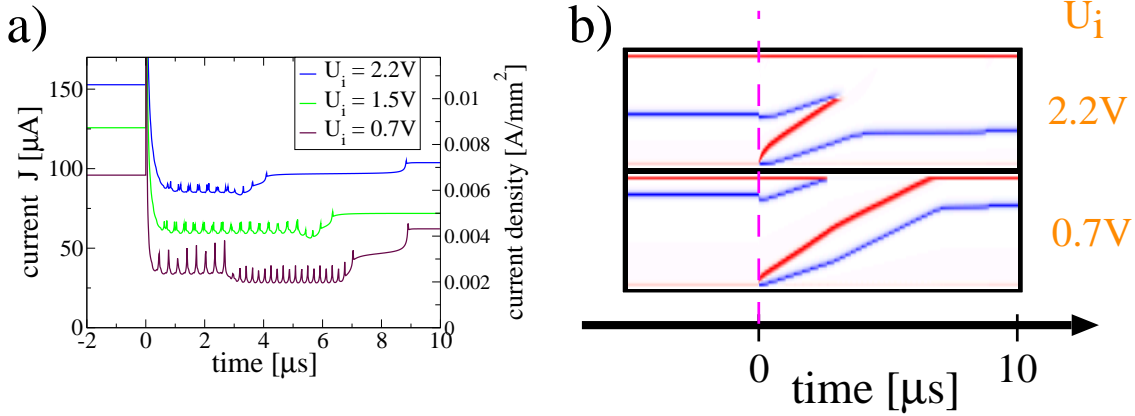


Figure 6.6: Current trace (a) and density evolution (b) for switching processes with varying U_i and fixed $U_{\text{step}} = +0.3\text{V}$.

discussed in Sec. 3.2, and reaches the collector shortly after the original electron accumulation front. Meanwhile the new accumulation front has traveled from the emitter towards the center and reaches its final position after the two other fronts have disappeared from the sample. We can now explain, why the final operating point is on the lower branch of the stationary current voltage characteristic. During a down sweep, the accumulation front also moves towards the collector, driven by a current below j_{min}^s . But since the same is true for the newly generated accumulation front, both processes have to lead to the same final state.

For $U_i = 1.5\text{V}$, the original accumulation front and the depletion front reach the collector at almost the same time. By choosing different initial voltage U_i , we can select other scenarios. Consider for instance the case $U_i = 0.7\text{V}$ in Fig. 6.6. Now the original accumulation front quickly reaches the collector, and we are left with a dipole. This is also visible from the current trace, which switches from the tripole current $j_{(2,1)}A$ to the lower dipole current j_dA , during the dipole phase. Although this effect seems to be small, it was demonstrated experimentally (cf. Fig. 6.7(b)) [110]. On the other hand for a larger $U_i = 2.2\text{V}$, the fast depletion front catches up with the original accumulation front, before it reaches the collector. In this case, the dipole phase is absent, and a shortened current trace is obtained (Fig. 6.6.)

The fact that dipole fronts are injected is related to our choice of the boundary currents. In Refs. [73, 115] switch on processes were considered and it was found that the domain formation is caused by a monopole mechanism. We can obtain equivalent scenarios by choosing $\sigma = 0.1\Omega^{-1}\text{m}^{-1}$, as shown in Fig. 6.8. Now with increasing U_{step} , there is a continuous transition from a direct relocation of the charge accumulation front ($U_{\text{step}} = +0.4\text{V}$) to a scenario, where the original accumulation front vanishes and a new accumulation front generated at the emitter forms the new domain boundary ($U_{\text{step}} = +0.9\text{V}$). At an intermediate voltage step of $U_{\text{step}} = +0.5\text{V}$, the original and the newly generated front at the emitter merge

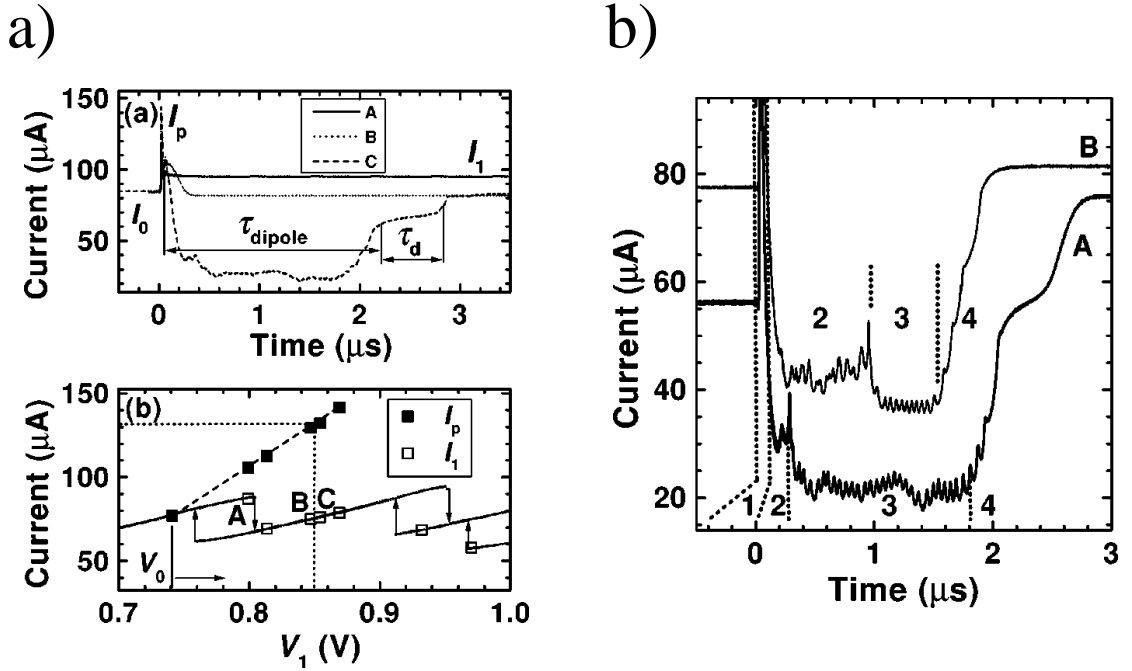


Figure 6.7: (a) Experimental current traces (upper panel) for up jumps from the third branch to the third (A) and fourth branch (B and C), respectively. The lower panel shows the final current (I_1) and the maximum current (I_p) during the jump. (b) Experimental current traces for switches from the third to the fifth branch (A) and from the tenth to the thirteenth branch (B) of the current voltage characteristic. The regions 2 and 3 correspond to the tripole and dipole phases, respectively. Reprinted from [110].

to the new domain boundary. This is apparently in violation of the basic rules of single front dynamics (see Chapter 3), which for instance require, that fronts of same polarity move in the same direction. However in Chapter 3, we were dealing with fully developed fronts, while the fronts appearing in Fig. 6.8(b) are only partly developed. Although the monopole mechanism is possible theoretically, the plateau like experimental current traces observed in Refs. [109, 110, 108] (cf. Fig. 6.9) show that the dipole mechanism are more common experimentally.

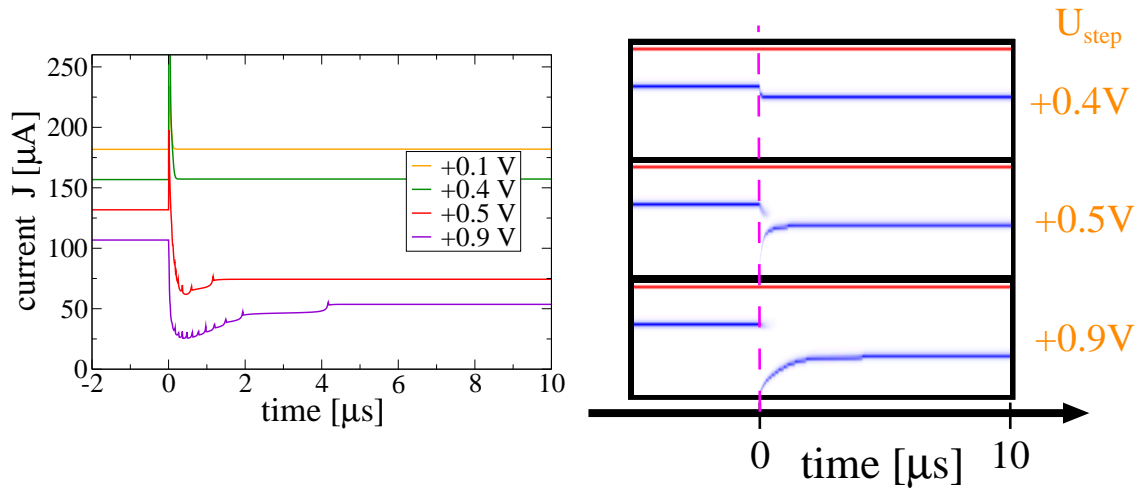


Figure 6.8: Current responses (left) and density evolution (right) for switching processes for a superlattice as in Fig. 6.2, but with $\sigma = 0.1 \Omega^{-1}\text{m}^{-1}$. Initial voltage $U_i = 1.5 \text{ V}$ and various U_{step} . The current traces in the left panel are shifted vertically by multiples of $25 \mu\text{A}$.

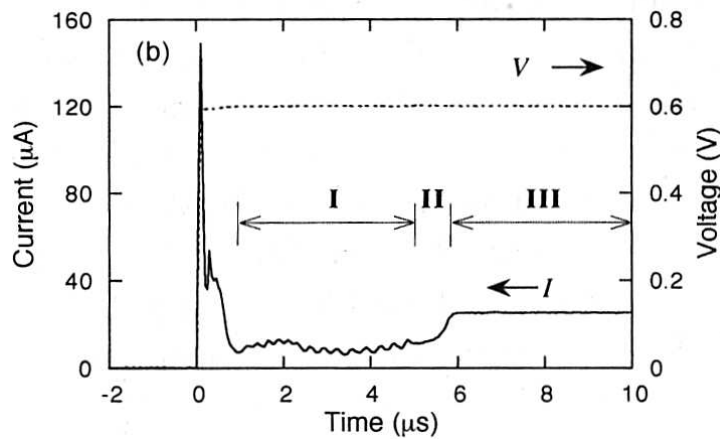


Figure 6.9: Experimental current trace of an $N = 20$ well superlattice for a voltage step from 0 to the second branch. Reprinted from [108].

6.2 Ramping

Experimentally it is not possible to switch the voltage instantaneously as in Eq. (6.1.1), but the effectively applied voltage will rather follow the ramp like form:

$$U(t) = \begin{cases} U_i & \text{for } t < -\tau_r, \\ U_i + \frac{\tau_r - t}{\tau_r} (U_{\text{step}}) & \text{for } -\tau_r \leq t < 0, \\ U_f = U_i + U_{\text{step}} & \text{for } t \geq 0, \end{cases} \quad (6.2.1)$$

with the ramping time τ_r .

Let us first consider the situation, where the final voltage U_f is close to the discontinuity point U_{disc} at which the current branch terminates. This situation was studied experimentally in Ref. [47]. We see from Fig. 6.11 that the current response depends sensitively on the exact value of the final voltage U_f . The branch at which the operating point at U_i is located if Fig. 6.11 has its discontinuity at $U_{\text{disc}} \approx 1.5738 \text{ V}$. Thus one could suppose that for $U_f < U_{\text{disc}}$ the final operating point is still on the original branch. This is however not the case, since for $U_f = 1.5737 \text{ V}$, the final operating point already is located on the next branch (cyan line in Fig. 6.11). Here the current rises during the ramping time, then at $t = 0$ quickly relaxes within less than $0.05 \mu\text{s}$ to a current which corresponds to an operating point on the original branch. At this level the current remains almost constant for a delay time of about $\tau_d = 1 \mu\text{s}$, before it finally drops to its final operating point on the next branch. The switching time for this final drop is about $\tau_s = 0.2 \mu\text{s}$. If we now further decrease U_f , the switching time τ_s remains approximately constant, but the delay time τ_d increases dramatically (right panel of Fig. 6.11), and diverges shortly before the final operating point remains on the same branch (green line in left panel of Fig. 6.11). This agrees with the experimental data from Ref. [47] (cf. Fig. 6.10).

It is now also interesting to consider the distribution of the relocation times for many switching processes with the same U_f . Experimentally it is not possible to specify U_f with arbitrary high accuracy and also the electron densities n_m will vary slightly with each switching process. For U_f far away from U_{disc} , the delay time τ_d can be neglected, and we obtain $\tau_{\text{rel}} \approx \tau_s \approx 0.2 \mu\text{s}$. Assuming a Gaussian distribution of U_f we expect that the distribution of τ_{rel} will also be Gaussian with a rather small variation σ . This is also found experimentally (cf. right inset in Fig. 6.10). However from Fig. 6.11 we see that for U_f close to the discontinuity point U_{disc} , the relocation time is extremely sensitive to variations δU_f of U_f . Additionally the sign of δU_f is important. Consider for instance the case $U_f = 1.57366 \text{ V}$ (violet line in Fig. 6.11(b)) with a relocation time $\tau_{\text{rel}} \approx 2.5 \mu\text{s}$. A variation of U_f by $\delta U_f = 0.01 \text{ mV}$ will yield a slightly lower $\tau_{\text{rel}} \approx 2.0 \mu\text{s}$. But a variation by $\delta U_f = -0.01 \text{ mV}$ (red line in Fig. 6.11(b)) approximately triples the relocation time to $\tau_{\text{rel}} \approx 7.9 \mu\text{s}$. Thus we expect that a Gaussian distribution in U_f translates to an asymmetric distribution of the relocation time τ_{rel} with a pronounced tail at large τ_{rel} . This behavior has also been observed experimentally, as shown in the left panel

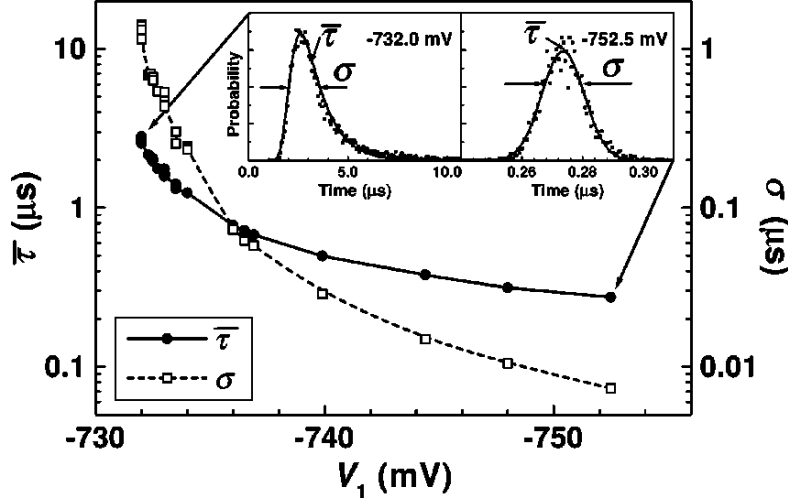


Figure 6.10: Average ($\bar{\tau}$) and width (σ) of the experimental relocation time distributions (insets) for up jumps from the third to the fourth branch at different final voltages. The discontinuity of the third branch is close to $V = -732.0$ mV. Reprinted from [47].

of Fig. 6.10. In the literature, however there exist two alternative explanations for this distribution, which propose that either thermal noise [116] or single electron tunneling [112] are responsible for the uncertainty in the relocation time. Such effects would however only dominate, if the final voltage U_f could be experimentally fixed with a very high precision, and the variation of U_f as the source of the distribution of the relocation time seems to be the more natural explanation.

6.3 Sweeping

Instead of only ramping to the next branch discontinuity, it is also interesting to sweep the voltage over several branches. We again use a voltage profile of the form (6.2.1).

A typical result of the current voltage characteristic for different sweep velocities is shown in Fig. 6.12(a). A large ramping time, such as $\tau_r = 10 \mu\text{s}$, merely reproduces the up sweep branch of the stationary current voltage characteristic in Fig. 6.2. With decreasing τ_r , the sharp drops at the discontinuity points of the branches are smeared out, and at the same time the current level rises (cf. $\tau_r = 4, 2, 0.7 \mu\text{s}$).

For even smaller $\tau_r = 0.6 \mu\text{s}$ (orange line in Fig. 6.12), the current shows a fundamentally different behavior. It first rises to a peak value of about $250 \mu\text{A}$ at $U = 1.5$ V, and then drops to current values about $120 \mu\text{A}$, with oscillations of about $15 \mu\text{A}$. The explanation for this phenomena is given again by the corresponding electron density plots (Fig. 6.12(b)). While for $\tau_r = 0.7 \mu\text{s}$ the original accumulation

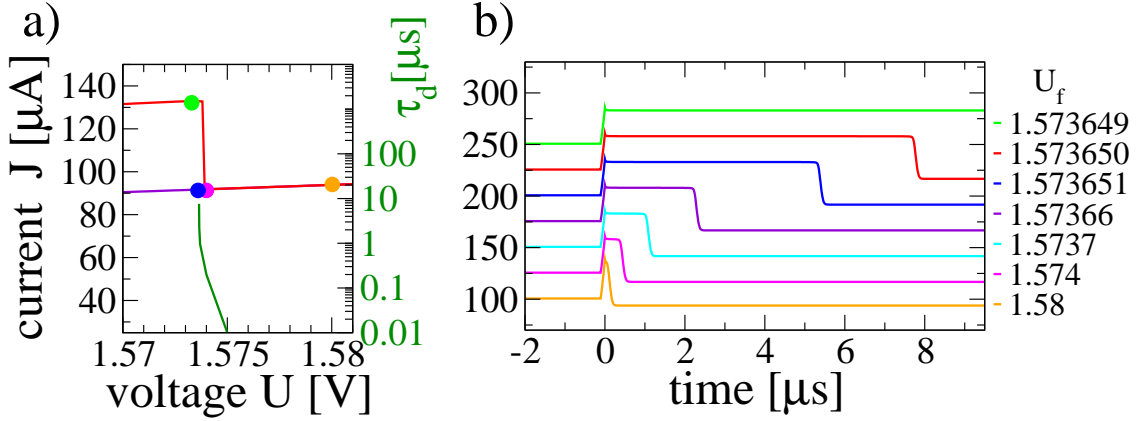


Figure 6.11: Ramping processes with $U_i = 1.5$ V and various final voltages U_f (colored points in (a)) close to the discontinuity of the original branch. The ramping time is $\tau_r = 100$ ns. The current traces in (b) are shifted vertically by multiples of $25 \mu\text{A}$.

front moves towards the emitter, for $\tau_r = 0.6 \mu\text{s}$, a new dipole is injected at the emitter, which is triggered by the large current peak. The leading depletion front of the dipole eventually merges with the original accumulation front, similar to the dynamics found for large positive switching voltages (cf. Fig. 6.6). However since the external voltage still increases during the tripole phase, the front trajectories in Fig. 6.12(b) are distorted, and the current during the tripole phase is larger than the classical tripole current $j_{(2,1)}$.

The findings of this section agrees well with experimental results [108, 110]. In particular in Ref. [110] (cf. Fig. 6.13) the importance of the triggering current was explicitly demonstrated.

6.4 Impedance

We now consider the response of a superlattice to a time dependent external voltage of the form

$$U(t) = U_{\text{dc}} + U_{\text{ac}} \sin(2\pi t/\tau_{\text{ac}}), \quad (6.4.1)$$

which is the sum of a dc voltage part U_{dc} , and an ac part which is characterized by the amplitude U_{ac} and the frequency $\omega_{\text{ac}} = 2\pi/\tau_{\text{ac}}$. Let us assume that for $U_{\text{ac}} = 0$, the superlattice contains a moving dipole consisting of an accumulation and a depletion front moving to the collector. From Sec. 3.2 we know that the fixed external voltage causes both fronts to move with the same velocity ($v_a = v_d$), which in turn fixes the current to j_d (cf. Fig. 3.13). This is of course not true, if the external voltage is not fixed. For example, if the external voltage increases the high field domain should grow, which is only possible, if the depletion front moves

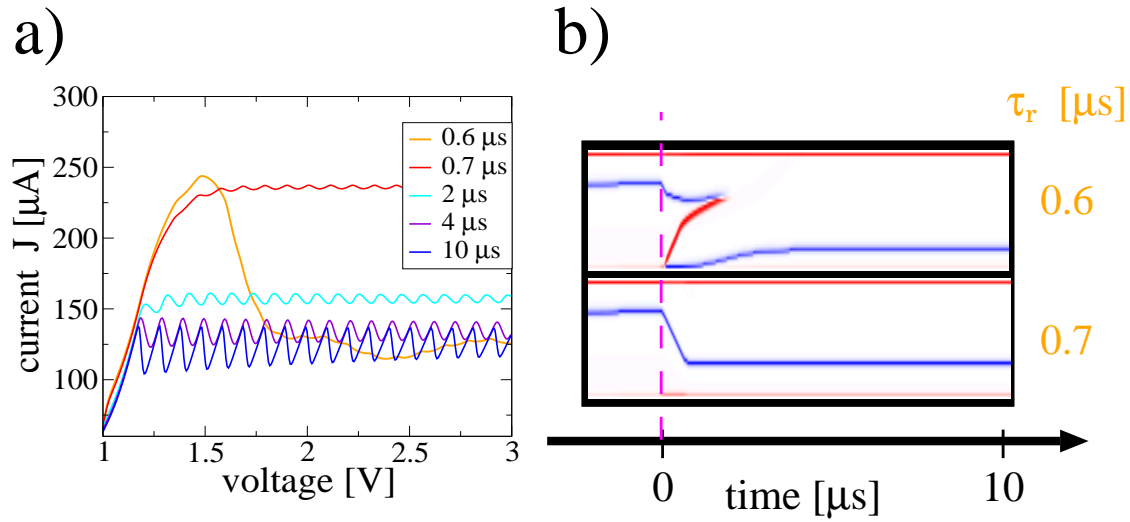


Figure 6.12: Current voltage characteristics (a) and density plots (b) for sweeping from $U_i = 1 \text{ V}$ to $U_i = 3 \text{ V}$ with various τ_r .

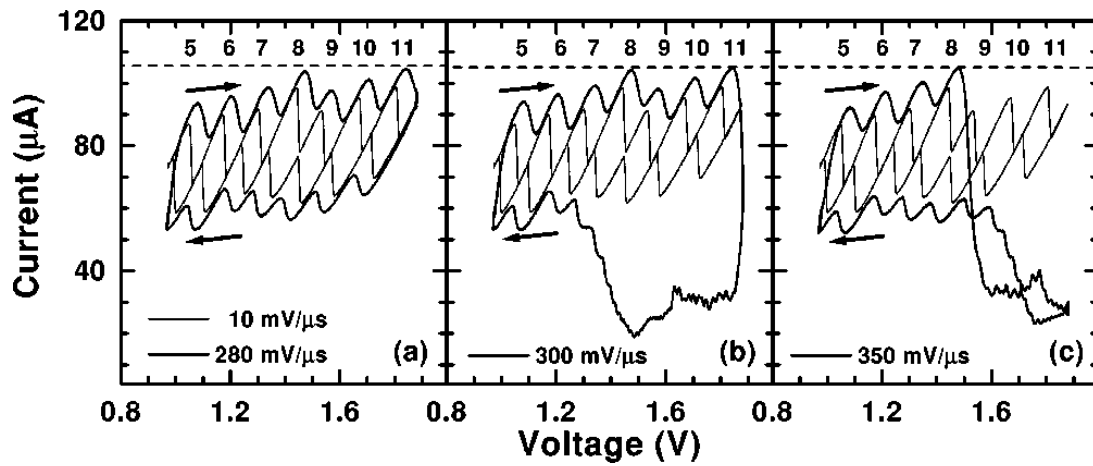


Figure 6.13: Experimental current voltage characteristic for triangular voltage sweeps at different sweep rates. The broken line denotes the critical current which triggers the dipole generation at the emitter. Reprinted from [110].

6 Nonstationary External Voltage

faster than the accumulation front. More precisely, from (4.2.1) we get

$$v_d(j) - v_a(j) = -\frac{\dot{U}}{F^h} + \frac{U \partial_j F^h(j) \partial j}{(F^h)^2 \partial t}, \quad (6.4.2)$$

where we have used the approximation $F^l \approx 0$. Similarly to (4.2.9) we approximate the left hand side of (6.4.2) by

$$v_d(j) - v_a(j) \approx k_v(j - j_d), \quad (6.4.3)$$

$$k_v = (\partial_j v_d(j_d) - \partial_j v_a(j_d)) \approx 2 \frac{d}{e N_D}. \quad (6.4.4)$$

For small voltages, we can neglect the second term on the right hand side of (6.4.2), and simply get

$$F^h k_v(j - j_d) = -\dot{U} = -i\omega U. \quad (6.4.5)$$

This gives rise to a purely imaginary impedance of

$$Z = \frac{U}{A(j - j_d)} = i \frac{F^h k_v}{\omega A}. \quad (6.4.6)$$

For a superlattice of type B we have $F^h \approx 5 \text{ MVm}$ and $k_v \approx 1.6 \cdot 10^{-4} \text{ m}^3/\text{Cb}$. For $\tau_{ac} = 1 \text{ ns}$, this yields,

$$Z = i \cdot 130 \text{ n}\Omega. \quad (6.4.7)$$

From the numerical simulation in Fig. 6.14, we obtain a somewhat smaller value $Z^{\text{num}} \approx i 60 \text{ n}\Omega$, but we see that the expected phase relation, between current density and the external voltage is accurately fulfilled.

We may note that (6.4.6) is only valid in the high frequency limit, when τ_{dc} is much smaller than the typical lifetime of the fronts. Furthermore the fronts have to be well separated from each other, in order to fulfill the velocity current characteristic for single fronts (cf. Fig. 3.13). Since this last condition is not fulfilled for the oscillation mode considered in Refs. [49, 117], their results can not be directly compared to the results in the present section.

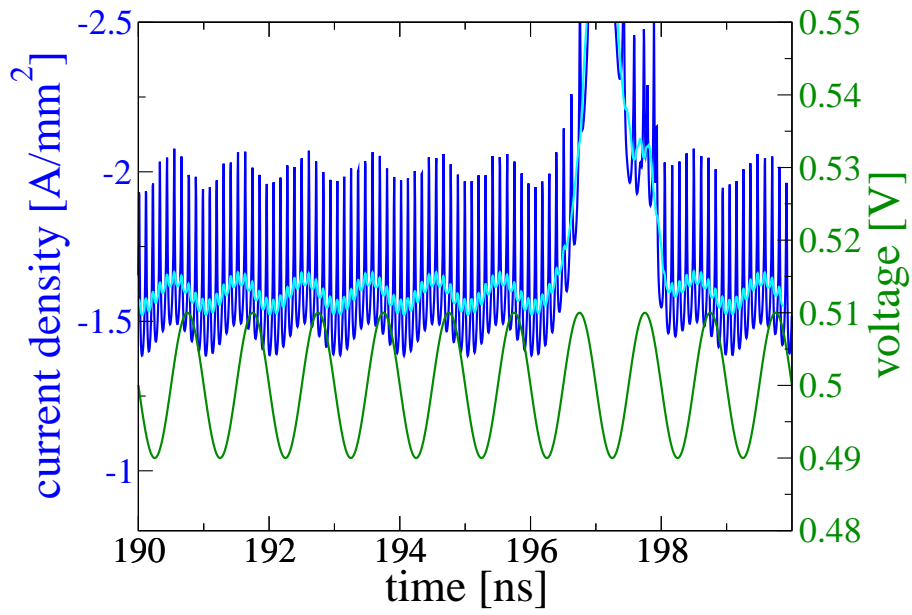


Figure 6.14: Current density trace (blue) for superlattice of type B with $\sigma = 1.3 \Omega^{-1} \text{m}^{-1}$, $U_{\text{dc}} = 0.5 \text{ V}$, $U_{\text{ac}} = 0.01 \text{ V}$ and $\tau_{\text{ac}} = 1 \text{ ns}$. The cyan line shows the time averaged current density over 0.05 ns . The electron density evolution is similar to Fig. 3.1(b).

6 *Nonstationary External Voltage*

7 Front Dynamics in Two Spatial Dimensions

Up to now we have considered the superlattice as a one dimensional device, and assumed that at any time each quantum well is homogeneously charged. In that case only the vertical charge transport from one quantum well to the next is responsible for the observed dynamical patterns. Such an assumption is only justified for small lateral well sizes, since then the relaxation time for charge fluctuations within one well is much faster than all other dynamical time scales.

In this chapter we will consider superlattices with large lateral extension. Then lateral patterns may contribute to the overall dynamics of the system. In particular the interaction between vertical and lateral patterns may give rise to qualitatively new scenarios.

7.1 Lateral Transport Theory

7.1.1 Dynamical Equations

Taking into account the lateral degrees of freedom, the new dynamical variables are the two dimensional charge densities $n_m(x, y)$, which now, in addition to the quantum well index m , also depend on the well plane coordinates $x \in [0, L_x]$ and $y \in [0, L_y]$ (here L_x and L_y are the extensions of the superlattice in x and y direction, respectively). The continuity equation (3.0.1) then generalizes to the new dynamical equation

$$e\dot{n}_m(x, y) = j_{m-1 \rightarrow m}^{\parallel} - j_{m \rightarrow m+1}^{\parallel} - \nabla_{\perp} \cdot \mathbf{j}_m^{\perp} \quad \text{for } m = 1, \dots, N, \quad (7.1.1)$$

with

$$j_{m \rightarrow m+1}^{\parallel}(x, y) = j_{m \rightarrow m+1}^{\parallel}(F_m^{\parallel}, n_m, n_{m+1}) \quad (7.1.2)$$

$$\nabla_{\perp} = \mathbf{e}_x \frac{\partial}{\partial x} + \mathbf{e}_y \frac{\partial}{\partial y}, \quad (7.1.3)$$

$$d\mathbf{j}_m^{\perp}(x, y) = -e\mu n_m \mathbf{F}_m^{\perp} - eD_0 \nabla_{\perp} n_m. \quad (7.1.4)$$

Here the lateral two-dimensional current density \mathbf{j}_m^{\perp} (units: [A/m]) is the sum of a drift and a diffusion term, characterized by the mobility μ and the diffusion

7 Front Dynamics in Two Spatial Dimensions

coefficient D_0 , respectively. The electric fields fulfill the semi-discrete version of Gauss's law

$$F_m^{\parallel} - F_{m-1}^{\parallel} + d\nabla_{\perp} \mathbf{F}_m^{\perp} = \frac{e}{\epsilon_r \epsilon_0} (n_m - N_D) \quad \text{for } m = 1, \dots, N, \quad (7.1.5)$$

with the boundary conditions

$$U = - \sum_{m=0}^N F_m^{\parallel}(x, y) d \quad \text{for } x \in [0, L_x], y \in [0, L_y], \quad (7.1.6)$$

$$\mathbf{F}_m^{\perp}(0, y) = \mathbf{F}_m^{\perp}(L_x, y) = \mathbf{F}_m^{\perp}(x, 0) = \mathbf{F}_m^{\perp}(x, L_y) = 0. \quad (7.1.7)$$

7.1.2 The Generalized Einstein Relation

The parameters μ and D_0 appearing in (7.1.4) are the mobility and the diffusion constant within the well, respectively. They are connected by a generalized form of the Einstein relation [118, 119]

$$D_0(n_m) = \frac{n_m}{-e\rho_0 (1 - \exp[-n_m/(\rho_0 k_B T)])} \mu, \quad (7.1.8)$$

with $\rho_0 = m/(\pi \hbar^2)$. Note that the mobility μ can in principle also depend on n , and that (7.1.8) can only be derived for the equilibrium case. In the following we make the assumptions that μ is fixed (for GaAs we assume $\mu \approx 10 \text{ m}^2/\text{Vs}$), and that (7.1.8) is still valid in the non-equilibrium case. Then we may rewrite (7.1.4) as

$$\mathbf{j}_m^{\perp}(x, y) = -e\mu n_m \left[\mathbf{F}_m^{\perp} + \frac{\nabla_{\perp} n_m}{-e\rho_0 (1 - \exp[-n/(\rho_0 k_B T)])} \right]. \quad (7.1.9)$$

7.1.3 Solving Poisson's Equation

For the integration of (7.1.1), it is necessary to solve (7.1.5) efficiently with respect to the electric fields \mathbf{F}_m^{\perp} and F_m^{\parallel} . This amounts to the solution of the semi-discrete Poisson equation for the potential $\varphi_m(x, y)$ of the form

$$\Delta \varphi_m(x, y) = (\Delta_{\perp} + \Delta_{\parallel}) \varphi_m(x, y) = -\frac{e}{d\epsilon_r \epsilon_0} (n_m - N_D) \quad \text{for } m = 1, \dots, N, \quad (7.1.10)$$

with

$$\Delta_{\perp} \varphi_m(x, y) = \left(\frac{\partial^2}{\partial x^2} + \frac{\partial^2}{\partial y^2} \right) \varphi_m(x, y), \quad (7.1.11)$$

$$\Delta_{\parallel} \varphi_m(x, y) = \frac{\varphi_{m-1}(x, y) - 2\varphi_m(x, y) + \varphi_{m+1}(x, y)}{d^2}. \quad (7.1.12)$$

A straightforward way for obtaining the potential φ_m from (7.1.10) would be to calculate the capacity matrix Δ^{-1} explicitly. With M the number of discretization

points in the (x, y) plane, this matrix would however have $(NM)^2$ elements, and we have to perform $O(N^2M^2)$ operations at every integration time step.

In search of a more efficient algorithm, we compare the contributions from $\Delta_{\perp}\varphi_m$ and $\Delta_{\parallel}\varphi_m$ in (7.1.10). In Ref. [119] the mean free path of the degenerate electrons in the well was estimated as $l_m \approx 0.3 \mu\text{m}$, and we may expect that typical structures in the lateral direction vary on a length scale which is even larger. Indeed it was found by numerical simulation of the very similar DBRT model that lateral structures typically occur on the length scale of about $l_t = 10 \mu\text{m}$ [21, 120, 121]. On the other hand, the variations of the potential in the vertical direction z is of the order of the superlattice period $d \approx 10 \text{ nm}$. We may therefore conclude that

$$\Delta_{\perp}\varphi_m \sim (l_t)^{-2} \ll \Delta_{\parallel}\varphi_m \sim d^{-2}. \quad (7.1.13)$$

This allows to invert the Laplace operator by the use of a perturbation expansion of the form,

$$\Delta^{-1} = (\Delta_{\perp} + \Delta_{\parallel})^{-1} = (1 + \Delta_{\parallel}^{-1}\Delta_{\perp})^{-1}\Delta_{\parallel}^{-1}, \quad (7.1.14)$$

$$\approx (1 - \Delta_{\parallel}^{-1}\Delta_{\perp} + \dots)\Delta_{\parallel}^{-1} = \Delta_{\parallel}^{-1} - \Delta_{\parallel}^{-2}\Delta_{\perp} + \dots. \quad (7.1.15)$$

In the last step we used the fact that Δ_{\perp} and Δ_{\parallel} commute. Applying (7.1.14) to (7.1.10) then yields

$$\varphi_m(x, y) = \varphi_m^0(x, y) + \varphi_m^1(x, y) + \dots, \quad (7.1.16)$$

$$\varphi_m^0(x, y) = -\frac{e}{d\epsilon_r\epsilon_0}\Delta_{\parallel}^{-1}(n_m - N_D), \quad (7.1.17)$$

$$\varphi_m^1(x, y) = +\frac{e}{d\epsilon_r\epsilon_0}\Delta_{\parallel}^{-2}\Delta_{\perp}n_m. \quad (7.1.18)$$

The advantage of such a solution for (7.1.10) lies in the fact that it can be calculated very efficiently. $\varphi_m^0(x, y)$ is evaluated by shooting with

$$\tilde{\varphi}_0^0(x, y) = \tilde{\varphi}_1^0(x, y) = 0, \quad (7.1.19)$$

$$\tilde{\varphi}_{m+1}^0(x, y) = 2\tilde{\varphi}_m^0 - \tilde{\varphi}_{m-1}^0 - \frac{ed}{\epsilon_r\epsilon_0}(n_m - N_D) \quad \text{for } m = 1 \dots N, \quad (7.1.20)$$

and then taking into account the corrections from the boundary conditions by

$$\varphi_m^0(x, y) = \tilde{\varphi}_m^0 + (U - \tilde{\varphi}_{N+1}^0)\frac{m}{N+1} \quad \text{for } m = 1 \dots N+1. \quad (7.1.21)$$

The algorithm described by (7.1.20) and (7.1.21) completes in only $O(NM)$ operations.

Also the matrix multiplication $\Delta_{\perp}n_m$ appearing in the calculation of $\varphi_m^1(x, y)$ in (7.1.17) is of $O(NM)$, since Δ_{\perp} is a matrix with only five entries per row. The operator Δ_{\parallel}^{-2} is simply evaluated by applying the algorithm of (7.1.20) twice and use a correction as in (7.1.21), but with $U = 0$.

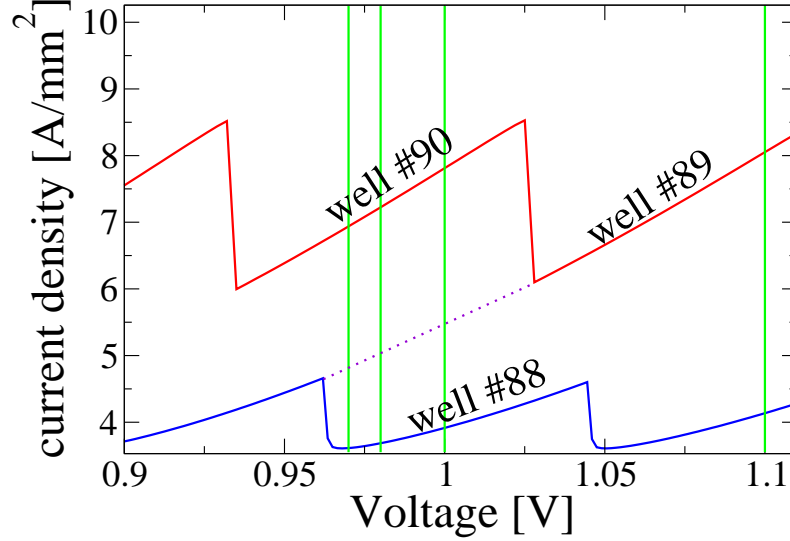


Figure 7.1: Homogeneous current voltage characteristic for superlattice of type B, with $\sigma = 500 \Omega^{-1}\text{m}^{-1}$ and $L_x = 50 \mu\text{m}$. The green lines denote the voltages considered in Fig. 7.3.

Once we have obtained the potential $\varphi_m(x, y)$, the electric fields are easily obtained in $O(NM)$ by

$$F_m^{\parallel}(x, y) = \frac{\varphi_{m+1}(x, y) - \varphi_m(x, y)}{d}, \quad (7.1.22)$$

$$\mathbf{F}_m^{\perp}(x, y) = -\nabla_{\perp} \varphi_m(x, y), \quad (7.1.23)$$

and can be used in (7.1.9) and (7.1.2) to calculate the current densities for the electron density evolution equation (7.1.1).

7.2 Stability of Inhomogeneous Lateral Patterns

For the numerical implementation of the scheme described in the Sec. 7.1, we use a superlattice of type B (see Table 2.2 on page 12), with a contact conductivity of $\sigma = 500 \Omega^{-1}\text{m}^{-1}$. Here we choose a large σ , in order to avoid front generation processes at the emitter. For simplicity we assume that the sample extension in the y direction is small, such that pattern formation can only occur in the x direction. We choose $L_x = 50 \mu\text{m}$ and $M = 25$ discretization points. We calculate $\varphi_m(x, y)$ only to the lowest order, and assume an effective diffusion constant of $D_0 \approx 0.01 \text{m}^2/\text{s}$.

In the homogeneous case without lateral pattern formation, the superlattice shows a stationary current voltage characteristic with branches associated with the peak of the electron charge distribution (Fig. 7.1) located in the well labeled by its number.

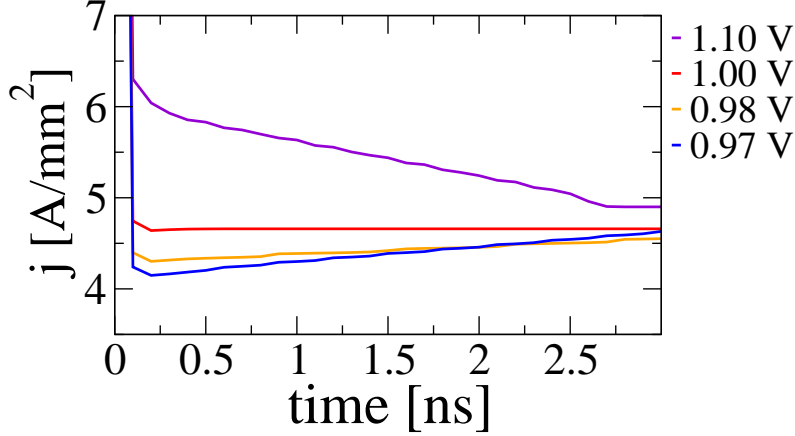


Figure 7.2: Current trace for superlattice parameters as in Fig. 7.1, with inhomogeneous initial condition at various voltages. At $t = 0$, accumulation fronts are placed in the left half of well 90 and the right half of well 88.

Due to the multistability apparent from Fig. 7.1, we may expect stable lateral patterns, where the superlattice is divided along the x axis into regions with varying operating points. We prepare initial conditions, with the left and right halves of the superlattice corresponding to operating points on branch number 90 and 88 respectively. This is achieved by putting electron accumulation fronts at the appropriate positions in well 90 and 88. We then study the response of this initial configuration to various voltages.

The resulting current traces and electron densities are shown in Fig. 7.2 and Fig. 7.3, respectively. We see that for $U = 0.97$ V the sharp current peak from the switch on of the external voltage, pushes the accumulation front in the left half from well 90 to 89 already at $t = 0.1$ ns. The current density is then given by the average of the current densities of the operating points at well 88 and 89. Subsequently the accumulation front at well 89 extends to the right and extrudes the accumulation front at 88, until at $t = 3.5$ ns we arrive at a homogeneous state with operating point at well 89. During this process the current density rises linearly to the value of the final operating point. For $U = 0.98$ V, we observe a similar behavior, but the time until the final operating point on branch 89 is reached, has approximately doubled. Note that the branch 89 wins over branch 88, although according to Fig. 7.1, both branches are stable at this voltage. This changes for $U = 1.0$ V, however, where the operating points on well 89 and 88 coexist (Fig. 7.3) for longer than the simulation time, and the final current is given by the average of the currents from both branches.

For an even higher voltage $U = 1.1$ V, we find that the switch-on-peak shifts both accumulation fronts by one well from well 90 and 88 to 89 and 87, respectively, within less than 0.1 ns. Then the electron accumulation from well 89 drops to well 88 starting from the middle of the sample, until at $t = 7$ ns we reach a stable

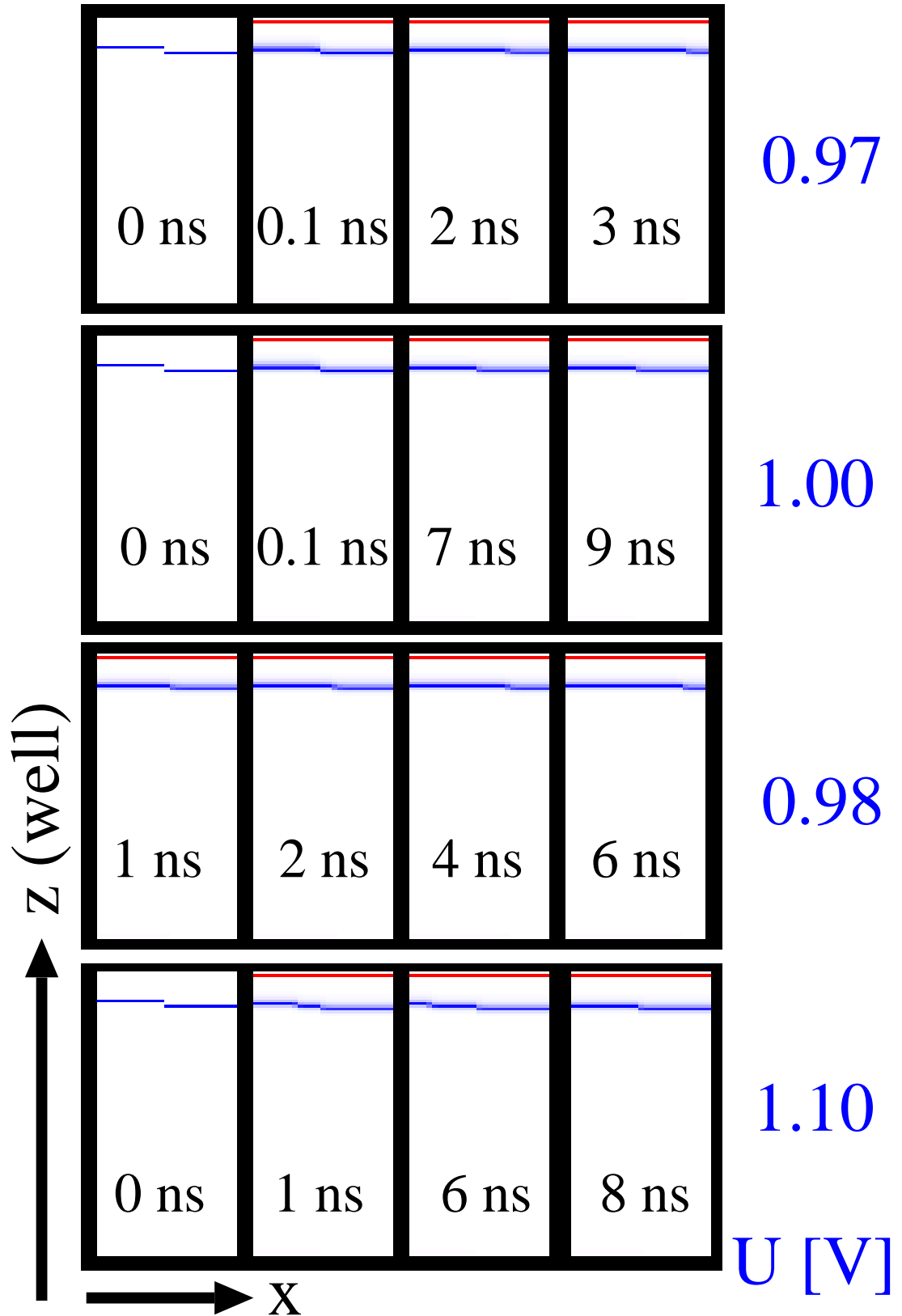


Figure 7.3: Electron density evolution for inhomogeneous initial conditions as in Fig. 7.2, shown in the (x, z) plane of the superlattice.

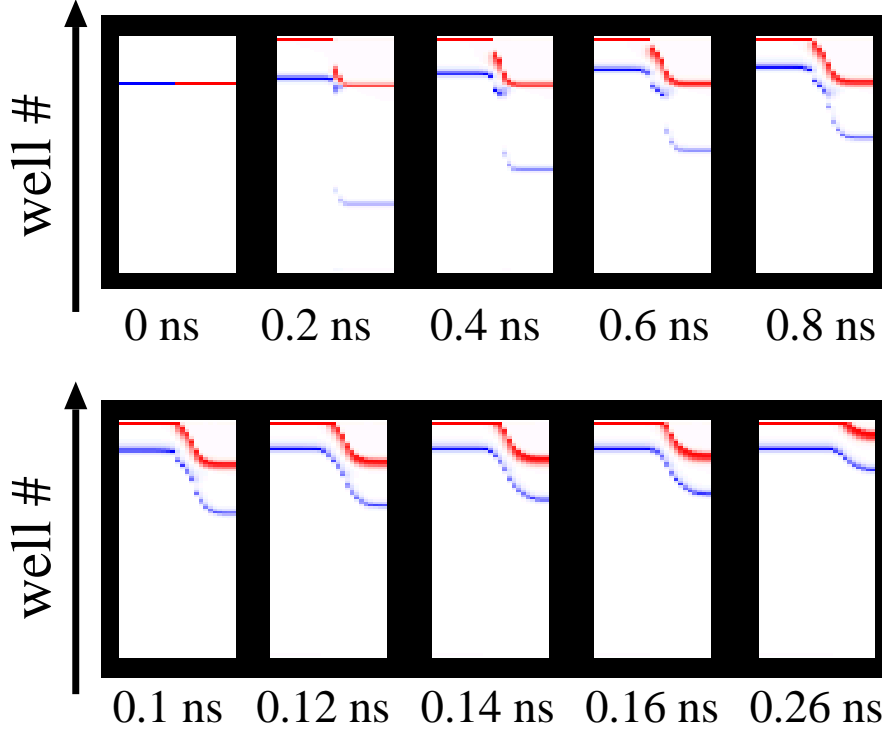


Figure 7.4: Superlattice as in Fig. 7.1 at $U = 1.0\text{V}$. Inhomogeneous initial condition with accumulation (depletion) front in left (right) half of well 80.

configuration with the left (right) half of the sample on branch 88 (87). During this transition, the current density drops linearly, as expected from the weighted average of the three involved operating points.

It is also interesting to consider an initial condition, with an accumulation front in the left half, and a depletion front in the right half of the same well. Such a configuration is shown in Fig. 7.4. We see that a new accumulation front is generated at the emitter in the right half of the sample, and moves towards the collector. Together with the already present fronts, we thus obtain a dipole in the left, and a monopole in the right part of the sample. As the dipole moves towards the collector, the monopole extends towards the right, until it eventually occupies the whole sample width. This behavior is also reflected by the corresponding current trace (cf. Fig. 7.5), which for $t > 1.0\text{ ns}$ can be explained as the weighted average of the dipole current j_d and the current of the final operating point.

In summary we have seen in this chapter that the lateral structures in superlattices reveal new aspects of front interaction processes, which are fundamentally different from the purely one-dimensional vertical interaction scenarios of Chapter 3. However, a more systematic analysis is still necessary, to gain a thorough understanding of the involved mechanisms. Such an analysis is however beyond the scope of the present work.

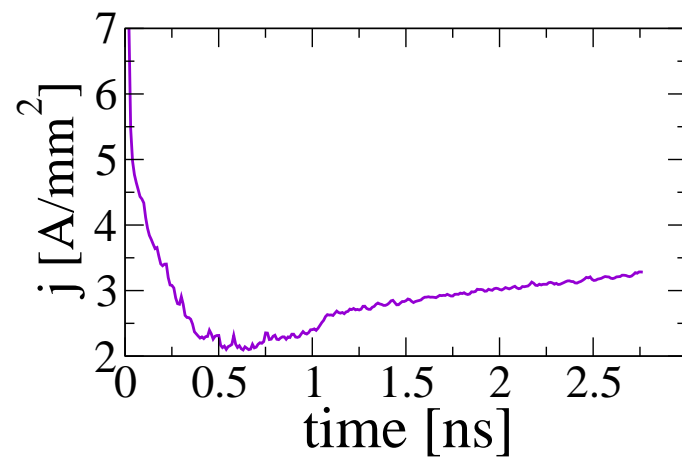


Figure 7.5: Current trace for the scenario in Fig. 7.4

8 Summary and Outlook

Semiconductor superlattices have been a focus of intensive research during the last decade. Experimentally a host of intriguing phenomena, such as self sustained high frequency oscillations, stationary field domains, or a remarkable response to the change of the external voltage has been observed. Theoretically, the dynamics of the superlattice has been described by various theories on different hierarchy levels. Examples are the Wannier-Stark ladder, the miniband transport model or the non-equilibrium Green's function theory. One reason for this interest in superlattices can be attributed to the expected technological applicability, for instance in Terahertz electronics, but from a more fundamental point of view, the significance of the superlattice as a nonlinear model system, is equally important. In particular the fact that it provides a rich front dynamics, has proved to be fruitful throughout this work.

We founded our analysis on a semiclassical sequential tunneling model for the electrons, which is motivated by quantum mechanical considerations. The resulting nonlinear transport equations give rise to the formation of electron accumulation and depletion fronts, which form the boundaries between high and low field domains. It is thus natural to look for a description of the superlattice dynamics in terms of fronts. Such a front model provides a new hierarchical level on top of the semiclassical model.

With this aim, we first study the propagation, generation and annihilation of single fronts in detail. It was found in Chapter 3 that the front velocities are determined by the overall current density, while the generation of fronts at the emitter is governed by the nature of the emitter contact, characterized by the contact conductivity σ . Fronts disappear from the system, as they either reach the collector, or collide with a front of opposite polarity. It is this latter possibility of front annihilation that allows for particularly interesting scenarios, such as chaotic behavior under fixed external voltage conditions. We have demonstrated in Chapter 4 that large parts of the bifurcation scenarios of the microscopic model can be reproduced by a model which uses the front positions as the dynamical variables. This front model has a very generic structure, and it may be relevant for other globally constrained front systems as well.

As shown in Chapter 5, a further simplification of the front model applies, if the fronts do not reach the collector. In this case the front model maps to a tank model, which describes the filling heights of a number of water tanks. The tanks are filled and drained by a given set of rules. Similar models are obtained generically in various areas of science and engineering, for instance in the context of production

processes. The tank model can be described analytically by iterated maps. In Chapter 5 we explicitly constructed the maps for the first two nontrivial cases $n = 3$ and $n = 4$. It is shown that the map for $n = 3$ follows the universal U-sequence of periods, which appears in a large class of one dimensional iterated maps. This finally explains the peculiar bifurcation scenario observed in the microscopic model.

Experimentally, the current response of superlattices shows surprising features, under sweeping or switching of the external voltage. For example, it is possible to reach the down sweep branch of the stationary current voltage characteristic by a fast voltage increase. As demonstrated in Chapter 6, such effects can be naturally explained in terms of the front dynamics.

Apart from the fronts in vertical direction, fronts are also possible in lateral direction. In Chapter 7 we extend the superlattice to include one additional lateral dimension, and found that the stability of the corresponding lateral patterns depends sensitively on the applied voltage.

Although the front model explains a large part of the superlattice dynamics, there are nevertheless scenarios, which are not yet reproduced successfully, and should be the object of future research on this subject. One failure of the front model obviously arises from fronts, which are not fully developed. Here the model could possibly be extended to at least take into account the “excitonic” fronts, which were discussed in Sec. 4.1.1, and appear to be the most important correction to the front model. It would also be worthwhile to understand, which parameters of the superlattice influence the success of the front model. It may then be possible to find a clear $n = 4$ or $n = 5$ scenario as in Fig. 4.11, in the microscopic model. Such considerations may also help the experimentalists to construct superlattices, which show self generated chaoticity. Furthermore the front model does not satisfactorily reproduce the case where fronts reach the collector, and a more detailed analysis of the collector contact seems to be necessary.

Interesting new effects are also expected from a further analysis of the lateral instabilities in the superlattice. In this work we have only laid out the basic lateral transport theory, but a detailed understanding of the interaction between vertical and lateral fronts is still missing.

Last but not least a more ambitious extension of this work would be to check the universality of the presented methods by applying them in a more general context. As a first step it would be useful to derive a generalized front model from a more generic, probably continuous model. A second step would then be to find concrete examples of front systems, which can be described by such a front model. The hope is, that in the course of this work, a unified theory encompassing general front interactions will emerge.

Acknowledgement

I am grateful to my supervisor Prof. Ekehard Schöll for his valuable advice and support. He directed me to interesting topics of research and at the same time permitted me to follow my own ideas. I am indebted to Dr. Andreas Wacker for introducing me to the details of the superlattice model, and for many helpful hints throughout this work. I would like to thank Prof. Harald Engel for making the second assessment of this thesis.

I appreciate the collaboration with the experimentalists Marco Rogozia in Berlin and Dr. Ekkehard Schomburg in Regensburg who provided the experimental basis for this theoretical research.

This work also profited from the invitation of Prof. Luis Bonilla to visit his group in Madrid and the subsequent collaboration.

I thank Anne-Katharina Jappsen for her contributions in the non stationary voltage case, Dr. Toni Lee for the vivid discussions on decoherence, Karsten Peters for the intense collaboration on the tank model, Dr. Pavel Rodin for his help on the lateral dynamics and Jan Schlesner for his extensive numerical support which substantiated many theoretical concepts of this thesis.

Last but not least I want to thank the present and former colleagues at the ITP for the enjoyable atmosphere, in particular Reinhard Wetzler, with whom I shared an office for the past years.

This work was supported by DFG in the framework of Sfb 555.

Bibliography

- [1] J. S. Langer: *Instabilities and pattern formation in crystal growth*, Rev. Mod. Phys. **52**, 1 (1980).
- [2] B. Boroson, R. McCray, C. O. Clark, J. Slavin, M.-M. M. Low, Y.-H. Chu, and D. V. Buren: *An interstellar conduction front within a wolf-rayet ring nebula observed with the GHRIS*, Astrophysical Journal **478**, 638 (1997).
- [3] A. M. Zhabotinskii: *Periodic processes of the oxidation of malonic acid in solution*, Biofizika **9**, 306 (1964).
- [4] R. Kapral and K. Showalter (Editors): *Chemical Waves and Patterns* (Kluwer Academic Publishers, 1995).
- [5] A. G. Merzhanov and E. N. Rumanov: *Physics of reaction waves*, Rev. Mod. Phys. **71**, 1173 (1999).
- [6] J. M. Davidenko, A. M. Pertsov, R. Salomonsz, W. Baxter, and J. Jalife: *Stationary and drifting spiral waves of excitation in isolated cardiac muscle*, Nature **355**, 349 (1992).
- [7] O. Steinbock, F. Siegert, S. C. Müller, and C. J. Weijer: *Three-dimensional waves of excitation during dictyostelium morphogenesis*, Proc. Natl. Acad. Sci. **90**, 7332 (1993).
- [8] M. C. Cross and P. C. Hohenberg: *Pattern formation outside of equilibrium*, Rev. Mod. Phys. **65**, 851 (1993).
- [9] A. S. Mikhailov: *Foundations of Synergetics Vol. I* (Springer, Berlin, 1994), 2nd ed.
- [10] G. Falkovich, K. Gawdzki, and M. Vergassola: *Particles and fields in fluid turbulence*, Rev. Mod. Phys. **73**, 913 (2001).
- [11] J. B. Gunn: *Microwave oscillations of current in III-V semiconductors*, Sol. Stat. Comm. **1**, 88 (1963).
- [12] V. L. Bonch-Bruевич, I. P. Zvyagin, and A. G. Mironov: *Domain electrical instabilities in semiconductors* (Consultant Bureau, New York, 1975).

Bibliography

- [13] E. Schöll: *Nonequilibrium Phase Transitions in Semiconductors* (Springer, Berlin, 1987).
- [14] M. P. Shaw, V. V. Mitin, E. Schöll, and H. L. Grubin: *The Physics of Instabilities in Solid State Electron Devices* (Plenum Press, New York, 1992).
- [15] J. Peinke, J. Parisi, O. RöSSLer, and R. Stoop: *Encounter with Chaos* (Springer, Berlin, Heidelberg, 1992).
- [16] E. Schöll, F.-J. Niedernostheide, J. Parisi, W. Prettl, and H. Purwins: *Formation of spatio-temporal structures in semiconductors*, in *Evolution of spontaneous structures in dissipative continuous systems*, edited by F. H. Busse and S. C. Müller (Springer, Berlin, 1998), pp. 446–494.
- [17] K. Aoki: *Nonlinear dynamics and chaos in semiconductors* (Institute of Physics Publishing, Bristol, 2000).
- [18] E. Schöll: *Nonlinear spatio-temporal dynamics and chaos in semiconductors* (Cambridge University Press, Cambridge, 2001), Nonlinear Science Series, Vol. 10.
- [19] A. Wacker and E. Schöll: *Oscillatory instability in the heterostructure hot-electron diode*, Appl. Phys. Lett. **59**, 1702 (1991).
- [20] M. Meixner, P. Rodin, and E. Schöll: *Accelerated, decelerated and oscillating fronts in a globally coupled bistable semiconductor system*, Phys. Rev. E **58**, 2796 (1998).
- [21] M. Meixner, P. Rodin, E. Schöll, and A. Wacker: *Lateral current density fronts in globally coupled bistable semiconductors with S- or Z-shaped current voltage characteristic*, Eur. Phys. J. B **13**, 157 (2000).
- [22] E. Schomburg, R. Scheuerer, S. Brandl, K. F. Renk, D. G. Pavel'ev, Y. Koschurinov, V. Ustinov, A. Zhukov, A. Kovsh, and P. S. Kop'ev: *In-GaAs/InAlAs superlattice oscillator at 147 GHz*, Electronics Letters **35**, 1491 (1999).
- [23] J. Schlesner, A. Amann, N. B. Janson, W. Just, and E. Schöll: *Self-stabilization of high frequency oscillations in semiconductor superlattices by time-delay autosynchronization*, Phys. Rev. E **68**, 066208 (2003), cond-mat/0303462.
- [24] J. Schlesner, A. Amann, N. B. Janson, W. Just, and E. Schöll: *Self-stabilization of chaotic domain oscillations in superlattices by time-delayed feedback control*, Semicond. Sci. Technol. (2004).

- [25] J. Faist, F. Capasso, D. L. Sivco, C. Sirtori, A. L. Hutchinson, and A. Y. Cho: *Quantum cascade laser*, *Science* **264**, 553 (1994).
- [26] C. Gmachl, F. Capasso, D. L. Sivco, and A. Y. Cho: *Recent progress in quantum cascade lasers and applications*, *Rep. Prog. Phys.* **64**, 1533 (2001).
- [27] A. Wacker: *Semiconductor superlattices: A model system for nonlinear transport*, *Phys. Rep.* **357**, 1 (2002).
- [28] G. Bastard: *Wave Mechanics Applied to Semiconductor Heterostructures* (Les Editions de Physique, Les Ulis Cedex, France, 1988).
- [29] E. Schöll (Editor): *Theory of Transport Properties of Semiconductor Nanostructures*, vol. 4 of *Electronic Materials Series* (Chapman and Hall, London, 1998).
- [30] L. L. Bonilla: *Theory of nonlinear charge transport, wave propagation, and self-oscillations in semiconductor superlattices*, *J. Phys.: Condens. Matter* **14**, R341 (2002).
- [31] G. Brozak, E. A. de Andrada e Silva, L. J. Sham, F. DeRosa, P. Miceli, S. A. Schwarz, J. P. Harbison, L. T. Florez, and S. J. Allen: *Tunneling cyclotron resonance and the renormalized effective mass in semiconductor barriers*, *Phys. Rev. Lett.* **64**, 471 (1990).
- [32] I. Vurgaftman, J. R. Meyer, and L. R. Ram-Mohan: *Band parameters for III-V compound semiconductors and their alloys*, *J. Appl. Phys.* **89**, 5815 (2001).
- [33] R. d. L. Kronig and W. G. Penney: *Quantum mechanics of electrons in crystal lattices*, *Proc. Royal Soc. A* **130**, 499 (1931).
- [34] H. D. Zeh: *On the interpretation of measurement in quantum theory*, *Found. Phys.* **1**, 69 (1970).
- [35] D. Giulini, E. Joos, C. Kiefer, J. Kupsch, I.-O. Stamatescu, and H. D. Zeh: *Decoherence and the Appearance of a Classical World in Quantum Theory* (Springer, Berlin, 1996).
- [36] M. B. Mensky: *Quantum Measurements and Decoherence* (Kluwer Academic Publishers, Dordrecht, 2000).
- [37] W. M. Itano, D. J. Heinzen, J. J. Bollinger, and D. J. Wineland: *Quantum Zeno effect*, *Phys. Rev. A* **41**, 2295 (1990).
- [38] H. Everett III: *Relative state formulation of quantum mechanics*, *Rev. Mod. Phys.* **29**, 454 (1957).

Bibliography

- [39] G. Lindblad: *On the generators of quantum dynamical semigroups*, Commun. Math. Phys. **48**, 119 (1976).
- [40] R. Scheuerer, E. Schomburg, K. F. Renk, A. Wacker, and E. Schöll: *Feasibility of a semiconductor superlattice oscillator based on quenched domains for the generation of sub-millimeter waves*, Appl. Phys. Lett. **81**, 1515 (2002).
- [41] G. H. Wannier: *The structure of electronic excitation levels in insulating crystals*, Phys. Rev. **52**, 191 (1937).
- [42] A. Wacker: *Vertical transport and domain formation in multiple quantum wells*, in *Theory of Transport Properties of Semiconductor Nanostructures*, edited by E. Schöll (Chapman and Hall, London, 1998), chap. 10.
- [43] A. Wacker and A.-P. Jauho: *Quantum transport: The link between standard approaches in superlattices*, Phys. Rev. Lett. **80**, 369 (1998).
- [44] H. Steuer, A. Wacker, E. Schöll, M. Ellmauer, E. Schomburg, and K. F. Renk: *Thermal breakdown, bistability, and complex high-frequency current oscillations due to carrier heating in superlattices*, Appl. Phys. Lett. **76**, 2059 (2000).
- [45] H. Steuer, A. Wacker, and E. Schöll: *Complex behavior due to electron heating in superlattices exhibiting high-frequency current oscillations*, Physica B **272**, 202 (1999).
- [46] J. Kastrup, R. Klann, H. T. Grahn, K. Ploog, L. L. Bonilla, J. Galán, M. Kindelan, M. Moscoso, and R. Merlin: *Self-oscillations of domains in doped GaAs-AlAs superlattices*, Phys. Rev. B **52**, 13761 (1995).
- [47] M. Rogozia, S. W. Teitsworth, H. T. Grahn, and K. H. Ploog: *Statistics of the domain-boundary relocation time in semiconductor superlattices*, Phys. Rev. B **64**, 041308 (2001).
- [48] S. Zeuner, S. J. Allen, K. D. Maranowski, and A. C. Gossard: *Photon-assisted tunneling in GaAs/AlGaAs superlattices up to room temperature*, Appl. Phys. Lett. **69**, 2689 (1996).
- [49] A.-K. Jappsen, A. Amann, A. Wacker, E. Schomburg, and E. Schöll: *High frequency impedance of driven superlattices*, J. Appl. Phys. **92**, 3137 (2002).
- [50] E. Schomburg, K. Hofbeck, R. Scheuerer, M. Haeussler, K. F. Renk, A.-K. Jappsen, A. Amann, A. Wacker, E. Schöll, D. G. Pavel'ev, and Y. Koschurinov: *Control of the dipole domain propagation in a GaAs/AlAs superlattice with a high-frequency field*, Phys. Rev. B **65**, 155320 (2002).

- [51] R. Aguado, G. Platero, M. Moscoso, and L. L. Bonilla: *Microscopic model for sequential tunneling in semiconductor multiple quantum wells*, Phys. Rev. B **55**, 16053 (1997).
- [52] D. Sánchez, M. Moscoso, L. L. Bonilla, G. Platero, and R. Aguado: *Current self-oscillations, spikes and crossover between charge monopole and dipole waves in semiconductor superlattices*, Phys. Rev. B **60**, 4489 (1999).
- [53] A. Amann, J. Schlesner, A. Wacker, and E. Schöll: *Self-generated chaotic dynamics of field domains in superlattices*, in *Proc. 26th International Conference on the Physics of Semiconductors (ICPS-26), Edinburgh 2002*, edited by J. H. Davies and A. R. Long (2003).
- [54] M. Rogozia, P. Krispin, and H. T. Grahn: *Giant resistance changes in (Al,Ga)As contact layers of GaAs/AlAs superlattices due to deep donors*, J. Appl. Phys. **90**, 4560 (2001).
- [55] F. Prengel, A. Wacker, and E. Schöll: *Simple model for multistability and domain formation in semiconductor superlattices*, Phys. Rev. B **50**, 1705 (1994), *ibid* **52**, 11518 (1995).
- [56] A. Wacker, G. Schwarz, F. Prengel, E. Schöll, J. Kastrup, and H. T. Grahn: *Probing growth-related disorder by high-field transport in semiconductor superlattices*, Phys. Rev. B **52**, 13788 (1995).
- [57] G. Schwarz, A. Wacker, F. Prengel, E. Schöll, J. Kastrup, H. T. Grahn, and K. Ploog: *Influence of imperfections and weak disorder on domain formation in superlattices*, Semicond. Sci. Technol. **11**, 475 (1996).
- [58] E. Schöll, G. Schwarz, M. Patra, F. Prengel, and A. Wacker: *Oscillatory instabilities and field domain formation in imperfect superlattices*, in *Proc. 9th Int. Conf. on Hot Carriers in Semiconductors, Chicago 1995*, edited by K. Hess, J. P. Leburton, and U. Ravaioli (Plenum Press, New York, 1996), pp. 177–181.
- [59] G. Schwarz and E. Schöll: *Field domains in semiconductor superlattices*, phys. status solidi (b) **194**, 351 (1996).
- [60] G. Schwarz, F. Prengel, E. Schöll, J. Kastrup, H. T. Grahn, and R. Hey: *Electric field domains in intentionally perturbed semiconductor superlattices*, Appl. Phys. Lett. **69**, 626 (1996).
- [61] M. Patra, G. Schwarz, and E. Schöll: *Bifurcation analysis of stationary and oscillating field domains in semiconductor superlattices with doping fluctuations*, Phys. Rev. B **57**, 1824 (1998).

Bibliography

- [62] G. Grüner: *The dynamics of charge-density waves*, Rev. Mod. Phys. **60**, 1129 (1988).
- [63] J. P. Keener and J. Sneyd: *Mathematical physiology* (Springer, New York, Berlin, 1998).
- [64] S. Flach, Y. Zolotaryuk, and K. Kladko: *Moving lattice kinks and pulses: An inverse method*, Phys. Rev. E **59**, 6105 (1999).
- [65] A. Carpio and L. L. Bonilla: *Depinning transitions in discrete reaction-diffusion equations*, SIAM J. Appl. Math. **63**, 1056 (2003).
- [66] L. L. Bonilla, M. Kindelan, M. Moscoso, and S. Venakides: *Periodic generation and propagation of travelling fronts in dc voltage biased semiconductor superlattices*, SIAM J. Appl. Math. **57**, 1588 (1997).
- [67] A. Carpio, L. L. Bonilla, A. Wacker, and E. Schöll: *Wavefronts may move upstream in semiconductor superlattices*, Phys. Rev. E **61**, 4866 (2000).
- [68] A. Amann, A. Wacker, L. L. Bonilla, and E. Schöll: *Dynamic scenarios of multi-stable switching in semiconductor superlattices*, Phys. Rev. E **63**, 066207 (2001).
- [69] A. Carpio, L. L. Bonilla, and G. Dell'Acqua: *Motion of wave fronts in semiconductor superlattices*, Phys. Rev. E **64**, 036204 (2001).
- [70] J. Kastrup, R. Hey, K. H. Ploog, H. T. Grahn, L. L. Bonilla, M. Kindelan, M. Moscoso, A. Wacker, and J. Galán: *Electrically tunable GHz oscillations in doped GaAs-AlAs superlattices*, Phys. Rev. B **55**, 2476 (1997).
- [71] L. L. Bonilla, J. Galán, J. A. Cuesta, F. C. Martínez, and J. M. Molera: *Dynamics of electric field domains and oscillations of the photocurrent in a simple superlattice model*, Phys. Rev. B **50**, 8644 (1994).
- [72] A. Wacker, M. Moscoso, M. Kindelan, and L. L. Bonilla: *Current-voltage characteristic and stability in resonant-tunneling n-doped semiconductor superlattices*, Phys. Rev. B **55**, 2466 (1997).
- [73] J. Kastrup, F. Prengel, H. T. Grahn, K. Ploog, and E. Schöll: *Formation times of electric field domains in doped GaAs-AlAs superlattices*, Phys. Rev. B **53**, 1502 (1996).
- [74] O. M. Bulashenko and L. L. Bonilla: *Chaos in resonant-tunneling superlattices*, Phys. Rev. B **52**, 7849 (1995).
- [75] K. N. Alekseev, G. P. Berman, D. K. Campbell, E. H. Cannon, and M. C. Cargo: *Dissipative chaos in semiconductor superlattices*, Phys. Rev. B **54**, 10625 (1996).

- [76] L. L. Bonilla, O. M. Bulashenko, J. Galán, M. Kindelan, and M. Moscoso: *Dynamics of electric-field domains and chaos in semiconductor superlattices*, Sol. State El. **40**, 161 (1996).
- [77] O. M. Bulashenko, K. J. Luo, H. T. Grahn, K. H. Ploog, and L. L. Bonilla: *Multifractal dimension of chaotic attractors in a driven semiconductor superlattice*, Phys. Rev. B **60**, 5694 (1999).
- [78] J. C. Cao and X. L. Lei: *Synchronization and chaos in miniband semiconductor superlattices*, Phys. Rev. B **60**, 1871 (1999).
- [79] Y. Zhang, J. Kastrup, R. Klann, K. H. Ploog, and H. T. Grahn: *Synchronization and chaos induced by resonant tunneling in GaAs/AlAs superlattices*, Phys. Rev. Lett. **77**, 3001 (1996).
- [80] K. J. Luo, H. T. Grahn, K. H. Ploog, and L. L. Bonilla: *Explosive bifurcation to chaos in weakly coupled semiconductor superlattices*, Phys. Rev. Lett. **81**, 1290 (1998).
- [81] A. Amann, J. Schlesner, A. Wacker, and E. Schöll: *Chaotic front dynamics in semiconductor superlattices*, Phys. Rev. B **65**, 193313 (2002).
- [82] I. R. Cantalapiedra, M. J. Bergmann, L. L. Bonilla, and S. W. Teitworth: *Chaotic motion of space charge wave fronts in semiconductors under time independent voltage bias*, Phys. Rev. E **63**, 056216 (2001).
- [83] M. Or-Guil, I. G. Kevrekidis, and M. Bär: *Stable bound states of pulses in an excitable medium*, Physica D **135**, 154 (2000).
- [84] J. Schlesner and A. Amann: *Superlattice bifurcation scenarios* (2003), private communication.
- [85] A. Wolf, J. Swift, H. Swinney, and J. Vastano: *Determining Lyapunov exponents from a time series*, Physica D **16**, 285 (1985).
- [86] A. Amann, K. Peters, U. Parlitz, A. Wacker, and E. Schöll: *A hybrid model for chaotic front dynamics: From semiconductors to water tanks*, Phys. Rev. Lett. **91**, 066601 (2003).
- [87] R. Alur, C. Courcoubetis, N. Halbwachs, T. A. Henzinger, X. N. P.-H. Ho, A. Olivero, J. Sifakis, and S. Yovine: *The algorithmic analysis of hybrid systems*, Theoretical Computer Science **138**, 3 (1995).
- [88] C. Chase, J. Serrano, and P. J. Ramadge: *Periodicity and chaos from switched flow systems: contrasting examples of discretely controlled continuous flow systems*, IEEE Trans. Automat. Control **38**, 70 (1993).

Bibliography

- [89] I. Katzorke and A. Pikovsky: *Chaos and complexity in a simple model of production dynamics*, Discrete Dynamics in Nature and Society **5**, 179 (2000).
- [90] T. Schürmann and I. Hoffmann: *The entropy of strange billiards inside n -simplexes*, J. Phys. A **28**, 5033 (1995).
- [91] K. Peters and U. Parlitz: *Hybrid systems forming strange billiards*, Int. J. Bifur. Chaos **13**, 2575 (2003).
- [92] R. Carretero-Gonzalez, D. K. Arrowsmith, and F. Vivaldi: *One-dimensional dynamics for traveling fronts in coupled map lattices*, Phys. Rev. E **61**, 1329 (2000).
- [93] A. Torcini, A. Vulpiani, and A. Rocco: *Front propagation in chaotic and noisy reaction-diffusion systems: a discrete-time map approach*, Eur. Phys. J. B **25**, 333 (2002).
- [94] L. Kleinrock: *Queueing systems* (John Wiley & Sons, 1975).
- [95] O. Rudzick, A. Pikovsky, C. Scheffczyk, and J. Kurths: *Dynamics of chaos-order interface in coupled map lattices*, Physica D **103**, 330 (1997).
- [96] K. M. Brucks, M. Misiurewicz, and C. Tresser: *Monotonicity properties of the family of trapezoidal maps*, Commun. Math. Phys. **137**, 1 (1991).
- [97] L. Glass and W. Zeng: *Bifurcations in flat-topped maps and the control of cardiac chaos*, Int. Journ. Bif. Chaos **4**, 1061 (1994).
- [98] C. Wagner and R. Stoop: *Renormalization approach to optimal limiter control in 1-d chaotic systems*, J. Stat. Phys. **106**, 97 (2002).
- [99] P. Cvitanović, R. Artuso, R. Mainieri, G. Tanner, and G. Vattay: *Chaos: Classical and Quantum* (Niels Bohr Institute, Copenhagen, www.nbi.dk/ChaosBook/, 2003).
- [100] T.-Y. Li and J. A. Yorke: *Period three implies chaos*, Amer. Math. Monthly **82**, 985 (1975).
- [101] N. Metropolis, M. L. Stein, and P. R. Stein: *On finite limit sets for transformations of the unit interval*, J. Comb. Theo. **15**, 25 (1973).
- [102] A. N. Sarkovskii: *Co-existence of cycles of a continuous mapping of a line onto itself*, Ukr. Math. Z. **16**, 61 (1964).
- [103] R. Badii, E. Brun, M. Finardi, L. Flepp, R. Holzner, J. Parisi, C. Reyl, and J. Simonet: *Progress in the analysis of experimental chaos through periodic orbits*, Rev. Mod. Phys. **66**, 1389 (1994).

- [104] S. Göller: *Surreale Zahlen und reelle Dynamik*, Diplomarbeit, Universität Erlangen–Nürnberg (1998).
- [105] H. E. Nusse, E. Ott, and J. A. Yorke: *Border collision bifurcations: An explanation for observed bifurcation phenomena*, Phys. Rev. E **49**, 1073 (1994).
- [106] S. Banerjee and C. Grebogi: *Border collision bifurcations in two-dimensional piecewise smooth maps*, Phys. Rev. E **59**, 4052 (1999).
- [107] S. Banerjee, P. Ranjan, and C. Grebogi: *Bifurcations in two-dimensional piecewise smooth maps – theory and applications in switching circuits*, IEEE Transactions on Circuits & Systems – I **47**, 633 (2000).
- [108] Y. Shimada and K. Hirakawa: *Time constant for high field domain formation in multiple quantum well sequential resonant tunneling diodes*, Jpn. J. Appl. Phys. **36**, 1944 (1997).
- [109] K. J. Luo, H. T. Grahn, and K. H. Ploog: *Relocation time of the domain boundary in weakly coupled GaAs/AlAs superlattices*, Phys. Rev. B **57**, 6838 (1998).
- [110] M. Rogozia, S. W. Teitsworth, H. T. Grahn, and K. H. Ploog: *Relocation dynamics of domain boundaries in semiconductor superlattices*, Phys. Rev. B **65**, 205303 (2002).
- [111] A. Amann, A. Wacker, L. L. Bonilla, and E. Schöll: *Field domains in semiconductor superlattices: Dynamic scenarios of multistable switching*, in *Proc. 25th International Conference on the Physics of Semiconductors*, edited by N. Miura and T. Ando (Springer, Berlin, 2001), p. 801.
- [112] L. L. Bonilla, O. Sánchez, and J. Soler: *Nonlinear stochastic discrete drift-diffusion theory of charge fluctuations and domain relocation times in semiconductor superlattices*, Phys. Rev. B **65**, 195308 (2002).
- [113] J. Kastrup, H. T. Grahn, K. Ploog, F. Prengel, A. Wacker, and E. Schöll: *Multistability of the current-voltage characteristics in doped GaAs-AlAs superlattices*, Appl. Phys. Lett. **65**, 1808 (1994).
- [114] S. H. Kwok, H. T. Grahn, M. Ramsteiner, K. Ploog, F. Prengel, A. Wacker, E. Schöll, S. Murugkar, and R. Merlin: *Non-resonant carrier transport through high-field domains in semiconductor superlattices*, Phys. Rev. B **51**, 9943 (1995).
- [115] F. Prengel, A. Wacker, G. Schwarz, E. Schöll, J. Kastrup, and H. T. Grahn: *Dynamics of domain formation in semiconductor superlattices*, in *Proc. 9th Symposium on Ultrafast Phenomena in Semiconductors* (Lithuanian Journal of Physics **35**, Vilnius, 1995), pp. 404–407.

Bibliography

- [116] O. A. Tretiakov, T. Gramspacher, and K. A. Matveev: *Lifetime of metastable states in resonant tunneling structures*, Phys. Rev. B **67**, 073303 (2003).
- [117] E. Schomburg, K. Hofbeck, R. Scheuerer, M. Haeussler, K. F. Renk, A.-K. Jappsen, A. Amann, A. Wacker, E. Schöll, D. G. Pavel'ev, and Y. Koschurinov: *Control of the dipole domain propagation in a GaAs/AlAs superlattice with a high-frequency field*, Phys. Rev. B **65**, 155320 (2002).
- [118] P. T. Landsberg: *Recombination in Semiconductors* (Cambridge University Press, Cambridge, 1991).
- [119] V. Cheianov, P. Rodin, and E. Schöll: *Transverse coupling in bistable resonant-tunneling structures*, Phys. Rev. B **62**, 9966 (2000).
- [120] P. Rodin and E. Schöll: *Lateral current density fronts in asymmetric double-barrier resonant-tunneling structures*, J. Appl. Phys. **93**, 6347 (2003).
- [121] P. Rodin and E. Schöll: *Comment on lifetime of metastable states in resonant-tunneling structures*, Phys. Rev. B (2003).